# A Novel Optoelectronic Device Based on Correlated Two-Dimensional Fermions

A Thesis

Submitted to the Faculty

of

Drexel University

by

Pouya Dianat

in partial fulfillment of the

requirements for the degree

of

Doctor of Philosophy in Electrical and Computer Engineering

February 2015

## Dedications

To my parents, Nasser and Jaleh;

my sister, Tabassom;

and to Love and Life.

# Acknowledgments

Completion of this dissertation was a major test on my endurance, more than on my knowledge. It was not possible solely through performing academic research, but it required generous support and deep empathy from many people involved in my work. I truly appreciate everyone who provided guidance, support, and advice through the years of my graduate studies. In addition to the academic accomplishments, I have gained significant life skills, none of which were possible without the positive influence from my family, friends, and professors. I would like to also acknowledge all the people who made my life as a graduate student into a joyous one. The list is long but I cherish each contribution to my development as a scholar and a teacher.

First, and foremost, I am deeply thankful to my adviser, Dr. Bahram Nabet, whose never ending support and healing patience eased the rigorous task of acquiring my PhD. I appreciate his academic investment in me and many insightful conversations that we had regarding the dissertation. Moreover, he not only served as my academic adviser, but served as a mentor and a compassionate father during the years of my graduate studies that I was away from my family. Additionally, he framed my thought to function as an independent researcher, through his many tactful advice.

I want to acknowledge the infinite passion and faith that my mother, Jaleh, and father, Nasser, had in me. It was only through their encouragements that I could conquer mind barriers, and construct a secure foundation for my future life. Although being far away, the distinct perspective that they offered on my abilities assisted me on believing in my competency.

I have a profound appreciation for my sister, Tabassom, whose kind, close, and unconditioned love provided me the right mentality to maintain my life. She has definitely been a true aspiration for me to maintain a smile on my lips even when the life is offering nothing but trouble.

I have to mention the great role of my friends in supplying joy and content to my life, specifically Richard W. Prusak, who helped me in adopting to American life and made the lab a lively place, Ashkan Vakil for his sincere friendship, and Navid Abedini and Sonia Modares Razavi for their continuos support.

I want to thank my committee members for their encouraging words, thoughtful criticism, and time and attention during busy quarters.

# Table of Contents

# List of Tables

# List of Figures

# Abstract

A Novel Optoelectronic Device Based on Correlated Two-Dimensional Fermions

Pouya Dianat

Advisor: Bahram Nabet, Ph.D.

Conventional metallic contacts can be replicated by quantum two dimensional charge (of Fermion) systems (2DFS). Unlike metals, the particle concentration of these "unconventional" systems can be accurately controlled in an extensive range and by means of external electronic or optical stimuli. A 2DFS can, hence, transition from a high-density kinetic liquid into a dilute-but highly correlated-gas state, in which inter-particle Coulombic interactions are significant. Such interactions contribute negatively, by so-called exchange-correlation energies $E_{ex-corr}$, to the overall energetics of the system, and are manifested as a series negative quantum capacitance.

This dissertation investigates the capacitive performance of a class of unconventional devices based on a planar metal-semiconductor-metal structure with an embedded 2DFS. They constitute an opto-electronically controlled variable capacitor, with record breaking figures-of-merit in capacitance tuning ranges of up to 7000 and voltage sensitivities as large as 400. Internal field manipulations by localized depletion of a dense 2DFS account for the enlarged maximum and reduced minimum capacitances. The capacitance-voltage characteristics of these devices incur an anomalous "Batman" shape capacitance enhancement (CE) of up to 200% that may be triggered optically. The CE is attributed to the release and storage of $E_{ex-corr}$, from the "unconventional" plate and in the dielectric, respectively. This process is enforced by density manipulation of the 2DFS by a hybrid of an external field and light-generated carriers. Under moderate optical powers, the capacitance becomes 43 times greater than the dark value; thus a new capacitance-based photodetection method is offered.

This new capacitance-based photodetection method has a range of applications in optoelectronics, particularly in the next generation of photonic integrated systems.

# 1. Introduction

## 1.1  Background: Two-dimensional fermion systems

Physical systems that include aspects of reduced spatial dimensionality (RSD) have been the subject of extensive research. Mainly such systems exhibit physical properties, such as high-temperature superconductivity [1] and room-temperature quantum hall effect [2], that are different from three-dimensional systems. The condition of lower dimensionality occurs in materials with two-dimensional structural units, such as graphene [3, 4], MXene [5], and layered metal dichalcogenides [1, 6]. Achievement of a single layer graphene was demonstrated in 2004 by Novoselov and Geim [3]. Furthermore, any material system that can confine the movement of electrons in any (or all) of spatial dimensions satisfies the requirements for low dimensionality from an electrical (and optical) perspective on the system. The length extent of confinement has to be on the order of an electron de Broglie wavelength[1] in the respective medium. A well known instance of these systems is a metal-oxide-semiconductor transistors (MOSFET), in which formation of a 2D channel of electrons (or holes) at the oxide-semiconductor interface is essential for various application of this device. Other examples for this category of RSD systems are carbon nanotubes [7, 8], nano wires [7], quantum dot devices [9, 10], electrons on surface of liquid helium [11, 12], novel oxide interfaces [13, 14, 15], and high-electron mobility transistors (HEMTs) [16, 17]. The RSD devices cover a wide range of applications in electronics and photonics.

Two dimensional electron systems (2DES) have been the subject of discussion in the last 50 years, proceeding the invention of MOSFETs at Bell labs [18], as well as their observation on the surface of liquid helium [19, 20]. Many interesting physical

---

[1]For an electron with mass $m$, which is moving at a speed $v$, its de Broglie wavelength is defined as: $\lambda_{dB} = \frac{h}{mv}$, where $h$ is the Planck's constant.

phenomena such as integer and quantum Hall effect were initially observed in a 2DES [2, 21], since a 2D system provides a good medium for testing theories on physics of their operation. This is mainly because of weaker field potentials in 3D compared to lower dimensions, that impose a challenge for probing their influences. Substitution of metallic contacts with a counterfeit, comprised of two-dimensional charge system (2DCS), of either confined electrons (2DE) or holes (2DH), produces unconventional devices with altered electronic characteristics [192], which substantially depends on the properties of the confined charges. In unconventional parallel-plate capacitors, for instance, a quantum capacitance, in series with the geometric one, is identified as a consequence of finite density of states of the 2DE or 2DH systems [22, 23, 24]. Electrons and holes are charge carrying fermions, hence they are subject to the Pauli's exclusion principle (PEP). This is specifically important for many-fermion systems, as the PEP determines the statistics of the system, since it requires that no two particles with identical four quantum numbers may occupy the same state. Moreover, the negative thermodynamic density-of-states[2] of the 2DE or 2DH [25] causes anomalous capacitance enhancements (CE) [23, 24, 26] in the unconventional capacitors resulting in achieving capacitances that are much greater than the geometric capacitance, which has important potential application as a replacement for high-k dielectric materials[26] in MOSFETs. It can also allow substantial performance improvements of voltage-controlled capacitors, varactors[27]. A 2D charge system can be obtained at oxide interfaces [26] or at quantum wells (QWs) formed at semiconductor hetero-interfaces [27, 28, 29]. Distinctive to unconventional 2DES contacts, is the ability to control their carrier density from a high-density 2DES to a complete depletion [30, 31], through application of an external excitation, hence controlling their ground state energy. This feature is suitable for applications in capacitive-based photodetectors [32, 33],

---

[2]to be discussed in Chap. 3 of this dissertation

reduction of clock skewing in ICs [34] and actuation of varactors [27, 35, 36].

### 1.1.1  Realization of a 2D charge system

A two-dimensional charge system can be achieved by various band engineering techniques, and in a host of different materials, that can be categorized into three main classes:

**Hetero-interfaces:** A band gap difference at a junction between two different materials can be applied to localize charge carriers in a direction normal to the interface. When such an interface is formed between thin films of materials, the locality is only limited to one spatial dimension, while the charge carriers can freely move in the remaining two directions. Hence, a 2DCS can potentially be formed at a hetero-interface, contingent to further electrical considerations. Depending on the situation, under which a 2DCS is formed at the hetero-interface, the following customary categories appear:

- MOS devices: In metal-oxide-semiconductor (MOS) structures, a 2DCS is formed at the semiconducting side of the oxide-semiconductor interface. By applying a voltage to the metal, the minority charge carriers in the semiconductor accumulate at the oxide-semiconductor interface. If the applied voltage is large enough, the charge at the amount of the minority charge at the interface surpass the majority of the bulk and a 2D sheet of charge with a finite thickness is formed, which is essentially a quasi-2DCS. This 2D channel is the fundamental requisite for the functionality of MOS field effect transistors.

- Quantum Wells: An electron inside an infinite energy barrier well is a classic example in quantum mechanic courses, that can practically be realized in interfaces of typical III-V compound semiconductors. When a large band gap material such as $AlGaAs$ makes an interface with a lower band gap material,

such as $GaAs$, the Fermi level can be located above the conduction band at the interface. As a result, a quantum well is formed and the charge carriers become localized and confined in the direction normal to the interface. Specifically, proper spatial doping profile is required for this purpose. Through means of modulation doping [37], in which the impurities are located in the large band gap material, the confined carriers in the quantum well can be spatially separated from the dopants, which increases the carrier mobility inside the quantum well. This can then be utilized as the conductive channel in high electron mobility transistors (HEMTs) [16, 17, 37].

- Novel oxide interfaces: A recent class of hetero-interfaces in novel oxides is shown to serve as a host for a 2DCS [14, 38]. Among such novel oxides, the $LaAlO_3/SrTiO_3$ interface[13, 26] has received recent attention [38] for investigation of the properties of a 2DCS. The most exciting phenomena arising, or awaiting discovery, at customized oxide interfaces result from correlated electron effects. In correlated electron systems, the interaction of an electron with other electrons can no longer be described by the Coulomb interaction of a virtually free, independent particle with an average background charge that represents the other electrons.

**Material surfaces:** This category include materials, either in liquid or solid phase, that are insulating in the bulk and conductor only on the surface. The charge carriers can only move on the surface of the material and can not penetrate the three-dimensional bulk of the structure. Hence such a condition is considered a two-dimensional charge system. Two major examples of this kind of 2DCS are:

- Liquid helium: Due to the difference between the dielectric of the liquid medium and the surrounding medium, electrons that are outside helium "feel" an attractive image potential [39]. Simultaneously, the liquid helium imposes a potential

barrier of greater than 1eV [20] that prevents electrons from entering the liquid. This causes formation of a 2D electron gas on the surface of the liquid helium [11]. The energy separation of electrons in this 2DCS is in the microwave frequencies. Furthermore, the attainable electron density on the surface of the liquid helium is limited to values below $2 \times 10^9 cm^{-2}$ [12], which is much less than the semiconducting counterparts. Initial investigations of 2DCS was performed on this system, including the first observation of plasmons in a two-dimensional system [40]. Another important aspect on 2DCS on liquid helium is formation of a crystal formed of electrons, as a consequence of highly correlated electron system at low densities [41, 42].

- Topological insulators: This class of electronic materials have a bulk band gap like that of an insulator, however, the surface and/or the edges of the material includes conductive states that are protected by time-reversal symmetry [43, 44]. It was initially predicted that the spin-orbit interaction of electrons can lead to topological insulating electronic phases [45, 46]. Experimental, the existence of such insulators was verified in a $Bi_{1-x}Sb_x$ material system [47]. The surface (or edge) states of a topological insulator lead to a conducting state with properties unlike any other known 2D electronic systems. In addition to their fundamental interest, these states are predicted to have special properties that could be useful for applications ranging from spintronics to quantum computation.

**2D crystals:** Materials that have a two dimensional crystal structure can innately host a 2D charge system. Two-dimensional solids are defined as crystals with very high aspect ratios and thicknesses corresponding to a few atomic layers [48]. The charge carriers in these materials can hence move only in two directions and form a 2DCS. The most well known instance of these class of materials is graphene [49], which is comprised of atomically thin layers of $sp^2$-bonded carbon atoms connected

by aromatic in-plane bonds. The crystal has a honeycomb hexagonal structure with a carbon atom positioned at every corner. Graphene was first experimentally produced in 2003 and existence of a 2DCS in graphene was discovered by Novoselov et al [3, 50] in 2004. Graphene has remarkable electronic features that include a zero band gap, a linear energy band diagram [51], and a very large mobility at room temperature [52]. The density as well as the sign of the 2D charge carriers in graphene can be altered by applying a gate voltage. Graphene exists in the forms of a single- or bi-layer material, each of which demonstrate unique features. Specially, while it is practically transparent to visible light. When combined with its conductive properties, graphene becomes a desired material for photovoltaic applications. Other materials that possess similar two-dimensional structure include hexagonal boron nitrides [53], transition metal dichalcogenides [1, 6], and early transition metal carbides and/or carbonitrides labeled MXenes [5].

## 1.2 Properties of 2D fermion systems

When an ensemble of particles form a system, the principal laws of physics, mainly the conservation of energy and momentum, should be sufficient to predict the state of the system at any given time. This problem, however, becomes exponentially complicated as the particle number increases and is effectively impractical in realistic many particle system. In such system, the number of particles is in the order of Avogadro's number $(6.02 \times 10^{23})$, it is necessary to characterize the system by macroscopic measurable, and mainly overall energy, chemical potential, $\mu$, temperature, $T$, and particle density, $n$, for the system. These variable are related to the microscopic particle states through a stochastic analysis and by applying the law's of thermodynamics [54]. Importantly, such an approach is based on an equal *a priori probability* [55] assumption, which means that the system is equally likely to be found at any

of its accessible micro states. Hence the grand canonical ensemble [56] has to extensively include all the possible micro states. Such an approach will be discussed in Secs. 1.2.1.1 and 1.2.2.6, for *noninteracting* classical and quantum systems of fermions respectively. In such noninteracting systems, the (influence of) inter-particle interactions on the macro state of the device is ignored. Investigation of the properties of interacting systems is presented in Chap. 3.

A system of electrons, as charge carrying fermions, is innately an interacting system. In these systems the Coulombic forces among electrons can critically alter the macroscale landscape of the energy. Furthermore, any arrangement of a system of charge carriers, induces an electric field in the surrounding medium. For the case of a two dimensional electron (or hole) system, despite the dynamics in the charge plane, an effective charge density can be associated with the 2D sheet of charge. This greatly simplifies the calculations of the induced electric field on both sides of the 2D plane through laws of classical electrostatics, and will be discussed in Sec. 1.2.1.2.

Mathematical modeling of physical systems with reduced spatial dimensionality imposes less complexity, both numerically and theoretically, due to smaller matrix size and fewer tensorial components that describe the physics of a given system. Moreover, systems with reduced spatial dimensionality exhibit different behavior, compared to the 3D case and under similar external stimulus. The most well-known instance is the electrons confined in a 2-dimensional quantum well at which the energy and momentum become quantized across the direction of confinement. This quantization is essential for functionality of many infrared photodetectors [57] and quantum cascade lasers [58].

### 1.2.1 Classical analysis of a 2D plane of charge

In classical scheme, the state of an individual particle is completely defined with the position and momentum vectors, $\vec{r}$ and $\vec{p}$, respectively. Conservations of the energy and the momentum in a system of many particles adequately predict the state of the system at any given time. Importantly, in the classical picture, individual particles are *distinguishable*. It means that the particles, with identical physical properties inside a many body system, are distinctly labeled. Equivalently, an exchange in spatial position of any two particles inside the system results in a new overall state. In material systems the number of constituting particles (atoms, molecules, ions, etc.) are very large and it is impractical to determine the state of each and every particle by using the microscopic conservation laws. Hence, an approach is required that relates the macroscopic state of the system to the microscopic state of each particle. Boltzmann statistics provides the required method for treating the many-body systems in classical mechanics.

#### 1.2.1.1 Distinguishable fermions and Boltzmann Statistics

The distinguishability of fermions influences the statistics of the particles, and its thermodynamic state. In order to evaluate the macroscopic state of a system, it is essential to define the statistics of the microscopic particles. In a non-relativistic closed many particle system of electrons, the overall energy of the system, $E_{tot}$, and the total number of particles, $N$, remain constant as a consequence of the conservation of mass and energy laws. It is of interest to find the distribution of particles with respect to energy spectrum. For a classical set of *distinguishable noninteracting* particles, the possible ways for $N_i$ particles to occupy an energy state of $E_i$ with a degeneracy factor of $g_i$ is a combinational selection, $g_i^{N_i}.\binom{N}{N_i}$. Knowing that $\sum_i N_i = N$ and $\sum_i N_i E_i = E_{tot}$, the overall possible ways, $W$, of distributing the distinguishable

electrons in all the available energy levels of the system becomes:

$$W = N! \prod \frac{g_i^{N_i}}{N_i!}. \tag{1.1}$$

The entropy, $S$, of a system of particles is a measure of the number of specific ways in which the system may be arranged. It also describes the overall *disorder* of the system and is related to the number of all possible microstates, $W$, through Boltzmann's fundamental equation:

$$S = k \ln W, \tag{1.2}$$

where $k = 8.62 \times 10^{-5} eV/K$ is the Boltzmann's constant. Specifically, this definition of $S$ describes the system disorder by a physically comprehensible value as opposed to the extensive number of $W$. According to the second law of thermodynamics the entropy of an isolated system never decreases. Consequently, the number of microstates, as presented in Eq. 1.1, has to be maximized with respect to $N_i$. The problem is then reduced to finding Lagrange multipliers of $\alpha$ and $\beta$ in the following function:

$$f(N_i) = \ln W + \alpha(N - \sum N_i) + \beta(E - \sum N_i E_i), , \tag{1.3}$$

in which $N$ and $E_{tot}$ have to satisfy the following constraints:

$$N = \sum N_i, \tag{1.4}$$

$$E_{tot} = \sum N_i E_i. \tag{1.5}$$

Eq. 1.3 can be solved by setting:

$$\frac{\partial f}{\partial N_i} = \ln g_i - \ln N_i - (\alpha + \beta E_i) = 0. \tag{1.6}$$

Hence:

$$N_i = \frac{g_i}{e^{(\alpha+\beta E_i)}}. \tag{1.7}$$

By substituting Eq. 1.7 in Eq. 1.1, it can be shown that [56]:

$$dE = \frac{1}{\beta}dW - \frac{\alpha}{\beta}dN. \tag{1.8}$$

This has the same format as the second law of thermodynamics, stated as:

$$dE = TdS + \mu dN, \tag{1.9}$$

in which $T$, $\mu$, and $S$ are the temperature, the entropy, and the chemical potential of the system. The Lagrange multipliers and the distribution function are then found as:

$$\alpha = -\mu/k_B T, \ \beta = 1/k_B T \tag{1.10}$$

$$N_i = \frac{g_i}{e^{(E_i-\mu)/k_B T}}. \tag{1.11}$$

Eq. 1.11 is known as the Boltzmann distribution function and is valid for systems of many distinguishable particles. It relates the micro states of the classical system, $E_i$, to macroscopic variables of occupation number, $N_i$, and chemical potential, $\mu$.

### 1.2.1.2 Electric field distribution of a 2D charge system

An ensemble of electrons is comprised of charge carriers, each of which induces an electric field in the surrounding medium. The overall electric field, at any given point in the space, is calculated by classical physics through superposition of the electric field vectors of individual particles. In many-electron system that the number of electrons is very large, the particle density is a better representation than the total

number of particles. For an arbitrary distribution of charge, $\rho(r)$, in which $r$ represents the location in space, the electric field, $E(\vec{r})$, in the surrounding space with dielectric constant of $\epsilon$ is found classically through application of Gauss's law:

$$\nabla.E(\vec{r}) = \frac{\rho(\vec{r})}{\epsilon} \tag{1.12}$$

The electric field in the surrounding regions of an infinite two-dimensional sheet of charge that is located on $z = 0$ plane and has the areal charge density of $\sigma_0$, is then calculated by applying Eq. 1.12 to such a distribution. Consequently it is found that:

$$E(\vec{r}) = \frac{\sigma_0}{2\epsilon}.\hat{z}, \tag{1.13}$$

in which $E$ represents the electric field, $\vec{r}$ is a spatial position vector, and $\epsilon$ is the dielectric constant of the surrounding medium. Mainly, Eq. 1.13 indicates an electric field with constant magnitude and a direction normal to the plane of charge, either into the plane for a negative charge density, or out of the plane for a positive charge case. This has important implications if a 2-dimensional charge system (2DCS) is exerted inside a metal-semiconductor-metal (MSM) structure, as it will be discussed in Chaps. 2 and 4, since the electric field inside the device can then predictably be found and manipulated through density control of the 2DCS. Notably, a constant vertical electric field in conjunctions with a highly conductive medium of the 2DCS can reduce the travel path for photo generated EHPs in the MSM photodetector and enhance the speed of operation.

### 1.2.2 Quantum properties of 2D fermion systems

Quantum mechanics (QM) take a stochastic approach toward systems of particles. A probability distribution function (PDF) represents the likelihood of finding elec-

trons in a certain location and at any specific time. This PDF is known as the wave function,$\Psi$, of the system of one or more particles. Similar to statistics of random variables, an average value and a standard deviation (or uncertainty), as well as higher order moments, can be extracted from the wave function. Any other observable in the system can also be deduced from the wave function.

### 1.2.2.1 Observable operators

In the QM scheme, the observables of the system, such as position and momentum, are redefined as an operator, $\hat{O}$, that is acting on $\Psi$. The results of any measurement experiment for a specific operator are eigenvalues, $O$, that are the solutions of the following differential equation:

$$\hat{O}\Psi \; = \; O.\Psi. \tag{1.14}$$

The results of physically meaningful meausrements require to be real numbers hence, any operator in QM has to be Hermitian, that is:

$$\hat{O} \; = \; \hat{O}^*. \tag{1.15}$$

It follows that the uncertainty, $\sigma_O$, in the measurement of an arbitrary operator $\hat{O}$ becomes:

$$\sigma_O \; = \; \sqrt{\langle\hat{O}^2\rangle - \langle\hat{O}\rangle^2}, \tag{1.16}$$

where $\langle\rangle$ denotes *the expectation value* of a given variable/operator.

### 1.2.2.2 Schrödinger equation

The Schrödinger equation serves as the fundamental mathematical model to determine the wave function and its time evolution. It relates the energy operator, $\hat{H}$,

of the system of interest to the eigen states, described by the wave functions:

$$i\hbar\frac{\partial}{\partial t}\Psi(\vec{r},t) \;=\; \hat{H}\Psi(\vec{r},t). \tag{1.17}$$

The operator $\hat{H}$ is called the Hamiltonian of the system. Similar to classical system, the Hamiltonian is the total energy and accounts for both the kinetic and potential energy operators, $\hat{T}$ and $\hat{V}$, respectively:

$$\hat{H} \;=\; \hat{T}+\hat{V}, \tag{1.18}$$

$$\text{and } \hat{T} \;=\; \frac{\hat{p}^2}{2m}. \tag{1.19}$$

The wave function of Eq. 1.17 describes the likelihood of finding a particle at a given time and spatial position. It does not however, distinguish between "different" particles and does not indicate "which" particle is located at the certain point in space. In other words, in the quantum picture all the particles are identical and indistinguishable.

### 1.2.2.3   Operator commutator and uncertainty principle

The commutator of the operators $\hat{A}$ and $\hat{B}$, with eigenvalues $a$ and $b$, respectively, is defined by:

$$[\hat{A},\hat{B}] \;=\; \hat{A}.\hat{B}-\hat{B}.\hat{A}. \tag{1.20}$$

The two operators $\hat{A}$ and $\hat{B}$ are said to commute if $[\hat{A},\hat{B}]=0$. It can be shown that any two commuting operator share the same basis of eigenstates, and they can be measured simultaneously and accurately [59]. Conversely, if two operators do not commute, only one of the respective observables can be accurately measured at a time.

Specifically, the commutator for position, $\hat{r}$, and momentum, $\hat{p}$, operators becomes:

$$[\hat{r}, \hat{p}] = i\hbar. \tag{1.21}$$

By using Eqs. 1.21 and 1.16 a fundamental concept in QM can be reached, which is known as Heisenberg uncertainty principle:

$$\sigma_x \sigma_p \geq \frac{\hbar}{2}, \tag{1.22}$$

in which $\sigma_x$ and and $\sigma_p$ represent the uncertainty associated to $\hat{r}$ and $\hat{p}$, respectively. The principle of Eq. 1.22 indicates that a minimum uncertainty exists in the measurement of the observables that do not commute. Equivalently, the higher accuracy in the measurement of one of them, results into a greater uncertainty in simultaneous measurement of the other. The QM system converges into the classical limit when $\lim \hbar \to 0$.

### 1.2.2.4    Permutation operator

A Permutation operator, $\hat{P}_{i,j}$ with eigenvalues $p_{ij}$ is defined as an operator that *exchanges* two particles $i$ and $j$ in a many-particle system with a wave function $\Psi(...i...j...)$. That is:

$$\hat{P}_{i,j}\Psi(...i...j...) = \Psi(...j...i...). \tag{1.23}$$

If the particles are indistinguishable, it requires the system to remain invariant under exchange of particles, hence:

$$\Psi(...j...i...) = \pm\Psi(...i...j...). \tag{1.24}$$

Combining Eqs. 1.24 and 1.23 indicates that the eigenvalues $p_{ij} = \pm 1$. Hence, the Hamiltonian and Permutation operators commute:

$$[\hat{H}, \hat{P}] = 0. \tag{1.25}$$

The result of Eq. 1.25 is important since it shows that $\hat{H}$ and $\hat{P}$ share the same basis of eigenstates. For the states with $p_{ij} = +1$, the wave function is symmetric and the particles that occupy such states are called bosons. Conversely, those particles that occupy the antisymmetric states with eigenvalues $p_{ij} = -1$ are called fermions. This particle categorization is specifically necessary since an ensemble of bosons and fermions will follow different statistics, as will be shown in Sec. 1.2.2.6, and hence exhibit distinct macroscopic behavior. Since electrons (and holes) are charge carrying fermions, the investigation of fermion properties and their collective behavior are the main subjects of discussion for this dissertation.

### 1.2.2.5 Pauli's exclusion principle for fermions

A restatement of Eq. 1.24 for fermions shows such a system possess an antisymmetric wave function, $\Psi_F$, that is:

$$\Psi_F(...j...i...) = -\Psi_F(...i...j...). \tag{1.26}$$

A special case for Eq. 1.26 occurs when two fermions occupy the same state, or when $i = j$. In this case:

$$\Psi_F(...j...i...)|_{i=j} = -\Psi_F(...i...j...)|_{i=j}, \tag{1.27}$$

and as a result,

$$\Psi_F(...i...i...) = 0. \tag{1.28}$$

Eq. 1.28 is the mathematical expression of the Pauli's exclusion principle. It shows that the likelihood of having two fermions occupying the same energy state is zero. Hence, no more than one fermion can occupy a state in a many-fermion system. It can be inferred from this requirement that a repelling "force" exists among fermions that prevents co-existence of two particles at the same state. This is known as the *exchange* force. A corresponding *exchange energy* can be associated with this force. It is to be noted that the exchange Force between fermions has a completely quantum mechanical nature and should not be confused with the repelling electrostatic forces, such as that among electrons.

### 1.2.2.6   Indistinguishable fermions and Fermi-Dirac Statistics

The statistical analysis of Sec. 1.2.1.1 has to be modified to account for the *indistinguishability* of fermions in a *noninteracting* system. Following Pauli's exclusion principle, no more than one fermion can occupy a certain energy state. Hence, the number of ways to distribute $N_i$ fermions in an energy level $E_i$ with the degeneracy factor of $g_i$ becomes a combinational selection: $w(g_i, N_i) = \binom{g_i}{N_i}$. The overall number of ways, $W$, for distribution of $N$ fermions in the available energy states is:

$$W = \prod_i w(g_i, N_i) = \prod_i \frac{g_i!}{N_i!(g_i - N_i)!}. \tag{1.29}$$

Equ. 1.29 is distinct from Eq. 1.1, mainly because the former does account for the indistinguishability of fermions. The rest of the analysis remains the same as that of Sec. 1.2.1.1. Consequently the statistics for a set of noninteracting indistinguishable fermions becomes:

$$N_i = \frac{g_i}{1 + e^{(E_i - \mu)/k_B T}}. \tag{1.30}$$

This equation is known as the Fermi-Dirac statistics.

### 1.2.2.7 An interacting fermion system

Both Boltzmann and Fermi-Dirac statistics are based on an equal a-priori probability assumption that is only valid when the particles are not mutually interacting. For charged particles such as electrons, there exists a long range significant Coulombic interaction. Consequently, in such a correlated system, the above assumption and the consequential statistics are not valid. It is required to incorporate the influence of the correlational Coulombic forces in the Hamiltonian of the many electron system. This step, however, imposes practical limitations due to the long range nature of Coulombic interaction and the potential associated with it. A number of techniques are typically applied to reduce such a system to an analytically approachable one. Those include a mean field approximation in Hartree-Fock method [60], application of a "jellium" model in random phase approximation (RPA) [61, 62], and application of Green function and Feynman diagrams in evaluation of (Lindhard) linear response of electrons [63].

### 1.2.3 Ground state energy of a many-fermion system

The ground state energy (GSE) of a 2DFS essentially includes terms that are related to the kinetic energy of individual electrons, and the inter-particle interactions among fermions in the system. A meaningful calculation of GSE has to account for quantum mechanical exchange and correlation forces among fermions, in addition to the classical kinetic energies of distinguishable particle. Fig. 1.1 compares the GSE of a distinguishable system of fermions with that of an indistinguishable one. The details of the contributing terms to GSE is the subject of Chap. 3 of this dissertation.

**Ground State Energy of many-fermion systems**
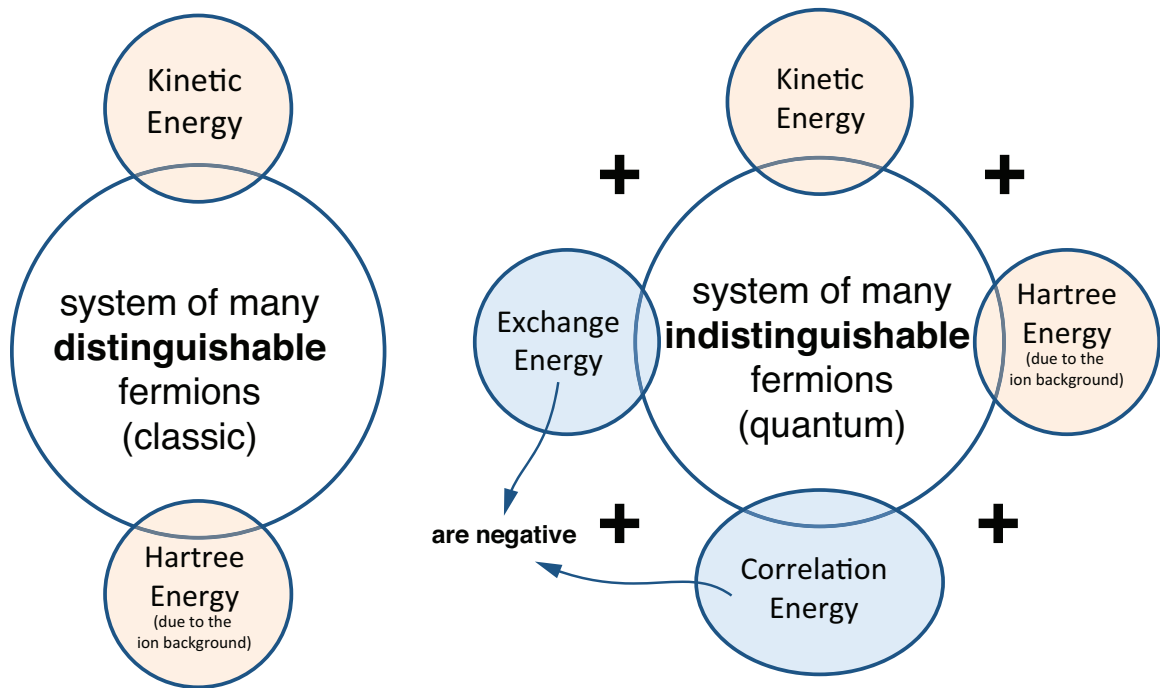


Figure 1.1: Contribution of various energy terms to the total ground state energy of many-body systems of distinguishable and indistinguishable fermions.

## 1.3 Density manipulation in 2DFS

Unlike metals, the particle density of a 2DFS that is attained in non-metallic crystals can be varied by changing the boundary and/or initial conditions of the system. Applying an external field effect is a common method of density manipulation in semiconductor devices, as in MOSFETs. Furthermore, depositing additional charge carries–typically generated through photon absorption–is an alternative for density manipulations in many-electron systems. Both of these methods can change the global particle density. Local variations in fermion density is also possible, while keeping the overall value constant. This can launch charge density waves [64] and plasmons [65], in the fermion system that may transfer energy between desired spatial locations. Fig. 1.2 summarizes these common methods for density manipulation. It is relevant
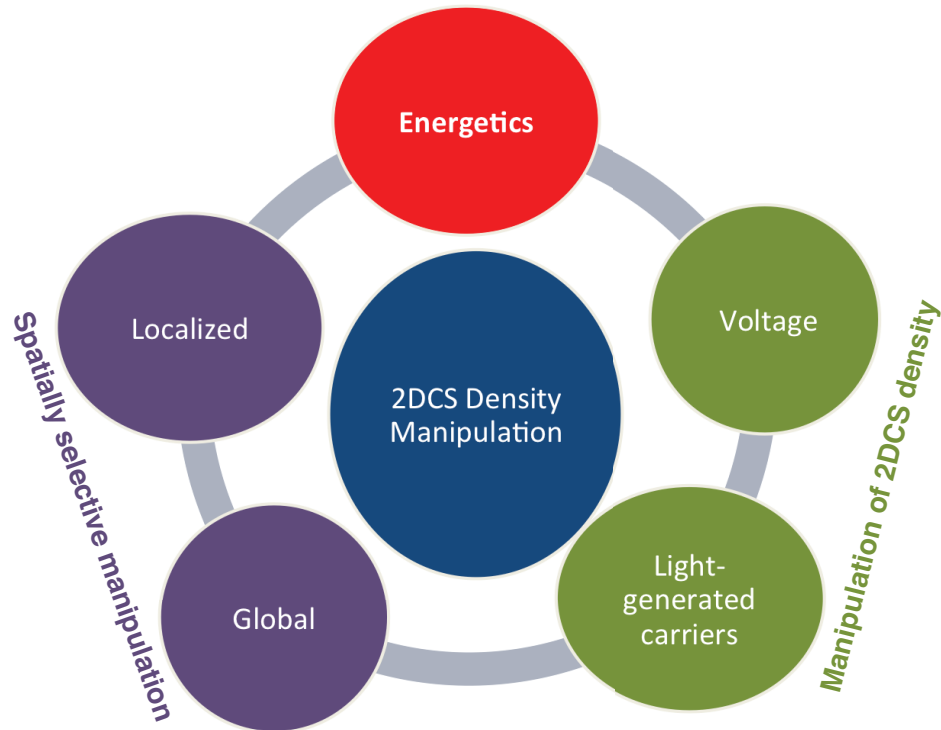
Figure 1.2: Significant aspects of a many-body system of fermions.

for this dissertation to examine these methods for a 2DFS that is attained in a QW at a $GaAs/AlGaAs$ hetero-interface.

### 1.3.1 Application of an external voltage

The density of 2DCS in semiconductor devices can be controlled either statically, through material structural considerations, such as a doping profile, or dynamically by exertion of external forces such as a bias voltage. In MOSFETs the concentration of the 2DCS at the oxide-semiconductor interface can be accurately controlled by gate voltage. Different regions of operation for the MOSFETs are identified based on the amount and sign of the 2D interfacial charge. The operation of a MOSFET is

thoroughly investigated in the last decades and can be found elsewhere [39, 66].

Modulation-doped field effect transistors (MODFETs) are a subcategory of FETs, in which a 2DCS is statically introduced at a hetero-interface, through sophisticated doping methods [30]. In MODFETs, the 2DCS conducting channel is spatially separated from the dopants. This significantly reduces the amount of impurity scattering [16, 17] and hence the carrier mobility increases. Consequently MODFETs are also known as high electron mobility transistors, or HEMTs. A quantum well can be formed at the interface of a semiconducting material, such as GaAs, with a large band gap insulating layer, such as AlGaAs. The modulation doping profile is located in the insulating layer, that raises the equilibrium Fermi level to above the conduction band inside the semiconductor and at the interface. A thin triangular quantum well at the hetero-junction is then populated by electrons, that forms the conducting channel. A gate contact is typically fabricated on top of the insulating layer, and by applying a voltage to this contact, the density of the 2DCS can be controlled. The charge concentration of this 2DCS layer at equilibrium is found by [31]:

$$n_{s0} = (DOS)\frac{k_B T}{q}\ln\left[\left(1 + exp\left\{\frac{q}{k_B T}[V^+ - E_0]\right\}\right)\left(1 + exp\left\{\frac{q}{k_B T}[V^+ - E_1]\right\}\right)\right],$$
$$(1.31)$$

in which $DOS$ is the density of state for a 2D system, $q$ and $k_B$ represent electron charge and Boltzmann constant, respectively, and $V^+$ is the potential at the semiconducting side of the heterointerface. Additionally, in Eq. 1.31, we have:

$$E_0 = \gamma_0 n_{s0}^{2/3} \qquad (1.32)$$

$$E_1 = \gamma_1 n_{s0}^{2/3} \qquad (1.33)$$

Here $\gamma_0 \approx 2.5 \times 10^{-12} eV cm^{4/3}$ and $\gamma_1 \approx 3.2 \times 10^{-12} eV cm^{4/3}$ for GaAs. It can be seen from Eq. 1.31 that the density $n_{s0}$ depends on interface potential at the

semiconducting side, $V^+$. At equilibrium $V^+$ and Fermi level coincide, however, by changing the gate voltage this potential, and hence $n_{s0}$ can be varied.

### 1.3.2 Density modification through photon-generated charge carriers

Unlike metals, in semiconductor materials, light can be absorbed and an electron-hole pair (EHP) is generated as a result. Any photo sensitive device operates based on physical separation of the light-generated carriers by a local electric field. Collection of the EHP by an external circuit is the basis of operation for many photodetectors.

It is possible to separate and deposit the optically generated EHPs in a 2D reservoir of charge, hence manipulating the charge density of a 2DCS. Consequently, any physical property of the 2D system that is a function of its density can be manipulated by the additional EHPs. This method constitutes many optoelectronic and photonic applications for devices that include a 2DCS.

### 1.3.3 Collective properties of a 2DCS

The manipulation methods of Secs. 1.3.1 and 1.3.2 change the overall density of the 2DCS from its equilibrium value, through subtraction, addition or deposition of carriers. These alterations can be done both locally or globally. Another class of 2DCS manipulation, however, is achieved by locally "tweaking" the 2DCS density, while keeping the overall density of the 2D plane constant. As a result, an imbalance in the local electric field among the carriers and the background is induced and transferred to other regions of the 2DCS. Equivalently, a charge density wave (or a plasmon) can be launched in the 2DCS by a local excitation of density [65, 67, 68]. The properties of such waves are the subject of the plasmonic field [65, 68], has been recently extended to novel materials such as in graphene [69]. Energy relaxation through propagation of plasmon has significant applications in various fields, such as

nano photonics [68] and specifically in Terahertz electromagnetic wave detection and generation [70].

## 1.4    Utilization of 2D fermion systems in semiconductor devices

Many modern electronic devices utilize the 2D fermion system. Primarily in MOS-FETs the inversion and accumulation layers are dynamic 2D charge systems. Furthermore, various photonic and optoelectronic devices function based on properties of 2D charge systems. Here a few important applications of a 2DFS in semiconductor devices is presented.

Voltage controlled capacitors, or varactors, have many applications in microwave circuits, namely in RF filters [71, 72, 73], voltage-controlled oscillators [74] and frequency multipliers [75]. Primary figures-of-merit for performance of varactors are tuning ratio (TR) and quality factor, Q. The $TR = \frac{C_{max}}{C_{min}}$, indicates the range that the capacitance can be varied, where $C_{max}$ and $C_{min}$ are the maximum and minimum capacitances, respectively, in the capacitance-voltage characteristics (C-V) of a varactor. The quality factor, Q, is a measure of the stored to dissipated energy; with a trade-off generally expected between TR and Q [76]. Additionally, a voltage sensitivity (S) is quantitatively defined by $S = \frac{dC}{dV} \times \frac{V}{C}$, and indicates the normalized rate of change in the capacitance with respect to the applied voltage [77, 78], showing how abrupt in voltage the capacitance can vary within the tuning range. Importantly, sensitivity S demonstrates the level of nonlinearity in C-V, required for frequency multiplication applications.

Since varactors are typically made of vertical parallel plates, their minimum conceivable capacitance will be bound by a rather large geometric plate capacitor. This limitation can be changed by substituting the varactor architecture with that of a planar metal-semiconductor-metal (MSM) structures. These devices consist of two

coplanar Schottky metal plates and hence have a small geometric capacitance. They are mainly used as low-noise high-speed photodetectors [79, 80] where photo generated carriers are rapidly collected by the electric field between the contacts. The Schottky contacts also produce the requisite small capacitance for high-speed photo-detection. If applied as a varactor, however, typical MSMs do not incur a large maximum capacitance. Furthermore, the capacitance does not vary significantly with applied bias voltage[3], hence the TR for a conventional MSM becomes insignificant. Conversely, unconventional MSMs have been proposed that incorporate 2D systems of electrons or holes for varactor applications with the added advantage of sensitivity to light [29, 77, 78, 81]. While MSM-based varactors may display TRs of over 100, those incorporating 2D charge, have reported values as large as 1000 [27, 29], which is the largest among the TRs for various varactor technologies [76], including those based on MOSFETs [82], MEMS [83] and hetero-structures [29, 75, 84, 85, 86]. Moreover, MSM varactors benefit from an existing fabrication process that is compatible with HEMT technology, based on either GaAs or InP substrates, and is hence ideal for monolithic microwave integrated circuits[29, 85]. These MSM varactors have a large no-bias parallel-plate capacitor comprised of the cathode as one plate and the underlying 2DES as the other. The gradual depletion of the confined charges by an applied bias voltages, $V_{bias}$ reduces the capacitance to the small geometric value of a planar MSM. Consequently very large TRs are achieved. Moreover the current-blocking Schottky contacts ensure large quality factor. Moderation of internal quantum mechanical energies, such as exchange energy of an unconventional contact, comprised of a system of two-dimensional charge carriers, improves performance merits of variable capacitors, varactors, mainly in the TR and sensitivity, S. Energy transfer from the unconventional contact to the dielectric increases energy density and enhances the

---

[3]i.e. see Fig. 1.3

capacitance of the varactor.

### 1.4.1 Correlated 2D fermion systems for design of new semiconductor device

There exists a vast theoretical work on the properties of a many fermion system that are related to the inter-particle correlations with many comprehensive reviews articles on this subject [87, 88]. The practical applications of such systems that are associated with the many-particle features are still scarce. The exchange and correlation energies of a 2DFS can be stored in a dielectric of a plane capacitor [89]. Consequently, the energy density of the capacitor dielectric can be increased and the overall capacitance is enhanced. This is an important feature that is proposed to serve an alternative to application of high-$\kappa$ dielectric materials for gate capacitance ehncements in FETs [26].

This dissertation reports on design, fabrication and analysis of an unconventional MSM varactor with an embedded 2D electron system fabricated in a HEMT compatible GaAs/AlGaAs system. The tuning range of these devices exceeds well over 5000, which surpasses previous reports while maintaining a Q of greater than 30 that is comparable to typical HEMT-based varactors [76]. Classical analysis of the device capacitance indicates that the electric field alterations by the underlying high-density 2DES accounts for device performance. By localizing density manipulation of the 2DES to the region underneath the reverse biased contact, the no-bias capacitance ($C_{0V}$), is twice the previously reported values [81]. Furthermore, total depletion of the 2DES underneath the cathode at large $V_{bias}$, while preserved elsewhere, reduces $C_{min}$ to a stray capacitance between cathode and the preserved 2DES, which falls below the geometrical capacitance of a conventional MSM that lacks 2DES. Finally, this MSM-2D varactor has voltage sensitivity as large as 370, a critical quality for

usage as a switched-capacitor, but without the requirement for additional switching elements. The MSM-2D varactor combines the unconventional features of 2DES with superior electrical properties of MSMs.

Importantly capacitance of capacitors in which one or both plates are made of a two-dimensional charge system (2DCS) can be increased beyond their geometric structural value. This anomalous capacitance enhancement (CE) is a consequence of manipulation of quantum mechanical exchange and correlation energies inside the ground state energy of the 2DCS. Macroscopically, it occurs at critical charge densities corresponding to transition from an interacting "metallic" to a non-interacting "insulator" mode in the 2D system. In this dissertation this concept is applied to a metal-semiconductor-metal capacitor with an embedded two-dimensional hole system (2DHS) underneath the plates for realization of a capacitance-based photodetector [33]. Under sufficient illumination, and at critical voltages the device shows a giant CE of 200% and a peak-to-valley ratio of over 4 at probe frequencies larger than 10kHz. Remarkably, the light-to-dark capacitance ratio due to CE at this critical voltage is well over 40. Transition of the 2DHS from insulator to metallic, enforced by charge density manipulation due to light-generated carriers, accounts for this behavior, which may be used in optical sensing, photo capacitors, and photo transistors.

## 1.5   Review of metal-semiconductor-metal devices

Metal-semiconductor-metal (MSM) devices are comprised of two coplanar metallic contacts on a semiconducting substrate. Since a metal-semiconductor junction (MS) can either be an Ohmic or a Schottky contact, three different devices are expected for a device with two MS contacts:

- If both MS contacts are Ohmic, the resulting device is mainly modeled through the properties associated with semiconductor portion of the device. In such a

device, each MS contact is modeled by its associated contact resistance. A very simple example of this category is a photoconductor, in which deposition of light generated carriers inside the semiconductor significantly changes the overall resistance of device. A more complicated device can be a MOSFET, in which two Ohmic MS contacts, for the source and the drain terminals, are connected through a channel. The conductivity of this channel is then controlled through a third gate terminal. MOSFETs are specifically interesting for the purpose of this dissertation, as they include a 2DCS as the channel, and provide a source of comparison for the unconventional metal-semiconductor-metal structure that will be discussed in the later sections of this chapter. Due to extensive research on MOSFETs, the properties of a device with two ohmic contacts and a 2DCS is very well known and documented [39].

- A device with one Schottky and one Ohmic MS contact with a semiconductor in between comprises a Schottky diode that has been very well studied and characterized since 1940s upon the modeling proposed for metal-semiconductor junction by Mott and Schottky [66, 90, 91, 92].

- The third category includes semiconductor devices with two Schottky MS contacts as their terminals. The simplest format of this device is two co-planar MS contacts on an undoped semiconductor. This metal-semiconductor-metal (MSM) device can be assumed as two back-to-back Schottky diodes. This assumptions deems to be insufficient for explanation of device performance when applied as a photodetector. MSMs are widely used for photodetector properties due to their fast response time, and superb noise performance [36, 80, 93, 94]. Since the device architecture of MSMs comprises the basis structure for the devices that are discussed in this dissertation, a brief review of these devices is presented in the remainder of this section.

### 1.5.1 A conventional metal-semiconductor-metal structures with Schottky contacts

Metal-semiconductor-metal (MSM) structures are a set of optoelectronic devices, with major applications in photon detection [95, 96]. These devices are composed of two Schottky metal-semiconductor contacts that share the semiconducting structure as the absorption medium. In these photonic devices electron-hole pairs (EHP) are generated by absorption of incident photons, transported, and collected at the contacts by the electric field in the absorption medium. Consequently, a successful event of detection requires generation of an EHP by an incident photon, and separation and collection of EHP at the respective contacts before occurrence of recombination of EHP. Figures of merit for performance of photodetectors are light sensitivity and speed of response. Hence a large quantum efficiency, and a low noise/dark current are pursued in design of a highly sensitive MSM detector. Furthermore a fast carrier transport mechanism and short carrier life times are essential in a fast photodetector.

Employment of Schottky metal-semiconductor junctions as the contacts provides a very low dark current in the MSMs, and a superior noise performance over other technologies such as $p - i - n$ and avalanche photodetectors. The latter technologies typically require highly doped $p-$ and $n-$doped regions on which deposition of a quality Schottky contact is difficult. Furthermore, the planar structure, use of undoped layers, low dark currents and minimal capacitance of MSM make them an ideal candidate for microwave photonics integrated circuits [97].

Speed of operation and the dynamic behavior for the MSMs, are generally determined by the two following categories:

- RC time constant of the metal-semiconductor-metal structure [98]. MSMs benefit from very low dark capacitance, and this is the main advantage of MSMs. For instance, in the case of an MSM and p-i-n photodetector with comparable

sizes, the former can have capacitance values of up to three times less than the latter [97]. This is mainly due to the planar structure of the MSM, which minimizes the geometric capacitance between the contacts. Conformal mapping techniques are applied to calculate the capacitance per unit area, $C_{geo}$ for two coplanar contacts with spacing $S$ and width $D$ on top of a semi-infinite semiconductor with relative permittivity $\epsilon_r$ as [99]:

$$C_{geo} = \epsilon_0.(1 + \epsilon_r).\frac{K(k)}{K(k')}, \qquad (1.34)$$

with

$$K(k) = \int_0^{\frac{\pi}{2}} \frac{d\phi}{\sqrt{1 - k^2 sin^2\phi}}, \qquad (1.35)$$

$$k = tan^2\left[\frac{\pi}{4}.\frac{D}{S+D}\right], \; k' = \sqrt{1 - k^2}. \qquad (1.36)$$

Fig. 1.3 shows the capacitance-voltage (C-V) characteristics for a set of MSM devices, that were fabricated on a GaAs substrate. An HP4284A LCRmeter was used for obtaining the C-V. The measurements were performed at 1 and $10kHz$ of probe frequency, with a $30mV$ oscillating voltage, and at room temperature. The contact pads are coplanar square shape $Au/Ti$ metals with "small" $100 \times 100\mu m^2$ and "large" $150 \times 150\mu m^2$ sizes, and various spacings of 5 and $20\mu m$. With this rather large contact area, the measured capacitance remains in tens of femtoFarad, while for a $p - i - n$ photodiode with similar carrier transit times as of this MSM, the capacitance is reported to be in sub-picoFarad range [97]. The capacitance value drops up to one order of magnitude, when the probe frequency is increased from 1 to $10kHz$. This decline in capacitance is attributed to the slow interface states at the Schottky-semiconductor junction

[100]. This happens because at lower frequencies the interface states can follow the oscillating voltage and yield an excess capacitance. In the high frequency limit, however, the interface states cannot follow the signal. This makes the contribution of interface state capacitance to the total capacitance negligibly small.
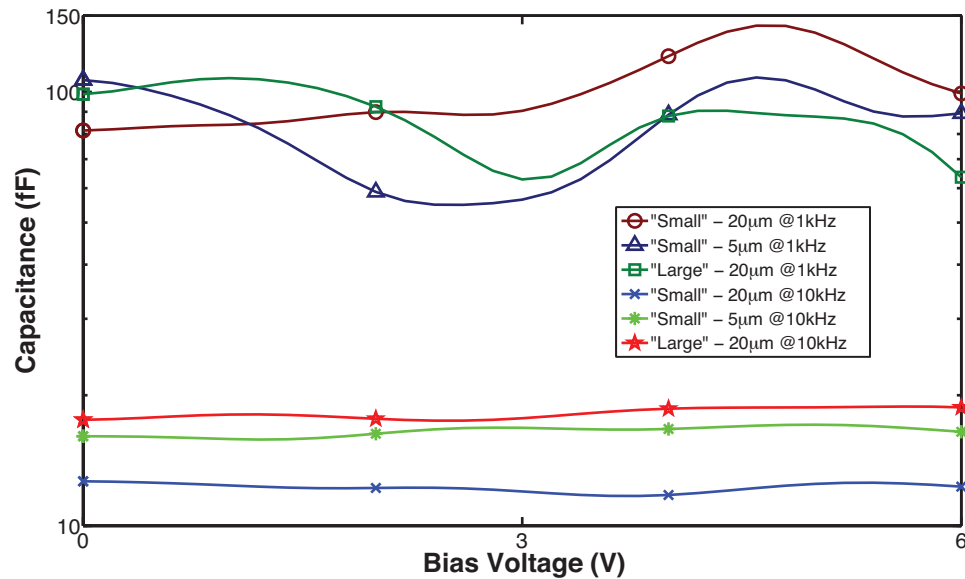


Figure 1.3: Capacitance-Voltage characteristics for a conventional MSM with GaAs as the absorption region.

- Carrier transit time inside the MSM structure [101]. It is desired to minimize the light generated carrier transit time without sacrificing the sensitivity and the quantum efficiency, or entering the MSM device into the breakdown region due to applications of high fields. Among the materials of choice as the absorption medium, $GaAs$ has the largest mobilities and hence has commonly appeared in MSM photodetectors. Even in this case, however, the transit time will be limited by velocity saturation of electrons at high fields, as well as by much

heavier, hence slower holes. In general, the transit-time limited cut-off frequency is highest for a contact spacing $S$ and the absorption region of thickness $W_a$, when [102]:

$$\frac{S}{W_a} \approx 0.5 \tag{1.37}$$

More advanced approaches for improving the dynamics of MSM photodetectors is by using materials, such as low-temperature grown $GaAs$ [103], with short carrier life time [94]. Such MSM photodetectors are demonstrated for detection in terahertz frequencies [94, 104].

A comprehensive review on on MSM structure can be found elsewhere (e.g. Zhao [105]; Seddik [106]).

### 1.5.2 Hetero-junction MSM devices

In order to decrease the dark current and noise in the MSM photodetectors, a barrier enhancer layer can be stacked on top of the absorption region. This layer has to have a larger band gap, compared to the underlying absorption region. Consequently, thermally generated electrons (hole) require to overcome an energy barrier at the interface, which is equal to conduction (valance) band offset of the two materials, in order to reach the metal contacts to contribute to the dark current. This increased barrier, eventually, reduces the amount of dark current. Adding a top layer with a larger band gap, compared to the absorption region, constitutes a heterostructure metal-semiconductor-metal (HMSM) photodetector.

The layer structure of an HMSM is similar to that of high electron mobility transistors (HEMTs), hence its fabrication does not impose any major challenge as it follows the well-established growth technology of HEMTs. Consequently HMSMs are notable candidates for microwave photonic integrated circuit applications.

### 1.5.3    Distribution of electric field lines inside a conventional HMSM

As described in previous chapters, HMSMs function based on E-field assisted collection of photon generated EHPs inside the absorption region of the device. Consequently the distribution of the electric field lines inside the photodetector has a significant effect on the performance merits of such devices. Fig. 1.4 visualizes the electric field distribution inside an HMSM with $2\mu m$ of contact spacing. This result was calculated through numerical solutions to Poisson and drift-diffusion equations by Synopsys Sentaurus$^{TM}$ device simulation package. This HMSM is composed of a top $AlGaAs$ barrier layer with a thickness of $50nm$. It is then followed by a $100nm$ GaAs absorption region which is grown on top of a $500nm$ GaAs buffer layer. All these layers are on top of a GaAs substrate. The electric field lines has a dominant
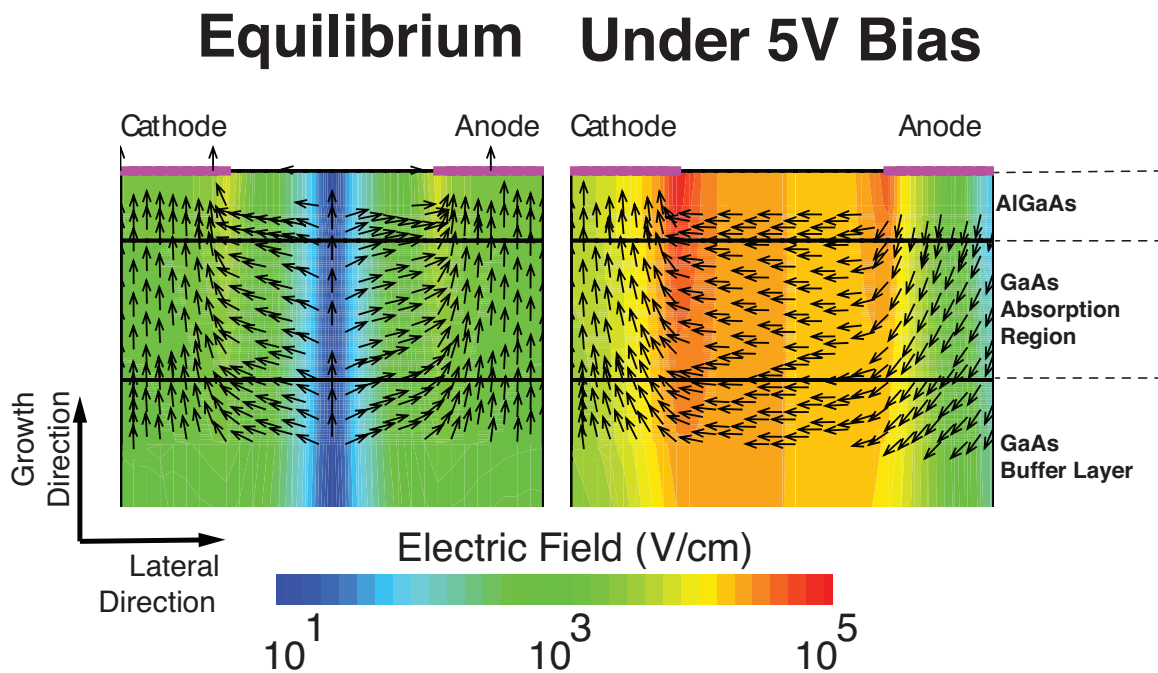


Figure 1.4: Calculated electric field line distribution inside a conventional HMSM device at equilibrium (left) and under 5V of bias voltage (right).

horizontal component in the bulk of the device. For EHPs that are generated in the GaAs absorption region, the election and hole get separated by the electric field and travel the distance from the point of generation to the collection at the contacts in alignment with the electric field lines. Since the speed of operation for an MSM is determined by the travel time of the light generated carriers, it is essential to minimize the travel path. This can be done by reducing the physical separation of contacts, which also reduces the device sensitivity. Any solution that can maintain the device sensitivity, while enhancing the response speed, becomes desirable. One approach to this is to alter the electric field landscape of the MSM through introduction of a 2DFS.

### 1.5.4 An HMSM with an embedded 2DFS

The electric field in the surrounding medium of a plane of charge can be found by applying Gauss's law, also derived in Sec. 1.2.1.2. In this case, the electric field lines will be normal to the 2D plane. With embedment of a 2DFS in the layer structure of an HMSM, the landscape of E-field lines can be varied. If this new MSM-2DFS device is utilized as a photodetector, it is expected that the light generated EHPs travel a shorter distance to be collected at the contacts. Light generated carriers will be moving vertically toward the contacts, and the large horizontal travel path is then avoided. At the same time, since the physical dimensions of the device is not changed, the sensitivity factor of the MSM-2DFS photodetector is not compromised. A practical HMSM device with an embedded two-dimensional hole gas, in which the vertical field in the MSM structure is created by a 2-D gas that transforms a conventional lateral MSM device to a vertical one, and although remaining as a planar structure, it allows a device design for high-speed performance without sacrificing the external quantum efficiency [36, 77].

Poisson and drif-difussion equations were solved numerically by Synopsys Sentaurus$^{TM}$ device simulation package to obtain the conduction band energy (CBD) of HMSMs with and without a 2DES. Fig. 1.5 compares the (CBD) for an HMSM without (left) and with (right) an embedded 2DFS under $5V$ of bias voltage. The former has the same layer structure as that of Fig. 1.4 (see Sec. 1.5.3), while the latter incurs a 2DES layer at the $GaAs/AlGaAs$ interface. The CBD has a gradual decline between the contact pads for the former case. It indicates the extent of horizontal travel path for EHPs before collection at the contacts. In contrast, for a device with a 2DFS, the CBD has an evident vertically-oriented drop across the absorption medium with an abrupt drop in potential at the edge of the contact. No significant horizontal variation in CBD is seen in the region between the contacts. Consequently, the light generated EHPs may travel a much shorter vertical distance to arrive at the collecting terminals. The idea here is to facilitate the horizontal transit of the EHPs through a high mobility medium of the 2DFS. It is shown that the 2DFS layer can enhance the dynamic response of an MSM photodetector by using an alternative energy relaxation mechanism, in place of the conventional light-generated charge transport [107].

## 1.6 Scope and organization of this dissertation

### 1.6.1 Statement of the problem

The main subject of study in this dissertation is the influences of an embedded 2D charge system (2DCS), as a counterfeit metal, on performance of metal-semiconductor-metal devices. Specifically, the following inquiries are addressed:

- How does spatial (localized vs. global) density manipulation affect device performance?

- How do microscopic exclusively quantum energy terms of a 2DCS affect macro-
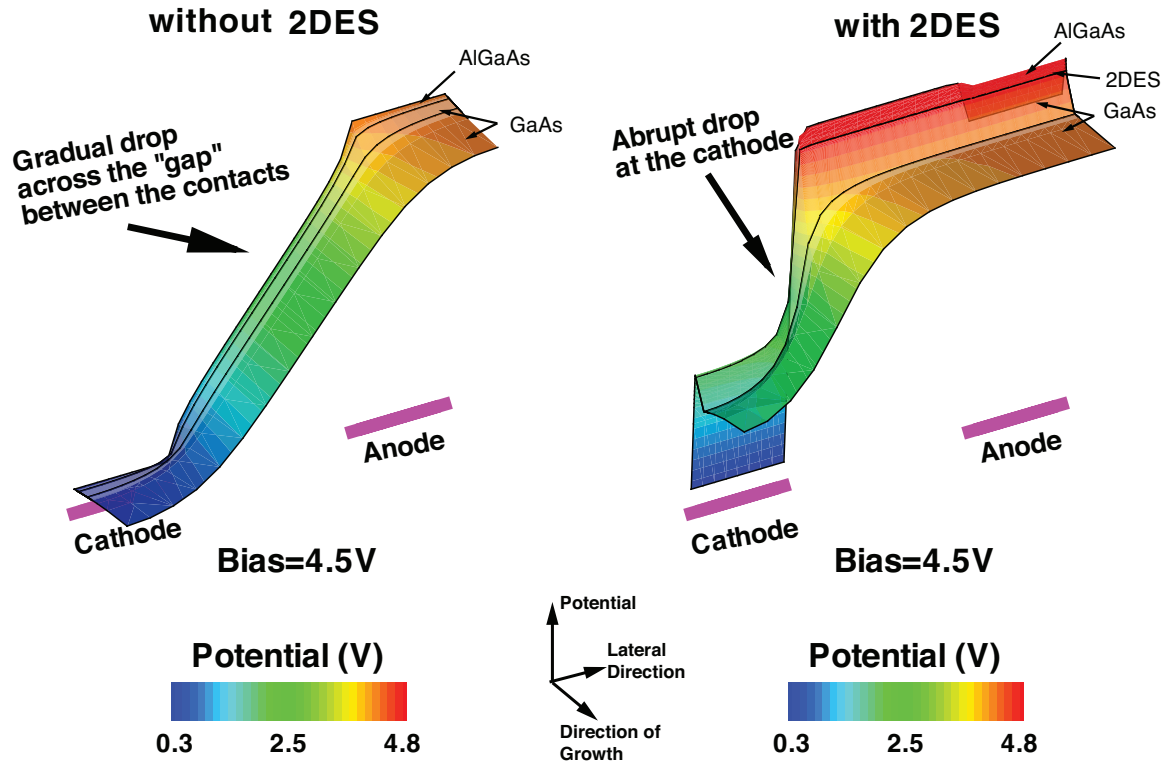
Figure 1.5: Calculated conduction band energy for HMSM devices under $4.5V$ of bias voltage and *without* a 2DES (left) and with an *embedded* 2DES (right).

scopic functions?

- What engineering application does such an unconventional device have?

### 1.6.2  Methodology

A phenomenological approach is taken to describe the capacitive behavior of a new family of unconventional devices. The design of these devices are based on MSM structures with embedded 2DCS. This selection benefits from ease of fabrication as the planar architecture of MSMs is compatible with that of the HEMTs. Hence, no major challenge is expected in growth of the layer structure and fabrication of the contacts. Furthermore, GaAs is selected as the substrate for all of the devices that are discussed in this dissertation. Since GaAs is a direct-band-gap material, the

unconventional devices are suitable for photonic applications.

The design of the layer structure for the devices is performed with the aid of numerical calculations by a self-consistent Poisson-Schrödinger equation solver. Metalorganic vapor phase epitaxy (MOCVD) is used for growth of the layer structure, which is performed by IQE plc, a commercial semiconductor manufacturing company. Fabrication of contacts on the devices is done by standard e-beam and optical lithography methods at Drexel University, Philadelphia PA, Brookhaven National Lab, Upton NY, and Institute for Microelectronics and Microsystems, Lecce Italy.

The MSM-2DCS devices are mainly characterized by capacitance- and current-voltage measurements. The measurement apparatus includes an HP4284A LCRmeter and a Keithley 6487 pico-ammeter to obtain the capacitance and current values, respectively. These measurements were conducted under various conditions including at dark, under illumination, at cryogenic temperatures, and under magnetic field.

Finally, the unconventional devices were modeled and analyzed, numerically and theoretically. Synopsys Sentaurus$^{TM}$ simulation package was used for semi-classical calculations and visualization of electric field, energy band diagram, and carrier concentration in devices. Poisson and drift-diffusion equations were solved for this purpose. Physics of many-body quantum systems were studied and implemented for description of the exotic features in the capacitance-voltage (C-V) characteristics of the MSM-2DCS devices.

### 1.6.3   Contributions of this dissertation

In this dissertation, significant electronic properties of two-dimensional fermion systems (2DFS) are presented, in both verification of theories of quantum mechanics and in engineering applications in electronics, photonics and optoelectronics. A new family of unconventional devices is designed, fabricated, characterized, and analyzed.

The main design feature of these unconventional devices is embedding of a 2DCS in the planar structure of an otherwise conventional MSM photodetectors. The capacitive performance of these unconventional MSM-2DFS devices are characterized by performing admittance spectroscopy measurements under various experimental conditions. Specifically, the C-V characteristics of these MSM-2DFS devices, exhibit large dependencies on applied bias voltage and/or the intensity of the incident illumination. A giant capacitance enhancement (CE) in the C-V characteristic is the distinct feature of this device. The amount of CE can be manipulated by applying a bias voltage or deposition of light-generated carriers. This remarkably improves the performance of the MSM-2DCS device as a voltage controlled capacitor and provides a new method for capacitance-based photodetection. This capacitor is modeled by accounting for the quantum mechanical exchange and correlation energy term in the interacting 2DCS. The theories of operation that are developed in this dissertation can be implemented for more complex devices, such as edge 1-dimensional electron systems and nanowires.

### 1.6.4   Outline of the chapters

Chap. 1 of this dissertation discusses the significance of the two-dimensional charge systems, and provides a review on performance of the conventional meta-semiconductor-metal structures. Specifically, the unique physical features of a 2DCS and the material systems at which it can be achieved are presented at Sec. 1.1. Properties of many-electron systems are described at Sec. 1.2 and the distinctions between a classic vs quantum mechanical approach are constituted. At Sec. 1.3, common methods for manipulation of properties of a (classic and quantum) many-electron system are explained. Sec. 1.4 presents the functionalities that may be obtained by inclusion of a 2DCS in semiconductor devices, with an emphasis on its application in

varactors. Finally, Sec. 1.5 reviews the performance of MSM photodetectors as a basis for the unconventional MSM-2DCS devices that are discussed in this dissertation.

In Chap. 2 an unconventional MSM device with an embedded 2D electron system (2DES) is introduced. The design specifics and performance characteristics of this device are discussed at Sec. 2.2 and a model is implemented for the device based on semi-classical calculations on the electric field and electron density in the device. In Sec. 2.3 the C-V characteristics of the MSM-2DES is inspected and various applications are identified for the MSM-2DES device. It is shown that this device is a varactor with record breaking figures-of-merit. Sec. 2.4 discusses sub-families of MSM-2DES device in which slight structural modifications in the device layer structure alter the 2DES density; hence new functionalities for these devices are identified.

The theoretical background of quantum many-electron systems is presented in Chap. 3. Specifically, the formalism for 2D fermion system is described in Secs. 3.2, 3.3, and 3.4 and quantum exchange and correlation energies are identified in Secs. 3.3 and 3.4. The concepts of compressibility and phase transition are described in Secs. 3.2 and 3.3. Furthermore, the concept of the capacitance as an energy storage device is revisited in Sec. 3.5 and exchange and correlation capacitances are defined at Sec.3.5.4.

Manipulation of exchange and correlation energies by a bias voltage and light-generated carriers are discussed in detail at Chap. 4. The "Batman" shape capacitance enhancement in the C-V of the MSM-2DES capacitor is explained based on manipulation of exchange and correlation energies of the 2D layer in Sec. 4.1. At the same section, a capacitance-mapping technique is used to investigate the source of a giant "sail" shape enhancement in capacitance of MSM-2DES device under light. Energy moderations inside the edge of the 2DES, as a quasi-1D electron system, may hypothetically account for the "sail" CE. Finally, an MSM device with an embedded

2D hole system is introduced at Sec. 4.2. In this device the density of the hole layer is judiciously design to remain below a critical value in dark. With an incident illumination, the density is raised above the critical value by deposition of light-generated carriers. This appears as giant "Batman" shape CE in the C-V characteristics under light, while totally absent in the dark. Hence, a new capacitance-based photodetection mechanism is suggested at Sec. 4.2.

Finally, at Chap. 5 the contributions of this dissertation are once again reviewed at Sec. 5.1. A road map for future work is defined, mainly in applying the concepts of many-electron systems to more complex structures. Specifically, an MSM-device with bi-layers of electron and hole, and 1-dimensional core-shell nanowire structures are suggested at Secs. 5.3 and 5.4, respectively, that are potential candidates for further in-depth investigations.

## 2. A versatile MSM device with an embedded 2D charge system

### 2.1   Introduction

Conventionally, metal-semiconductor-metal structures are used as photonic devices for photon detection through transport of light-generated charge carriers. Such devices perform based on transport properties of light generated mobile charge carriers and associated considerations, as was discussed earlier in Sec. 1.5. It is desirable to reduce carrier travel path, while maintaining absorption cross section to be high. This requires inclusion of new mechanisms for collection of carriers, other than the mere field-assisted collection. With embedding of a 2DCS layer inside a layer structure, the dominant horizontally-oriented electric field of a planar device can be altered into a vertical field. In this chapter an unconventional metal-semiconductor-metal device with a 2D electron system is described, modeled and analyzed. This device exhibit remarkable performance characteristics as a variable capacitor.

### 2.1.1   Semi-classical approach for device analysis

As mentioned in Chap. 1, in quantum mechanics a system of particles is completely described by a set of wave functions. The significance of these functions is in their representation of likelihood of finding a particle in a specific location and at a certain time. Additionally, according to the Planck-Einstein equation the energy of the system can only take discrete values. Equivalently, the energy of the system is quantized. A mathematical model that includes both of the features of wave-matter duality and quantization of energy is the Schrödinger equation. The solution to this linear partial differential equation is a set of eigenfunctions and eigenvalues that corresponds to the wave functions, $\Psi$, and allowed energy levels, $E$, of a given system,

as the following:

$$i\hbar\frac{\partial}{\partial t}\Psi = \hat{H}\Psi, \tag{2.1}$$

in which $\hbar$ is the reduced Planck constant, $\hat{H}$ is the Hamiltonian operator that represents the total energy of the system, similar to classical mechanics. It includes the kinetic energy operator, $\hat{T}_i$ for the particle $i$, as well as the potential energy operator, $\hat{V}$:

$$\hat{H} = \sum_i \hat{T}_i + \hat{V}. \tag{2.2}$$

The Hamiltonian operator, $\hat{H}$, is defined according to the specifics of a given problem. In the Scrödinger picture, however, it is assumed that the Hamiltonian is time independent and any time evolution is included in the wave function only [108]. Consequently, the state function can be separated into two part:

$$\Psi(r,t) = \psi(r)\tau(t). \tag{2.3}$$

$\psi(r)$ is found through the solution to the time-independent Schrödinger equation:

$$\hat{H}\psi = E\psi \tag{2.4}$$

The overall state function, hence becomes $\Psi(r,t) = \psi(r).e^{\frac{-iEt}{\hbar}}$. Equivalently, the state function propagates periodically in time with a space position probability density of $\psi(r)$. It is customary to apply Dirac's notation for state function and operators, hence for the Schrödinger picture, the state vector becomes:

$$|\Psi_s(r,t)\rangle = e^{-i\hat{H}t}|\Psi_s(r,0)\rangle \tag{2.5}$$

Here the subscript $s$ indicates a state vector obtained through applying the Schrödinger

picture. In typical electronic devices, that are based on solid crystal structure, the periodicity of the lattice, with wave vector $k$, is introduced to the Schödinger equation of Eq. 2.4. By applying Bloch's theorem [109], the energy eigenstates for an electron in the crystal can be written as Bloch waves:

$$|\Psi_s(r)\rangle = e^{ik.r}|u(r)\rangle, \qquad (2.6)$$

in which $|u(r)\rangle$ is a periodic function with the same periodicity as the crystal. Applying Eq. 2.6 to crystals established the well-known *electronic band theory* (EBT) by which many physical properties of solids, such as electrical resistivity and optical absorption can be explained. Specifically, EBT simplifies treatment of typical electronic devices by allowing a classical *single electron approach*. It, however, sets constraints on charge carriers through assumption of an effective electron mass, $m^*$, for a lattice, as well as conduction of carriers in separate energy bands. These, altogether, constitute a semi-classical analysis of solid-state devices, in which classical laws of physics control the electronic properties of charge carriers that have the form of a Bloch wave of Eq. 2.6.

## 2.2 "Unconventional" metal-semiconductor-metal devices

### 2.2.1 An MSM-2DES device with an auxiliary p-type delta doping

A 2D electron charge is introduced to a planar HMSM structure, by a triangular quantum well (QW), and by replicating the techniques of using a delta-doping profile, which is routinely applied for high electron mobility transistors (HEMTs). The distinctive difference of the resultant device, with HEMTs, is on the type of the metal-semiconductor contacts. While the latter has two Ohmic contacts, as drain and source, connected to the 2D channel, here two Schottky metal-semiconductor contacts

are fabricated on top of the layer structure. This significantly simplifies the device fabrication process, as it does not require any annealing requisite for Ohmic contacts. Such MSM devices with an embedded 2D charge system was previously proposed and characterized by our research group and others [29, 36, 77, 81, 110, 111, 112].

In this dissertation, a new MSM device with a 2D electron system (2DES) is proposed, in which an auxiliary p-type doping layer, in addition to the main modulation profile, is used to increase band bending and to enhance confinement of electrons inside the quantum well. This is shown in detail in Sec. 2.2.1.1.

### 2.2.1.1 Layer structure

On a GaAs buffer layer, $500nm$ GaAs was grown by molecular beam epitaxy (MBE), followed by $50nm$ of $Al_{0.3}Ga_{0.7}As$. An n-type $5.0 \times 10^{12}cm^{-2}$ Si delta-doping (DD) layer was grown $5nm$ away from the hetero-interface on the AlGaAs side to produce free 2D cloud of electrons in GaAs, similar to HEMTs. In addition, growth of a p-type (C-doped) $6.25 \times 10^{11}cm^{-2}$ DD layer $100nm$ away from the interface on the GaAs side increases band bending, hence carrier confinement, which was shown by Hall measurement at $300K$ to be $6.2 \times 10^{11}cm^{-2}$ at AlGaAs/GaAs interface. Schottky contacts were defined by optical lithography, Ti (10 nm)/Au (90 nm) metal deposition, and subsequent lift-off. Measured low dark currents–in picoamp range– indicate a negligible effect of surface states at metal-semiconductor interface. The specifics of the contact layouts are shown in Figs. 2.1 and 2.2 at this chapter and in Fig. B.2 at Appendix.B, and will be discussed in Sec. 2.2.1.2. The calculated energy band diagram (EBD) of the doped wafer, in a direction normal to the contacts and at equilibrium, is shown in Fig. 2.1(b). The calculations are performed by a one dimensional self consistent Poisson-Schrödinger solver [113]. A triangular quantum well (QW) is formed at the GaAs/AlGaAs hetero-interface and on the GaAs side.
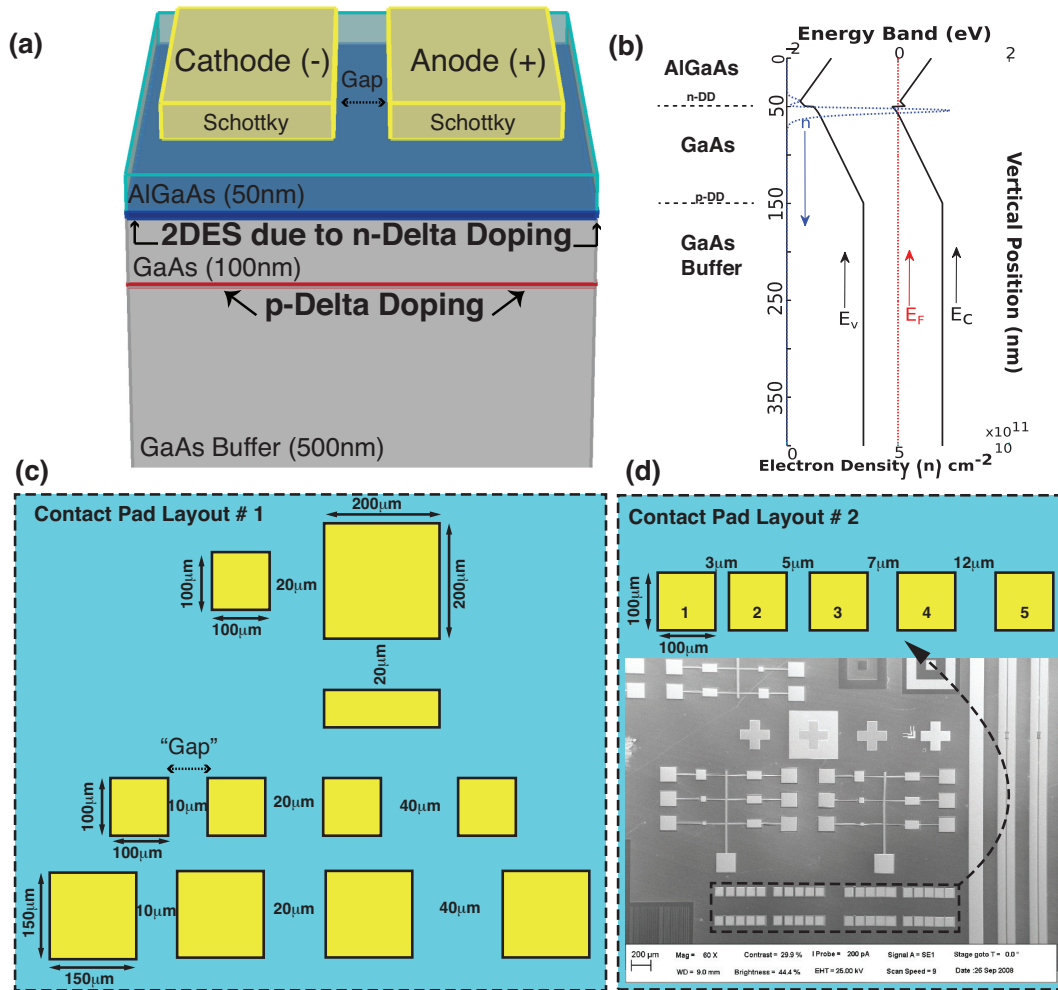
Figure 2.1: a) Layer structure for the MSM-2DES devices, b) calculated energy band diagram and carrier concentration in the growth direction, c,d) contact layout specifics.

The QW is populated by electrons as indicated by the Fermi level position.

### 2.2.1.2 Device Layouts

Several contact patterns were fabricated on the substrate in different layouts, each of which assists in probing different metrics of device performance. Specifics of these designs are indicated in Figs. 2.1,2.2, and B.2. All the devices discussed in this dissertation follow the similar naming convention for their contact geometry. Mainly, the

TLM structures [114] were fabricated with various spacings in a $0.5 - 40\mu m$ range. Two contact sizes were selected: a "small" $100 \times 100\mu m^2$ and a "large" $150 \times 150\mu m$ with a square shape geometry. Any two adjacent contact pads in a TLM structure constitute a single device, and the majority of the devices here incur such format. Several other geometries were also fabricated that include eccentric circular pads, interdigitated structure with Ground-Signal, Ground-Signal-Ground, and Transmission Line connection pads. The characteristics of the devices with the more complex geometries, however, carry numerous interesting features, and the respective physical explanation can exhaust the intention of this dissertation. Hence, such characteristics are addressed in the appendices.
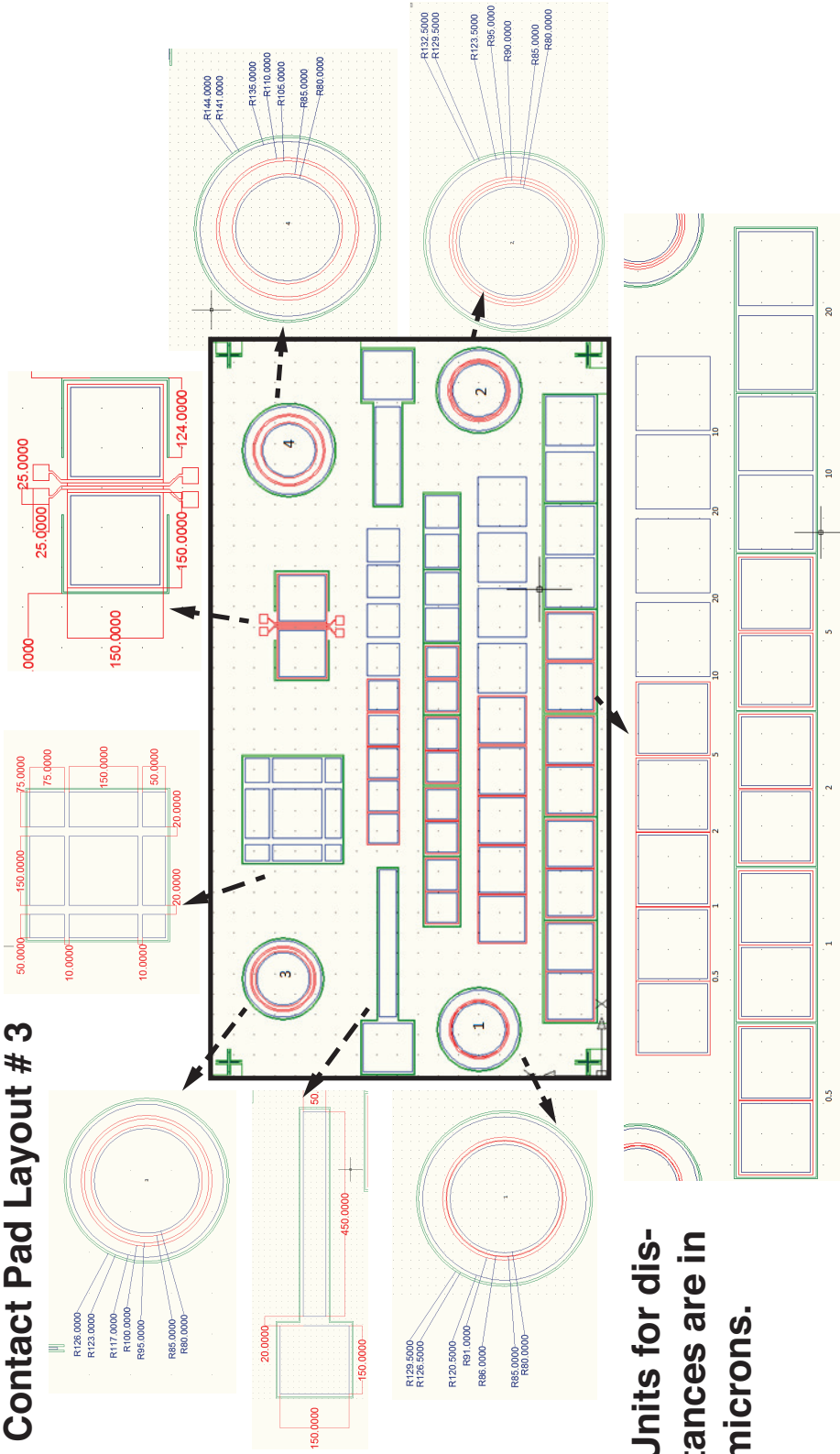
Figure 2.2: An additional contact layout for the fabricated MSM-2DES devices.

### 2.2.2 A control MSM device with suppressed 2DES

A second set of identical devices to the MSM-2DES ones were also fabricated that suppressed the 2DES through the omission of n-delta doping layer from the growth process. These control devices were intended to probe the influence of the 2DES on the performance of the device. It is to be noted that the layer structure for the control MSMs still include the auxiliary p-doping layer.

### 2.2.3 Electric field distribution in an MSM-2DES device

Fig. 2.3 shows the calculated electric field inside the MSM-2DES, at equilibrium and under a finite bias value. They show that the electric field distribution inside the device has a dominant vertical component. This is in contrast with the electric field inside conventional MSM, that was shown in Chap. 1 (Fig. 1.3). Hence with placement of a 2D charge layer inside a conventional MSM, the electric field landscape changes from a horizontal to a pre-dominantly vertical format. This has been shown to enhance the performance of this device for fast photodetection.

In order to probe the subsurface electric field, electron beam induced current (EBIC) measurement was performed on the MSM-2DES device to verify the electric field calculations of Fig. 2.3. In this technique, an electron beam (e-beam) is incident on the device under test(DUT). The location of the e-beam can be varied precisely, and at each point the current flow through the terminals of the DUT is recorded. The electrons that are induced in the bulk of the device by the e-beam are collected at the terminals. Depending on the local and external electric field, the current recording will be different for every e-beam location. Additionally, since the energy of the e-beam can also be controlled, the depth of penetration of the electron beam inside the device can be changed. Consequently, the current readings bear information on the all the three dimensions of the DUT. Notably, when there is no bias applied to
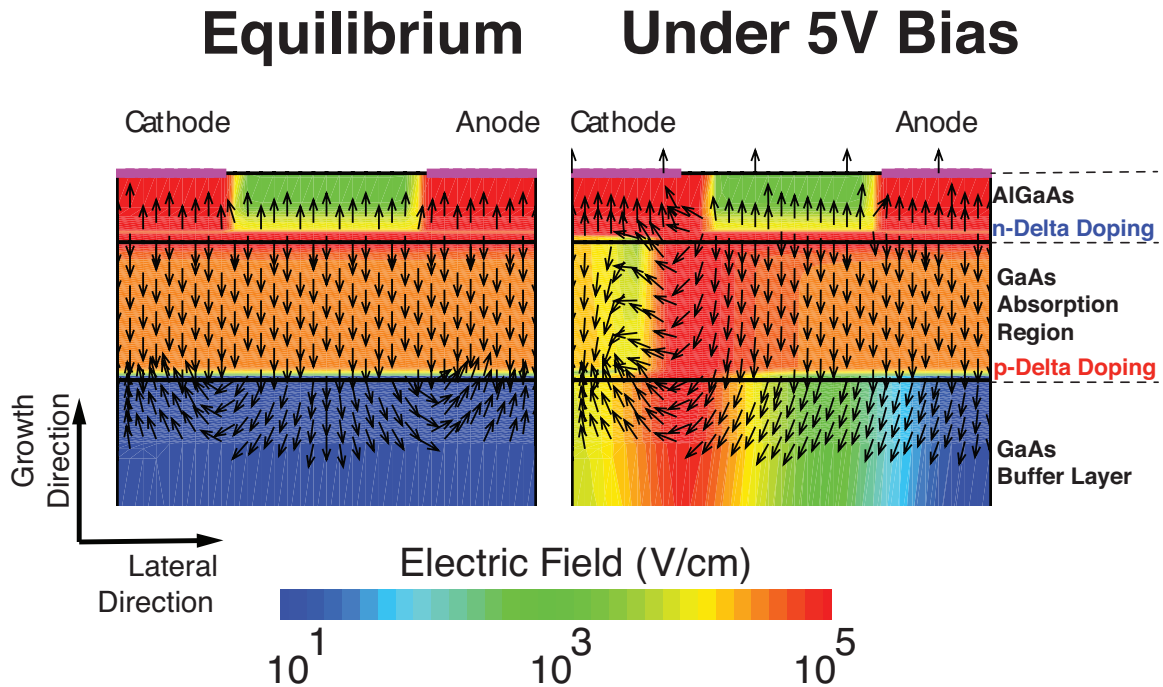
Figure 2.3: Calculated electric field line distribution inside the MSM-2DES device at equilibrium (left) and under $5V$ bias (right).

the terminals of DUT, the EBIC mapping of the device will indicate the energy band structure.

For the MSM-2DES, the planar structure of the device suggests that the measured current by EBIC represents the strength of horizontal component of the electric field. An SEM image and EBIC images of the MSM-2DES device for TLM pattern with $5\mu m$ contact separation are shown in Fig. 2.4. Under equilibrium, a thin bright (dark) band is visible at the edge of cathode (anode). These bands correspond to the fringe electric field lines between the contact edge and the n-delta doping layer (Fig. 2.3). Interestingly, with application of a bias voltage, the width of the edge bands in the EBIC do not increase. This indicates that the electric field can not penetrate horizontally in the region between the contacts, and it is being screened by the 2DES and the delta doping charge layer. This feature has a significant effect in

the capacitive performance of the device, as will be discussed in the following sections.
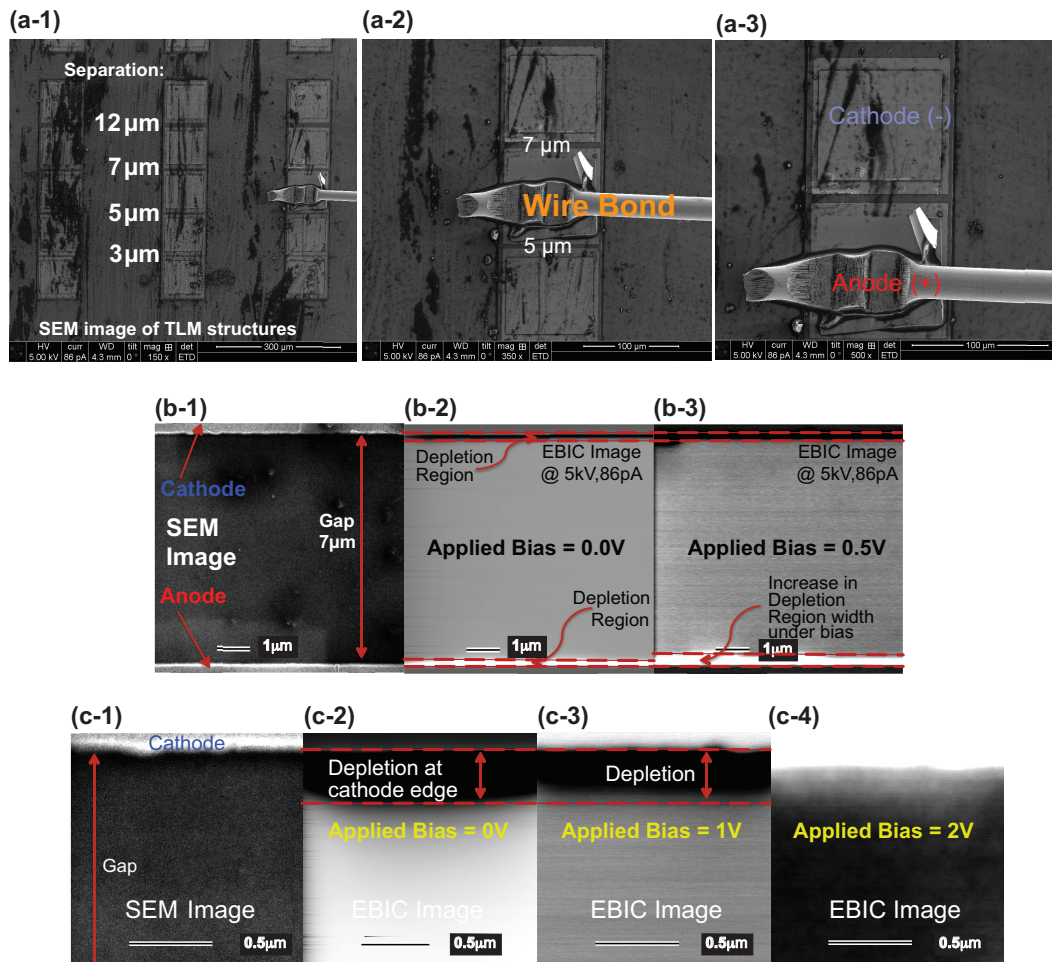


Figure 2.4: a1-3) SEM images of the MSM-2DES devices, b1) SEM image for an MSM-2DES device with $7\mu m$-gap size, b2,3) corresponding EBIC images under various bias voltages, c1) magnified SEM image displaying the region by the cathode edge, and c2-4) corresponding EBIC images under various bias voltages highlighting the depletion region.

### 2.2.4 Electric field distribution in the control device

It is expected for the electric field landscape of the control device to resemble that of a conventional MSM, with more horizontal alignment of the field lines. The calculated field lines, (Fig. 2.5) shows that at equilibrium, the fringe field lines penetrate more into the gap region between the contacts, when compared with that of the MSM-2DES device. Under $5V$ bias, this penetration becomes evident as field line spread into the gap region and closer to the other contact. Noticeably, the existence of the auxiliary p-delta doping layer adds a vertical component to the field line. Overall, the landscape for the control device is a transition between that of MSM-2DES and the conventional devices.
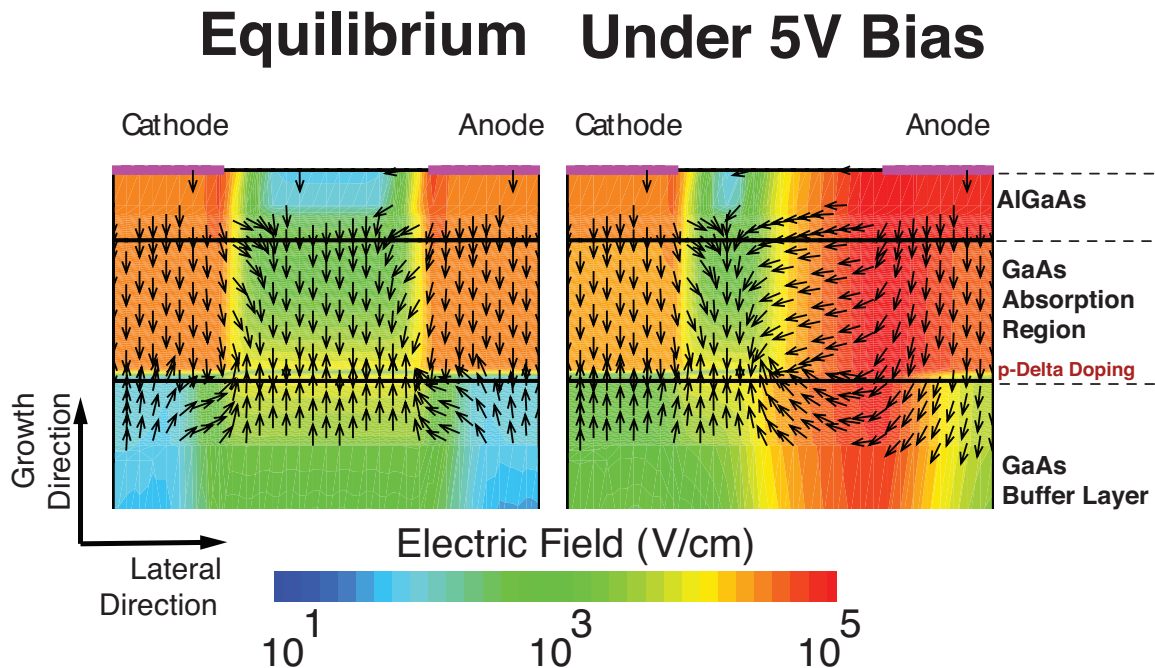


Figure 2.5: Calculated electric field line distribution inside the "control" device at equilibrium (left) and under $5V$ bias (right).

### 2.2.5 Energy band diagram of the MSM-2DES under bias voltage

Calculated conduction band energies under $V_{bias} = 5V$ are shown in Figs. 2.6 for MSM-2DES capacitor and the control device. It indicates that the control device has a gradual voltage drop across the 'gap' region between the contacts, while in the MSM-2DES device all the potential abruptly drops at the cathode edge, and it remains equipotential elsewhere in the device. This is because the preserved 2DES layer screens the electric field lines at the cathode edge and prevents the penetration of field lines in the lateral direction under applied bias.
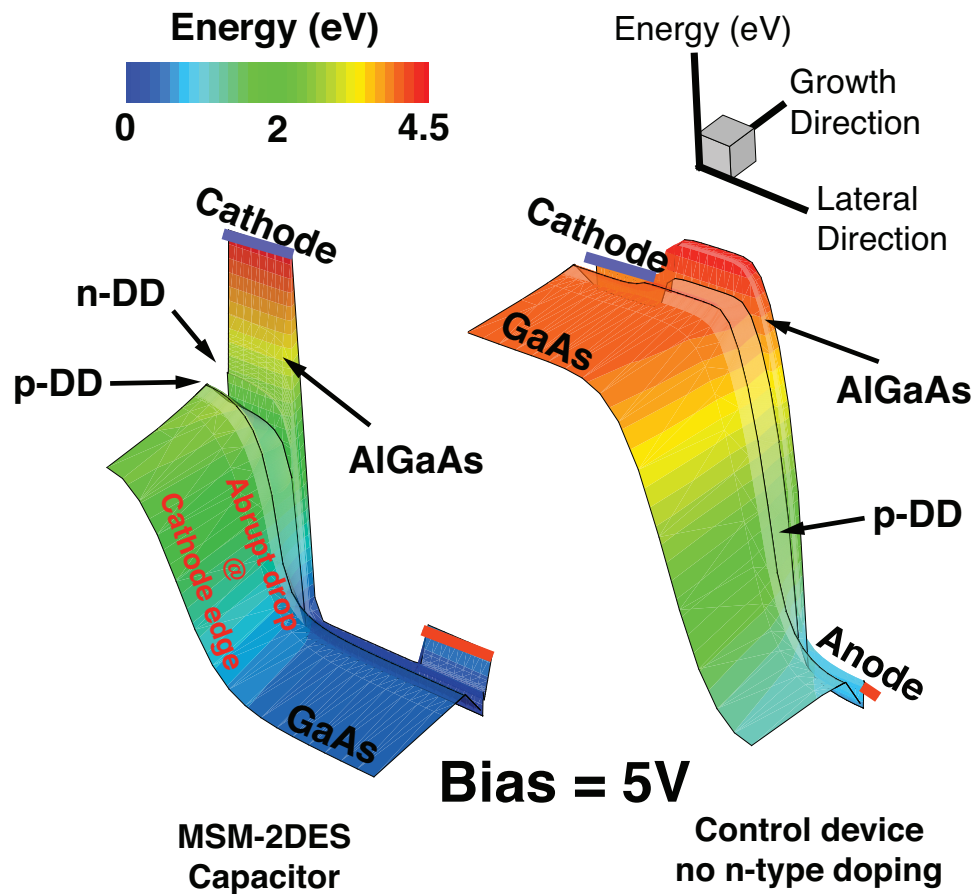


Figure 2.6: Calculated conduction band energy for MSM-2DES (left) and control devices (right) under 5V of bias.

### 2.2.6 Current-Voltage characteristics of MSM-2DES device

The current-voltage (I-V) characteristics of the MSM-2DES device was measured by a Keithley 6487 pico ammeter at room temperature, and shown in Fig. 2.7. The vertical electric field landscape affects the I-V characteristics significantly. Inspection of calculate E-field of Fig. 2.3 indicates that there exists a strong electric field at the cathode edge of the MSM-2DES device, that is further enhanced under bias. The breakdown field of $AlGaAs$ is $E_{Breakdown} \approx 4 \times 10^5$ [115], and the internal electric field exceeds $10^6 V/cm$ under 5V of bias, hence a breakdown is expected. Such prediction is reflected in the I-V characteristics of the "large" MSM-2DES device, also shown in Fig. 2.7, as the current levels reach values greater than $10\mu A$ at $V_{bias} > 4V$. A major contributing factor to the very large dark current of MSM-2DES device is the close placement of the n-type delta doping to the contacts. This results in the formation of a large electric field at the edges, and significantly reduces the breakdown voltage as well. For smaller bias voltages ($0V \leq V_{bias} < 1V$, however, the current level remains less than $10nA$. A transition in the current level is observed at bias range of $1V \leq V_{bias} \leq 3V$, and it reaches saturation at $V_{bias} = 4V$. These current levels are very high, compared to expected values for a conventional HMSM [79], in which the dark current values are typically in a pico amp range, for a device of a comparable size. For charge transport based photodetectors, it is desirable to have a minimal dark current for enhanced noise performance [79, 116]. The MSM-2DES device, hence, does not display proper merits for a low-noise transport based photodetection. In contrast to MSM-2DES device, the control sample has significantly lower current levels in the same applied bias range. Specifically, it remains less than $10nA$ at $V_{bias} \leq 6V$ for the "large" device, which is 3 orders of magnitude less than the MSM-2DES counterpart. Furthermore, the current value scales with the device pad area for the "small" control device. The I-V of the control device does not indicate a consistent trend with the
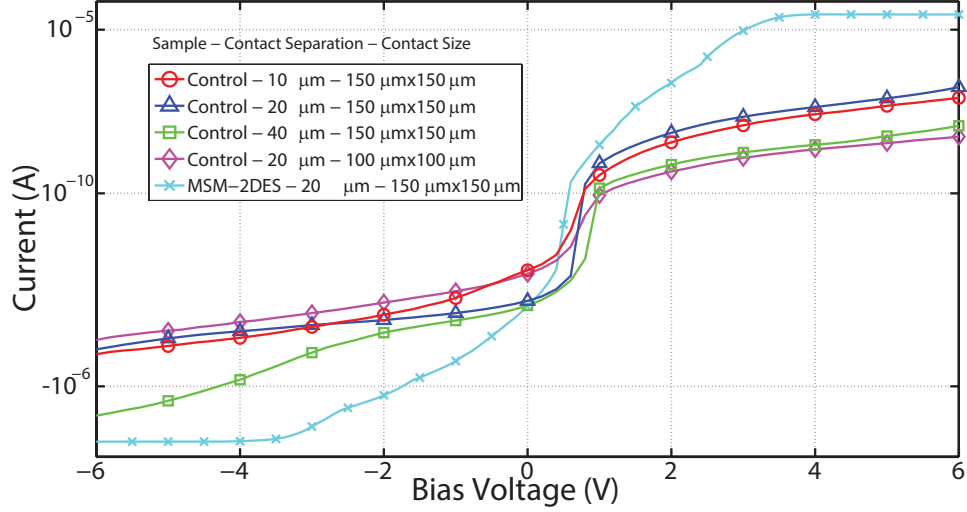
Figure 2.7: Comparison of the I-V characteristics for the MSM-2DES with that of the "control" device.

contact pad separation distance.

### 2.2.7 Capacitive-Voltage characteristics of MSM-2DES device

The capacitances of all the devices reported in this dissertation were measured by a commercial HP 4284A LCR-meter that applied a capacitance bridge balancing technique [117]. In the vector voltage-current method of Fig. 2.8, ac signal $v_i$ with a probe frequency (PF) of $\omega$ is applied to the device under test (DUT) and the device impedance $Z$ is calculated from the ratio of $v_i$ to the sample current $i_i$. A high-gain operational amplifier with feedback resistor $R_F$ operates as a current-to-voltage converter. With the input to the op-amp at virtual ground, the negative terminal is essentially at ground potential, because the high input impedance allows no input current to the op-amp, $i_i \sim i_o$. With $i_i = v_i/Z$ and $i_o = ?v_o/R_F$, the device impedance can be derived from $v_o$ and $v_i$ as [114]:

$$Z = -\frac{R_F v_i}{v_o}, \tag{2.7}$$

where the device impedance of the parallel $G - C$ circuit in Fig. 2.8 is given by:

$$Z = \frac{G}{G^2 + (\omega C)^2} - \frac{j\omega G}{G^2 + (\omega C)^2}.$$ (2.8)

It consists of a conductance, the first term, and a susceptance, the second term. The voltages $v_o$ and $v_i$ are fed to a phase detector and the conductance and susceptance of the sample are obtained by using the 0 and 90 degree phase angles of $v_o$ referenced to $v_i$. The zero degree phase angle gives the conductance $G$ while the 90 degree phase angle gives the susceptance or the capacitance $C$ [114].
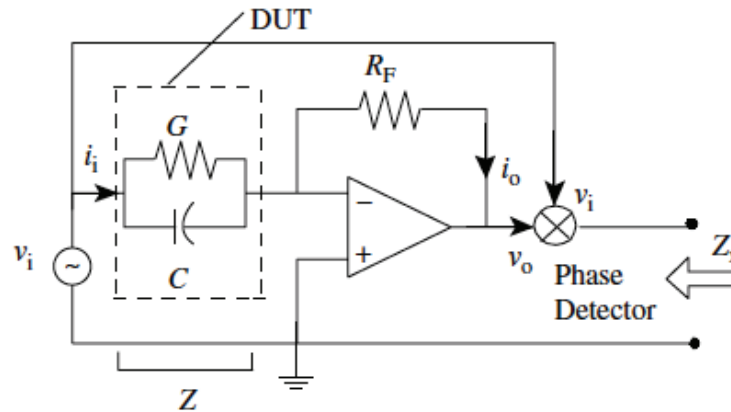


Figure 2.8: Schematic circuit diagram of a capacitance-conductance meter. [114]

C-V characteristics were obtained at various probe frequencies (PF) ranging from $1kHz$ to $1MHz$ at room temperature. Stray capacitance due to measurement apparatus was eliminated by open circuit corrections. The detail of C-V behavior for a "small" device with contact separation of $7\mu m$ is shown in Fig. 2.9. A quasi-flat region is observed in the vicinity of equilibrium capacitance, with higher capacitances at lower probe frequencies (PF). Further voltage increase causes a distinctive "Bat-

man" shaped enhanced capacitance, which starts at a critical voltage of $V_{cr} \sim 2V$ and ends at a threshold voltage, $V_{th}$ of 2.8$V$; it is followed by an abrupt decline into negative capacitances (NC). As depicted in Fig. 2.9, both capacitance enhancement and NC characteristics are frequency dependent with the former observed up to probe frequencies as high as $100kHz$ and more pronounced at lower frequencies, while NC inversely diminishes as PF increases, and disappears for $PF > 50kHz$. The observed CE may reach as high as 26.8%. All of the curves approach the same minimum capacitance with further increase in bias.

MSM-2DES device with other contact separations exhibit similar behavior. Notably, the capacitance values for all the separations coincide with each other at $V_{bias} < V_{th}$, suggesting the insignificant influence of contact separation on pre-threshold capacitance. Additionally, as indicated in Fig. 2.9, as the bias is increased above threshold, the capacitance drops from a large maximum to a small value that is lower than the (geometric) capacitance of coplanar metal plates on this semiconductor.

Comparison of the C-V characteristics for the MSM-2DES capacitor and that of the control device indicates distinctions in the performance of the two sample. The C-V for control devices, displayed in Fig. 2.10, shows fundamental differences with that of the MSM-2DES's, in both pre- and post-threshold capacitances; they also lack the CE and NC. At 0, 2 and 4.5V of $V_{bias}$, the capacitance ratio for the MSM-2DES to control devices are 4.6, 104.2 and 0.21 at $PF = 10kHz$, signifying the effect of the n-delta doping and the 2DES on capacitive performance of the device.

### 2.2.8 Effects of measurement parameters on capacitance of MSM-2DES device

The measurement parameters in the LCR-meter can be varied to obtain further insight on device characteristics. Specifically, the amplitude and frequency of ac os-
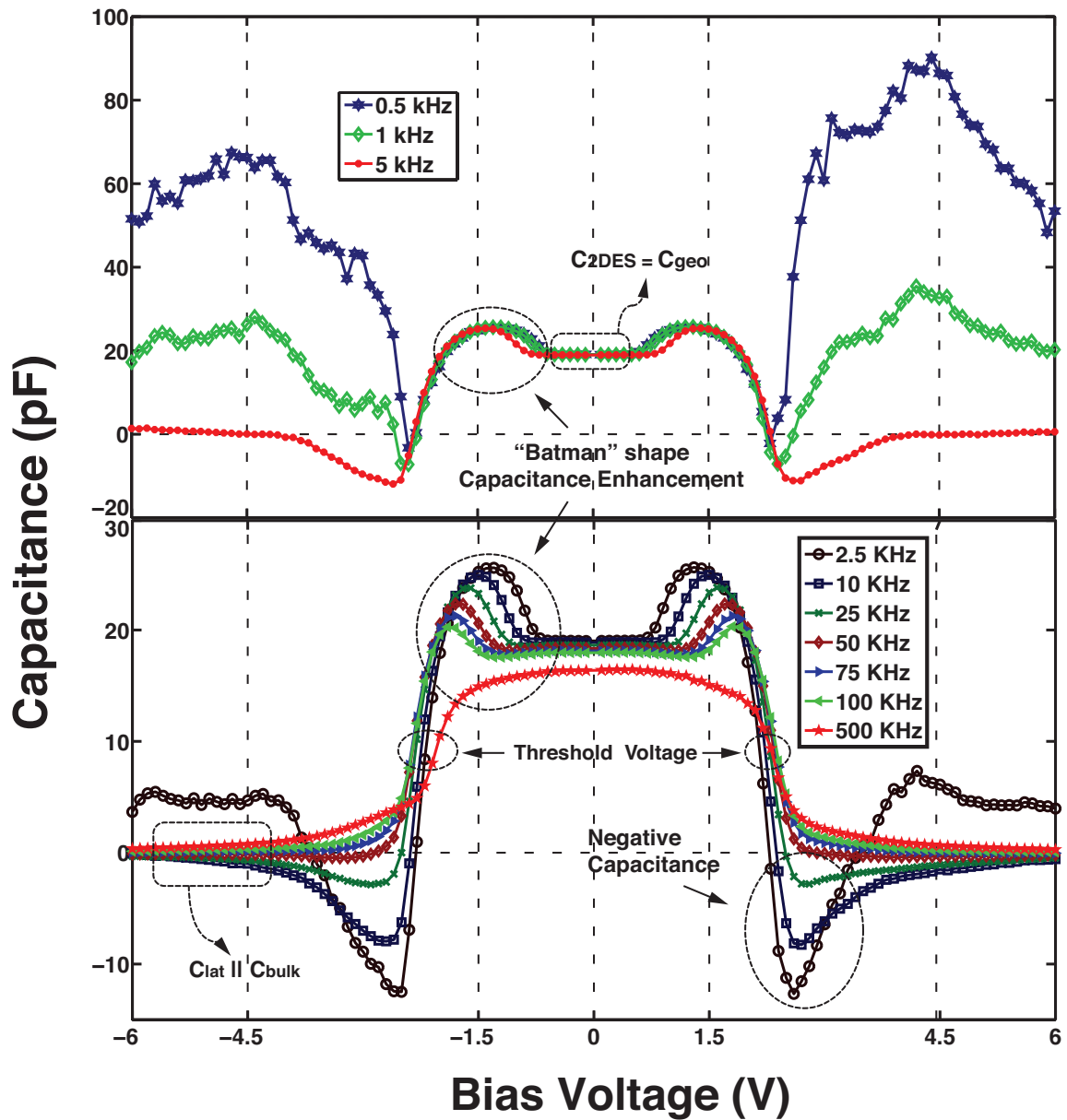
Figure 2.9: C-V characteristics for the "small" MSM-2DES capacitor at various probe frequencies.

cillating (probe) voltage can bear information on the dynamics and the electronic structure of the device [114]. Here the capacitance vs the probe frequency and the amplitude of the ac voltage are presented for the MSM-2DES device. The measurements are taken under various DC bias voltages, at which the device exhibits
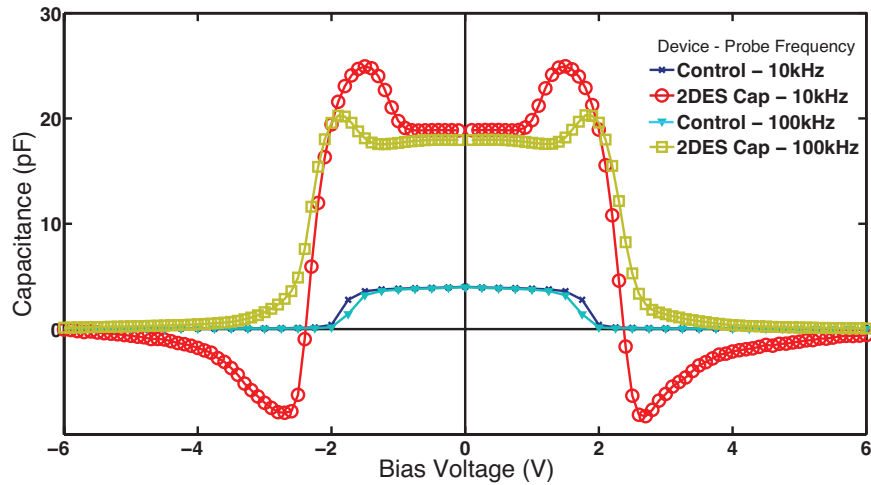
Figure 2.10: Comparison of C-V characteristics of MSM-2DES capacitor with that of "control" device.

interesting features, such as the capacitance enhancement and negative capacitance.

**Probe Frequency:** Fig. 2.11 indicates the dependence of the capacitance of the MSM-2DES capacitor on Frequency. The measurements were performed by using the same LCRmeter, under various DC bias voltages and with a $50mV$ ac excitation.

High density of surface states at the $GaAs/AlGaAs$ interface and fast interface states in the heterojunction with peak densities close to GaAs conduction band edge have been previously suggested [118, 119] to account for frequency dependence of the equilibrium capacitance of a modulation doped GaAs/AlGaAs HEMT. Similar characteristics was also observed for $C_{0V}$ of the MSM-2DES device. Since the layer structures of typical HEMTs [30] and this MSM-2DES capacitor are closely related, it is feasible for the interface states to account for the equilibrium frequency response. This can be further verified by measurement of the AC-conductivity (G) on MSM-2DES capacitor, performed by the same LCR meter, and displayed in Fig. 2.12, follow the previously observed trend of abnormal increase in G at high probe frequencies where fast capture of electrons by interface defect states and slow re-emission in
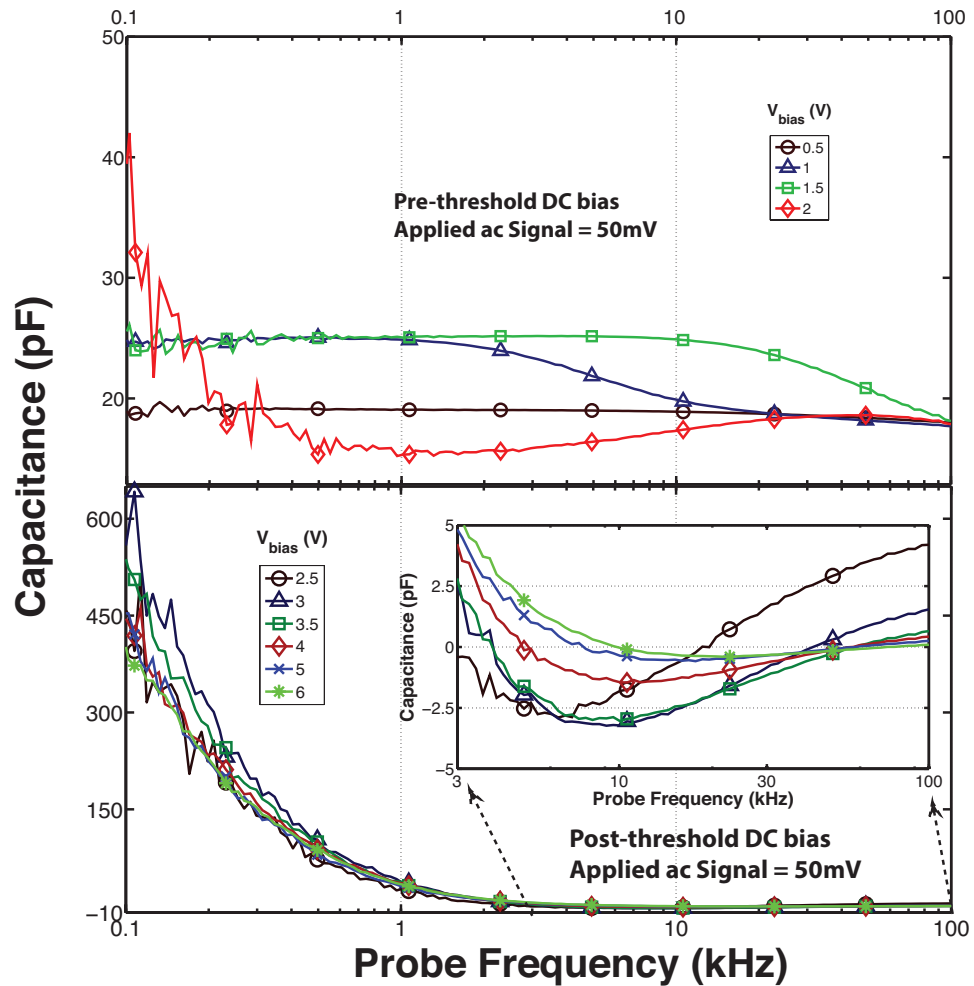
Figure 2.11: Capacitance evolution with the probe frequency, measured at various DC bias voltages and at $V_{ac} = 50mV$.

conjunction with an additional transport path through the series resistance of the 2DEG, increase the ac conductivity [118].

Furthermore, the capacitance values at pre-threshold bias voltages of $0.5, 1.5,$ and $2V$ exhibit very different dependencies on applied probe frequency. While the capacitance value at $V_{bias} = 0.5V$ remains rather constant at $18.9pF$ with variations of PF, at $V_{bias} = 1.5$, where the "Batman" shape in C-V is observed, the capacitance is constant at $25.1pF$ for $PF < 10kHz$ and drops linearly until it converges to the
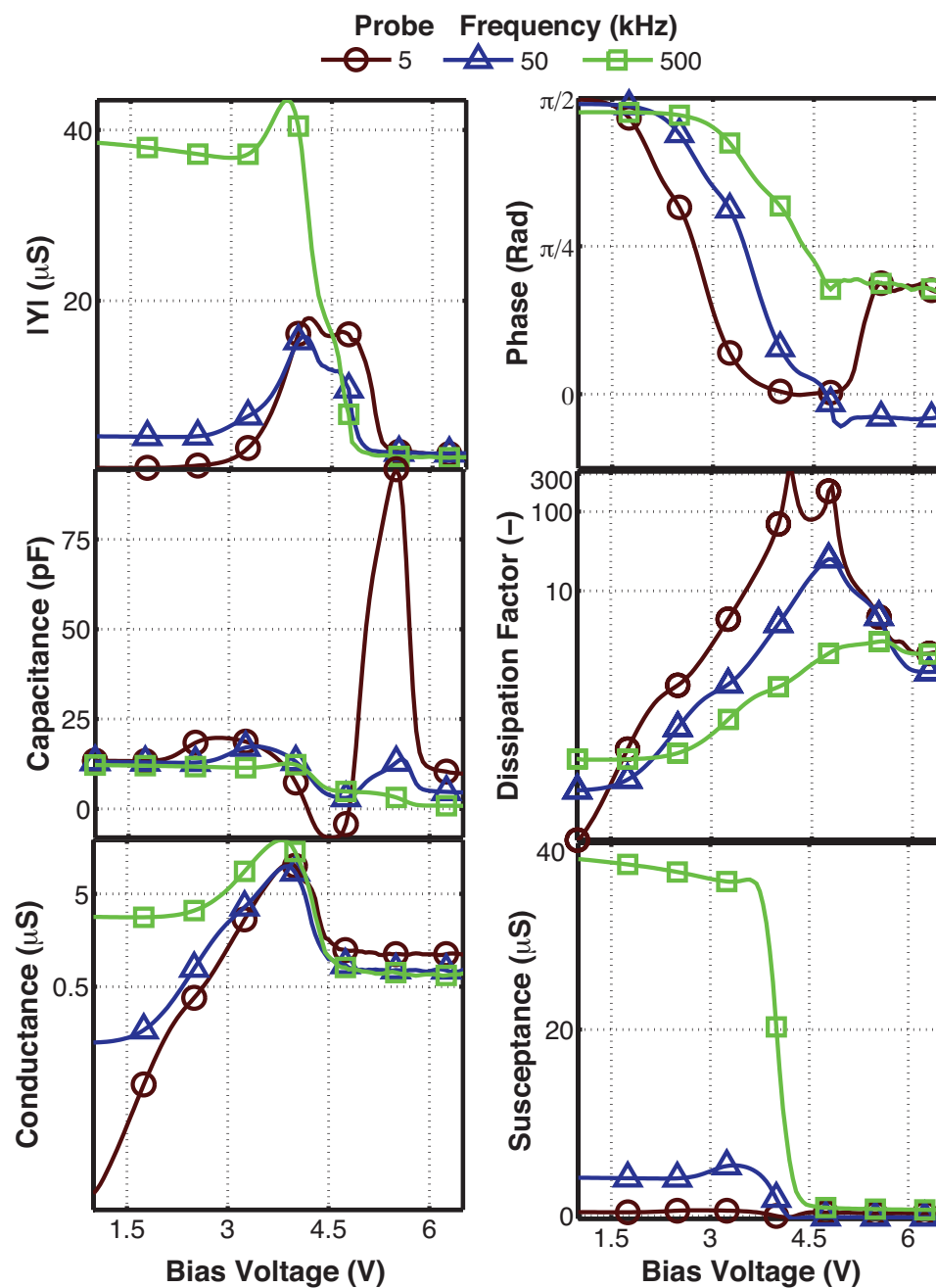
Figure 2.12: From left to right and in the order: top) amplitude and phase of admittance, middle) capacitance and dissipation factor, and bottom) conductance and susceptance, vs voltage characteristics for the MSM-2DES device with $20\mu m$ of separation for contact pads.

equilibrium value of $15.2pF$ at $PF = 100kHz$. For $V_{bias} = 2$ that corresponds to the threshold voltage in the C-V, the frequency response exhibits a non-linear behavior with capacitance values taking a maximum and minimum values of 42.0 and $15.2pF$ at PFs of 100 and $960Hz$, respectively. It increase and converges to the equilibrium value $17.8pF$ at $PF = 100kHz$. Such descriptions in frequency response at pre-threshold bias voltages infers existence of multiple charge mechanisms in the MSM-2DES device.

The post-threshold capacitances for different bias voltages indicate similar trends with variations of probe frequency. Specifically, for $PF < 3kHz$ all the values remain positive and can be as large as $600pF$ at $PF = 100Hz$. The capacitance become negative at $3kHz < PF < 50kHz$. with further increase in PF, all the capacitance values become positive and rather constant with frequency. For $PF > 75kHz$, the capacitances remain less than $4.1pF$, and for larger bias voltages converging to smaller capacitance values.

**Oscillating Voltage:** The capacitance of the MSM-2DES capacitor also exhibits dependence on the applied oscillating voltage. Such behavior is shown in Fig. 2.13, for a measurement performed on the "small" MSM-2DES capacitor with $5\mu m$ pad separation. All the data were acquired under a $50kHz$ probe frequency and at various DC bias voltages. Interestingly, a stairway feature is observed in the $C - V_{osc}$ characteristics, when the device is biased at the threshold or in the depletion regions. This behavior typically exhibits an abrupt jump or drop in capacitance at $V_{osc} = 93, 193, 374,$ and $494mV$. Table 2.1 summarizes the features of capacitance with variations in the probe voltage amplitude.
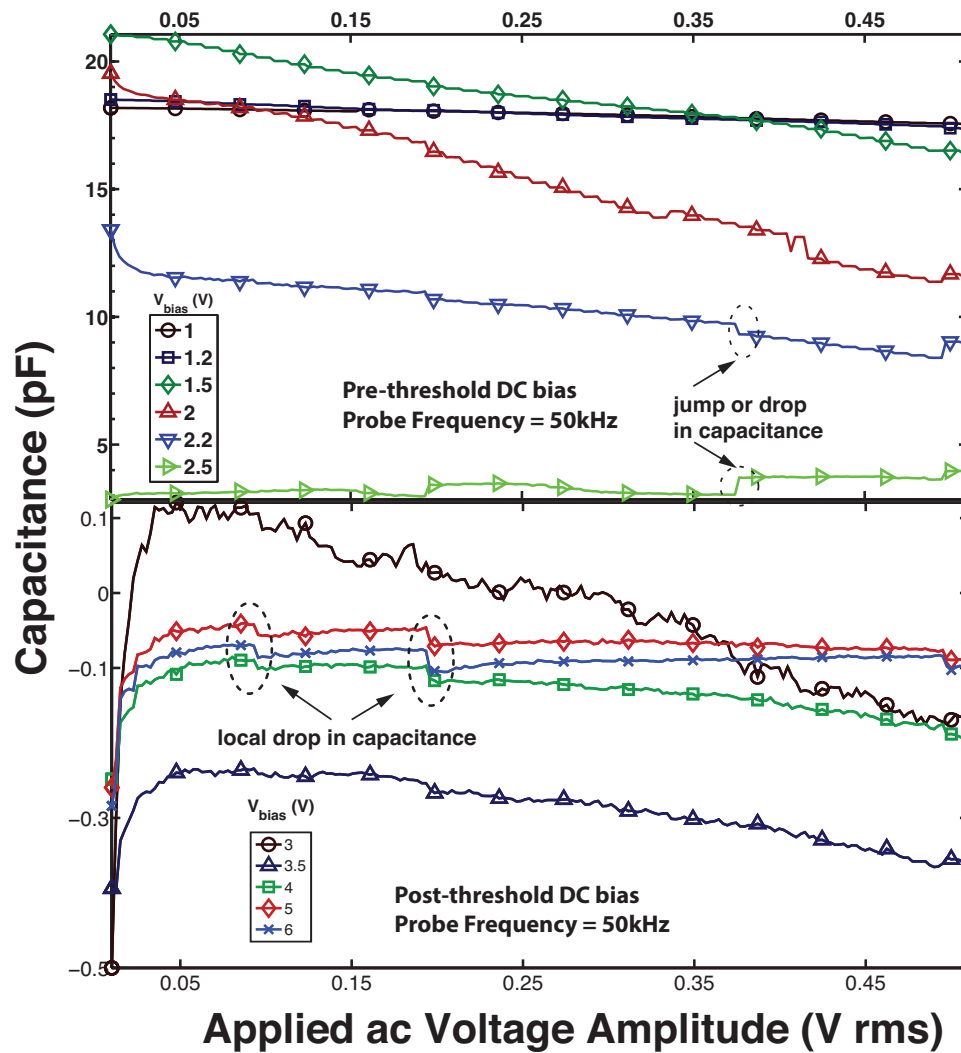
Figure 2.13: Capacitance evolution with the applied ac signal across the device, measured at various DC bias voltages and at $PF = 50kHz$.

Table 2.1: Summary of features for capacitance vs. ac probe voltage amplitude.

| Feature in the C-V (Bias range (V)) | Capacitance Evolution with $V_{osc}$ |
| --- | --- |
| Pre-threshold equilibrium $(0 \leqslant V_{bias} \lesssim 1.5)$ | Negligible change with $V_{osc}$ |
| "Batman" shape CE $(1.5 \lesssim V_{bias} \lesssim 2.2)$ | Descending gradually as $V_{osc}$ increases |
| Threshold $(2.5 \lesssim V_{bias} \lesssim 3.5)$ | A stairway behavior. Abrupt drop of jump at $V_{osc} = 193,\ 374$ and $494mV$ |
| Negative C $(3 \lesssim V_{bias} \lesssim 4)$ | A steep increase for $0 < V_{osc} < 50mV$ and a gradual descend for $V_{osc} > 50mV$ Change of sign occurs for lower DC biases. |
| Depletion $(V_{bias} \gtrsim 4)$ | A descending stairway behavior. Drops at $V_{osc} = 93,\ 193,$ and $494mV$. |

### 2.2.9 Charge control model for device capacitance

Fig. 2.14(a) depicts a schematic of a modulation doped field effect transistor (MODFET). A quasi two dimensional electron system is formed at the $AlGaAs/GaAs$ interface, and inside a triangular quantum well (QW). Typically the first discrete energy levels ($E_0$ and $E_1$ in Fig. 2.14(b)) are filled and the rest of the energy levels can be ignored. In this case the surface carrier concentration $n_s$ of the 2DES is given by [120]:

$$n_s = \frac{\varepsilon}{qd}[V_g - (\phi_b - V_{P2} + V(d_i^+) - \Delta E_C)]., \tag{2.9}$$

where $\phi_b$ is the Schottky barrier height, $V_g$ is the gate voltage, and $V_{P2}$ is the pinch-off voltage of the AlGaAs layer. Furthermore, $\Delta E_C$ is the conduction band offset at the $GaAs/AlGaAs$ interface, and $V(d_i^+)$ is the potential at the interface on the

$GaAs$ side, which can be calculated through continuity of the displacement field at the interface. Eq. 2.9 simply gives the charge induced in a parallel plate capacitor formed by the gate and the 2DES separated by the $AlGaAs$ layer.
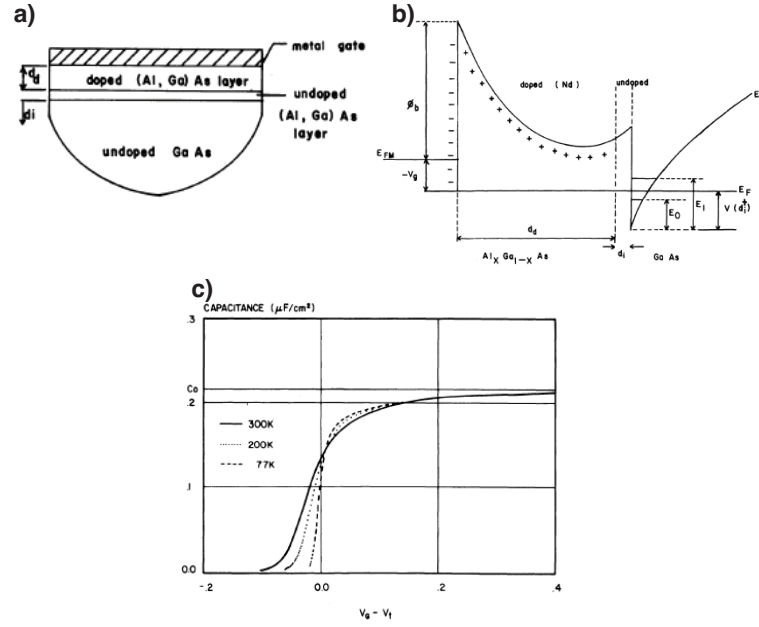


Figure 2.14: a) Schematic, b) Energy band diagram, and c) C-V characteristics of a MODFET calculated by the charge control model (CCM) of Shur [30].

A *differential capacitance*, $C_{diff}$, can then be defined as:

$$C_{diff} = \frac{\partial q n_s}{\partial V_g}.,$$  (2.10)

in which $q$ is the charge of an electron.

Additionally, the surface carrier density $n_s$ is given by the well known integral [121]:

$$n_s = \int_0^\infty DOS.f(E)dE,$$  (2.11)

and DOS is the two dimensional density of states in the QW, and f(E) is the Fermi-Dirac statistics of Eq. 1.30. By inspecting the energy band diagram of Fig. 2.14(b), Eq. 2.11 becomes:

$$n_s = DOS\frac{k_B T}{q}\ln\left[\left(1+exp\left\{\frac{q}{k_B T}[V(d_i^+)-E_0]\right\}\right)\left(1+exp\left\{\frac{q}{k_B T}[V(d_i^+)-E_1]\right\}\right)\right].$$
$$(2.12)$$

Here $E_0$ and $E_1$ are the two lowest energy levels of the QW measured from the bottom of conduction band (Fig. 2.14(b)), and can be found from Eqs. 1.32 and 1.33.

By combining Eqs. 2.9 and 2.10, the differential capacitance is calculated as:

$$C_{diff} = 1/(\frac{\partial V}{\partial q n_s}) = 1/(\frac{d}{\varepsilon}+\frac{1}{q}\frac{\partial V(d_i^+)}{\partial n_s})$$
$$(2.13)$$

Furthermore, Eq. 2.12 gives the relation between $V(d_i^+)$ and $n_s$, hence:

$$\frac{\partial V(d_i^+)}{\partial n_s} = \frac{2}{3n_s}\left\{\frac{3n_s/D+2(E_0+E_1)}{4C/(C+4)}[1+(1+C/A^2)^{-1/2}]-B\right\}$$
$$(2.14)$$

and,

$$A = exp(E_0/V_T)+exp(E_1/V_T) \tag{2.15}$$

$$B = E_0 exp(E_0/V_T)+E_1 exp(E_1/V_T) \tag{2.16}$$

$$C = 4\{exp[(n_s/(DOS)+E_0+E_1)/V_T]-1\} \tag{2.17}$$

Finally:

$$C_{diff} = \frac{\varepsilon}{d+\Delta d}. \tag{2.18}$$

The $C_{diff}$ vs $V_g$ relation is calculated and shown in Fig 2.14(c) [30]. Importantly, $\Delta d$ indicates the effective distance of the center of the 2DES from the $GaAs/AlGaAs$ interface. It essentially takes into account the envelope wave function of electron

inside a triangular QW. By applying a gate voltage, the center of 2DES is moved further away from the interface and the overall capacitance is reduced. Equivalently, the surface carrier concentration is reduced. The simplicity of charge control model is on reduction of the complicated system dynamics into the effective 2DES distance $\Delta d$, which at equilibrium ($V_g = 0$) becomes $\Delta d = 80\mathring{A}$ [31]. In Sec. 2.2.10, the CCM is applied to the MSM-2DES device for evaluation of the equilibrium capacitance.

### 2.2.10   MSM-2DES circuit model

Based on the C-V characteristics of the MSM-2DES, three independent charge control mechanisms are identified. Each of these mechanisms is related to spatially separated ensemble of charge carriers, hence represents different capacitive source.

**Pre-threshold geometric capacitance** $C_{2DES}$ : Electron density profile for MSM-2DES varactor is calculated by solving Poisson equation using Synopsys Sentaurus™simulation package and is shown in Fig. 2.15. Under equilibrium, a thin reservoir of electrons, or 2DES, is present at the GaAs/AlGaAs hetero-interface. Application of an adequately large $V_{bias}$ locally depletes the electrons only underneath the reverse biased contact, cathode, while maintaining the reservoir intact elsewhere in the device. The evolution of the electron densities with bias are shown in Fig. 2.15(d) along the direction of growth under cathode, anode and in the gap. The electron density significantly drops underneath cathode by 12 orders of magnitude while it remains constant in other regions. The depletion mechanism of the electrons is modeled by charge control model used for HEMTs [30, 120]. A charge control mechanism is then identified through a parallel-plate capacitor:

$$C_{2DES} = C_{geo} = \frac{\epsilon_0 \epsilon_{AlGaAs}}{d^*}, \qquad (2.19)$$

which is comprised of the cathode and 2DES beneath it as its plates and separated

by a distance of $d^* = d_{AlGaAs} + \Delta d$, with $d_{AlGaAs}$ being the thickness of AlGaAs layer and $\Delta d = 8nm$ the effective distance of the center of the 2DES to the heterojunction [30, 120], and as previously explained in Sec. 2.2.9.

The validity of the CCM model for calculation of the $C_{2DES}$ of the MSM-2DES capacitor is confirmed by comparing the predictions of the model with the measured capacitance. Through Eq. 2.19, CCM predicts a $C_{2DES}$ of $18.3pF$, which is close to the measured $C_{2DES} = 18.8pF$ at $PF = 10kHz$. Importantly, this value is twice larger than similar planar MSM devices which include a 2DES[29, 77, 81]. While in those devices the pre-threshold equilibrium capacitance is due to the anti-series combination of anode- and cathode- to 2DES parallel plate capacitors, here the $C_{2DES}$ only includes the cathode-to-2DES capacitor. This is due to the preservation of the 2DES in the present MSM-2DES varactor, while in other similar devices [29, 81] it is depleted in other regions. Markedly, CCM is utilized to find the 2DES concentration through the measured $C_{2DES}$. By replacing the experimental data of $C_{2DES} = 18.3pF$ into Eqs. 2.13, 2DES density was graphically solved by MATLAB™and found $N_{ca} = 4.6 \times 10^{11}cm^{-2}$. This is in agreement with Hall density of $6.2 \times 10^{11}cm^{-2}$. This calculation is particularly important for future discussions on many-body features of the 2DES in Chaps. 3 and 4.

**Post-threshold lateral capacitance, or** $C_{lat}$ : Calculated electron density across a horizontal line in the 2DES (line H in Fig. 2.15(c)) indicates a slight penetration of the depletion region in the vicinity of the cathode edge with an increase in $V_{bias}$. Consequently a second capacitance, $C_{lat}$ due to the lateral extension of electric field lines into the gap can be identified with the cathode and the preserved 2DES as its two contacts. The lateral field penetration does not exceed the Thomas-Fermi screening length, $L_{TF}$ for a 2DES [30]. Thus there is a lateral capacitance between the edge of the 2DES and the cathode edge ($C_{lat}$) and a bulk capacitance ($C_{bulk}$)
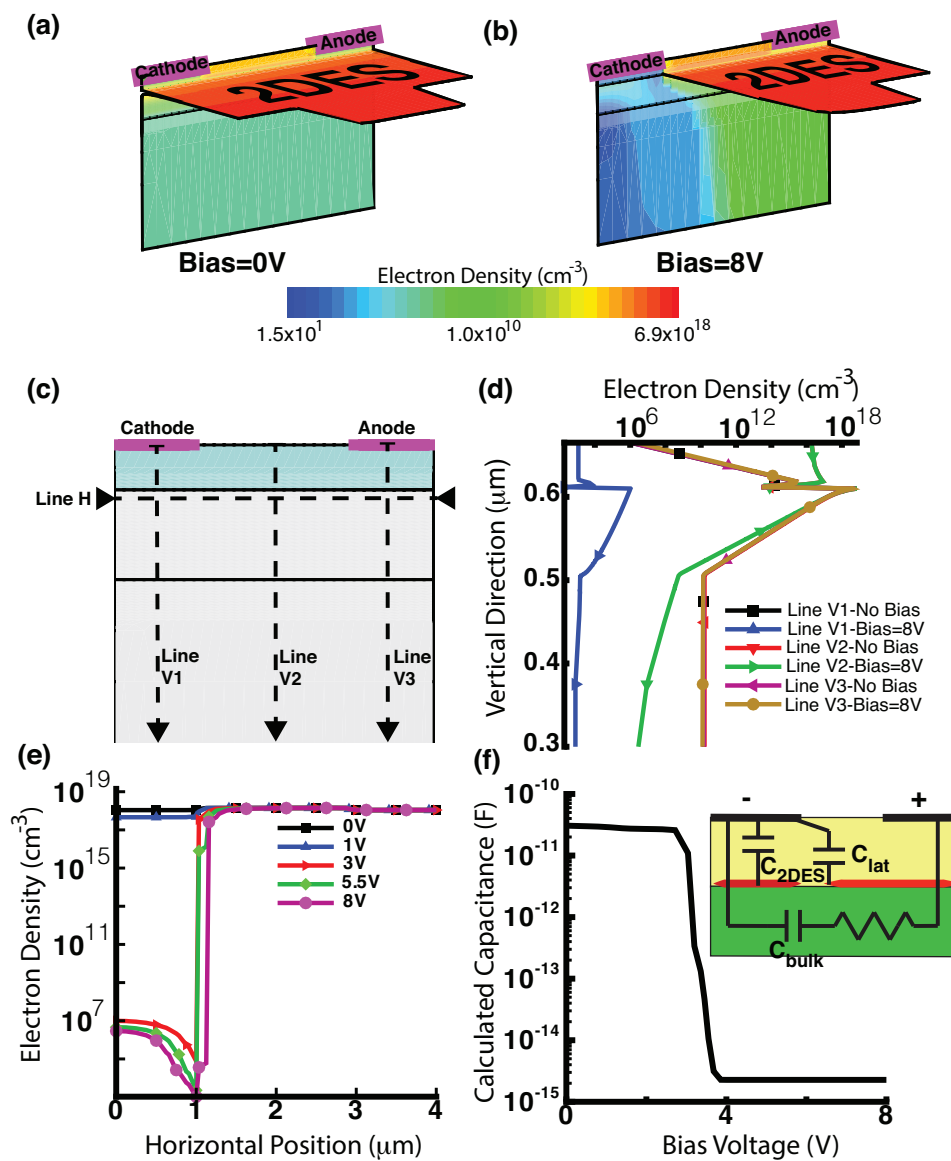
Figure 2.15: a) A three dimensional representation of calculated electron density at equilibrium (left) and under 5V of bias (right), b) Profile of electron density under various bias voltages along the direction of growth, c) Electron density profile along a lateral direction in the device, and d) Calculated capacitance and a qualitative circuit model for the MSM-2DES capacitor.

due to field lines which penetrate deep into the bulk of the device. Using conformal mapping [122], and with $L_{TF} = 6.4nm$ for $N_{ca} = 6.9 \times 10^{11} cm^{-2}$ in the MSM-2DES capacitor, $C_{lat}$, chiefly being a fringe capacitance, is calculated by:

$$C_{lat} = \frac{\epsilon_{AlGaAs}\epsilon_0}{\pi} \sqrt{\frac{L_{TF}d^*}{L_{TF}^2 + d^{*2}}}, \tag{2.20}$$

which yields $C_{lat} = 1.24fF$. The measured $C_{min}$ for all separations are in agreement with measurements (reported in Table 2.2), within the femto-Farad resolution of the LCR meter. Exceptionally, this minimum capacitance is smaller than that of two coplanar contacts, the value of which, found by conformal mapping techniques [104, 123], is $7.7, 6.0, 5.1, 4.3, 3.2fF$ for $3, 5, 7, 10$ and $20\mu m$ contact separations, respectively. Embedment of a high-density 2DES in a layer structure can potentially decrease the capacitance between two adjacent contacts on a substrate. Consequently, the number of devices per unit area of the substrate could increase and higher integration in ICs may be achieved.

**Post-threshold depletion capacitance, or $C_{bulk}$:** Furthermore, a bulk capacitance, $C_{bulk}$, due to the extension of the depletion region in the bulk of the structure, exists, which is mainly inside the $GaAs$ underlying layers. Since $C_{lat}$ and $C_{2DES}$ are in parallel, the former only dominates at $V_{bias} > V_{th}$ when $C_{2DES}$ is zero. Moreover, $C_{lat}$ and $C_{bulk}$ are parallel mechanisms at $V_{bias} > V_{th}$, and an increase in the contact separation, results in more dominant $C_{bulk}$, leading into deviations from the expected $C_{lat}$ capacitance. Moreover, comparison of post-threshold C-V of MSM-2DES capacitor with that of the control devices (Fig. 2.10), highlights the role of $C_{bulk}$ as a third parallel capacitance, which accounts for the junction capacitance of the cathode Schottky contact. For the MSM-2DES capacitor, as displayed in Fig. 2.3, the screening of electric field by 2DES limits the horizontal extension of depletion region, hence a $C_{bulk}$ becomes noticeably smaller than that of the CMSMs and control de-

vices. In similar bias voltage and probe frequencies, the control sample maintains a post-threshold capacitance of larger than $200fF$ while the MSM-2DES capacitor reaches $C_{min} < 10fF$ and remains less than $150fF$ with a further increase in bias. In a like manner, for the CMSMs with similar contact geometry and measurement conditions, the capacitance never goes below $10fF$ (see Fig. 1.3 and Sec. 1.5.1), which is greater than the $C_{min}$ for the MSM-2DES capacitor.

Fig. 2.15(f) represents simulated C-V which is in a good qualitative agreement with experimental results, both in general behavior and in the value of threshold voltage. It does not, however, include CE and NC features since these are attributed to quantum mechanical exchange-correlation effects in 2DES [26], which are beyond the capabilities of the simulation package. A qualitative circuit model that includes the three identified capacitive mechanisms for the MSM-2D varactor is indicated in the inset of Fig. 2.15(f).

Finally, a prominent feature of this device is the capacitance enhancement in C-V which occurs when the 2DES transitions from a high density interacting system to a depleted non-interacting one. This is due to negative thermodynamic density of states for a 2DES [23, 25], and will be describe in Chap. 3. This has been also proposed as a gate capacitance enhancer for MOSFETs [26]. Here, the addition of exchange and correlation energies of the interacting many-body system of 2DES, as the unconventional contact, to the stored energy inside the electric field of the dielectric, results in an enhancement in the overall capacitance, as an energy storage device [23]. Enhancement of $C_{max}$ by up to 26%, further increases the tuning ratio. More in-depth discussion on this matter, however, is deferred to Chaps. 3 and 4.

### 2.2.10.1 Experimental verification of electric field screening

An observation was made on the C-V characteristics of the devices that were fabricated on the MSM-2DES wafer, in which the pre-threshold capacitance $C_{2DES}$ was independent of the distance between any two nonisolated contact pads. This is an outstanding consequence of the shielding/screening effect due to the 2DES and the n-type delta doping and has potential application (see Sec. 2.3.3) for cross-talk reduction and signal delivery enhancements in integrated circuits [124]. A systematic experiment was performed, as shown in Fig. 2.16, to verify this observation. Here the subject matter capacitors were "small" planar devices in the TLM layout of Fig. 2.1(d) that were comprised of contact 1 and anyone of the remaining pads as the capacitor terminals. Interestingly, the pre-threshold capacitances, $C_{2DES}$, of all of these devices coincide, as shown in Fig. 2.16, and equals the geometrical capacitance, $C_{geo}$ of Eq. 2.19. This indicates the continuity of the 2DES in the layer structure and verifies the predicted shielding effect of the 2D cloud of charge.
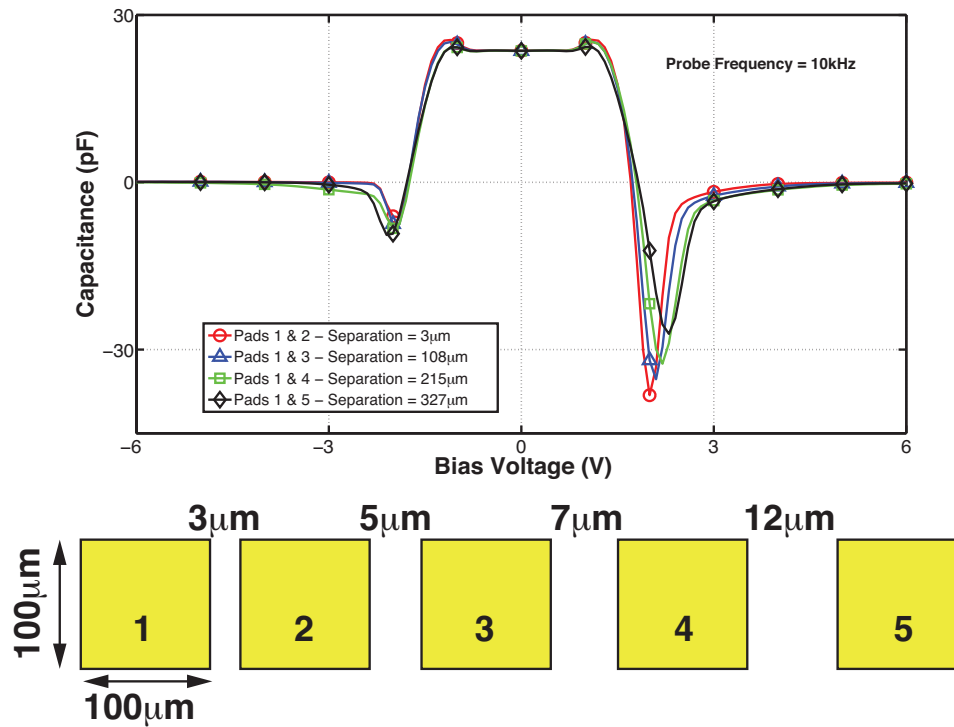
Figure 2.16: C-V characteristics indicates minimum dependence of Capacitance on contact separation.

### 2.2.10.2  Effect of contact pad size on C-V characteristics

Additionally, the C-V of "large" MSM-2DES capacitor follows the general behavior of the "small" analogue, as demonstrated in Fig. 2.17 however, $C_{2DES}$ of the former scales up to 41.2 and $39.9pF$, a factor of 2.2 larger than the 18.73 and $17.83pF$ of the original size MSM-2D varactors with 10 and $20\mu m$ contact separations, respectively. This matches well with the large-to-small contact pad area ratio of 2.25. This indicates that the pre-threshold capacitance merely depends on cathode capacitance. Hence, the electric field shielding of the dense 2DES is verified. For devices that such a dense 2DES does not exist, the $C_{2DES}$ corresponds to an anti-series combination of anode- and cathode-to-2DES parallel plate capacitors, as predicted by Marso et al. [29, 81]. Further details on the latter are discussed in Sec. 2.4.
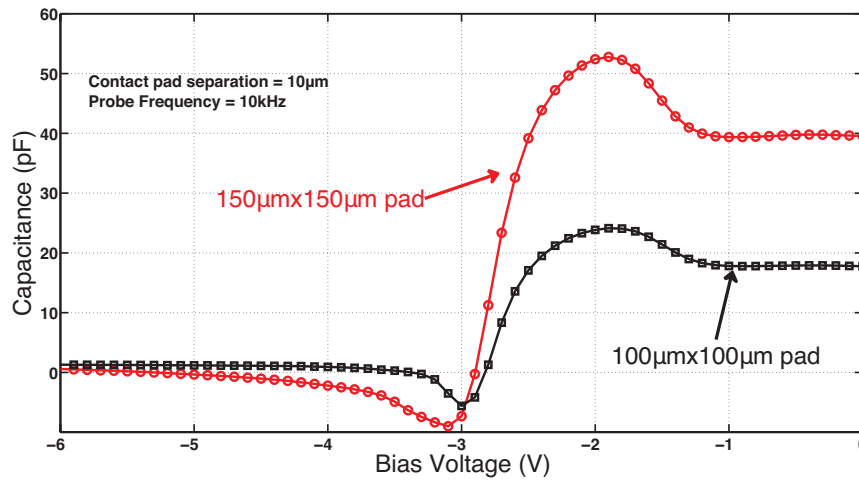
Figure 2.17: C-V characteristics for MSM-2DES capacitor for different areas of the contact pads

## 2.3 Application of the MSM-2DES device as a highly tunable variable capacitor

Voltage-dependent capacitors, or varactors, have a range of applications in frequency multipliers, voltage-controlled oscillators, tunable filters and electro-optical modulators [71, 76]. Important figures of merit are sensitivity defined as (normalized) change of capacitance per change in voltage, tuning ratio (TR) of maximum to minimum of the voltage-controlled capacitance, and quality factor, Q, with a trade-off expected between Q and TR [76]. Typical varactors including those based on MOS technology [82], metal-semiconductor-metals (MSMs) [29, 81] and ones which are carbon-based [125] show TRs less than 40, with maximum TRs of up to 121 that have been achieved using Two Dimensional Electron Gas (2DEG) [29]. Varactors that are based on a two dimensional hole gas can reach high sensitivities of 35, and large TRs of $\sim$ 113 [77]. By judicious use of the 2DES underneath and in-between contacts of the MSM-2DES device can be applied as a remarkable varactor with an

ultra high tuning ratios of well over 1000. It is a result of a large maximum capacitance, and a minimum capacitance that is lower than the geometric capacitance of the coplanar contacts, reaching fF ranges. Table 2.2 summarizes measurement results on MSM-2DES varactors, including zero-bias, minimum and maximum capacitance values, tuning ratio, quality factor, sensitivity, and capacitance enhancement, for various contact separations of "large" contact pads and at different probe frequencies.

Table 2.2: Summary of the measurements on MSM-2DES varactors.

| Separation | $3\mu m$ | | $5\mu m$ | | $7\mu m$ | | $10\mu m$ | | $20\mu m$ | |
|---|---|---|---|---|---|---|---|---|---|---|
| Probe Frequency | 10kHz | 50kHz | 10kHz | 75kHz | 10kHz | 75kHz | 10kHz | 50kHz | 10kHz | 50kHz |
| $C_{0V}(pF)$ | 19.01 | 18.24 | 18.88 | 18.18 | 18.87 | 18.12 | 18.76 | 17.83 | 18.73 | 17.33 |
| $C_{min}(fF)$ | 150 | 2.6 | 207 | 3.7 | 43 | 3.2 | 83 | 8 | 108 | 9 |
| $C_{CE}, C_{max}(pF)$ | 24.24 | 22.08 | 24.25 | 22.22 | 24.94 | 21.27 | 24.12 | 21.88 | 24.02 | 21.98 |
| Tuning Ratio $(\frac{C_{max}}{C_{min}})$ | 127 | 7015 | 91 | 4913 | 438 | 5662 | 226 | 2228 | 173 | 1925 |
| Max. Q | 40.94 | 16.73 | 41.15 | 17.10 | 40.84 | 16.58 | 41.32 | 16.87 | 40.64 | 17.43 |
| Sensitivity | 163 | 370 | 65 | 263 | 173 | 187 | 118 | 98 | 80 | 246 |
| Enhancement $(\frac{C_{CE}-C_{0V}}{C_{0V}})$ | 27.5% | 21.0% | 28.4% | 22.22% | 32.16% | 17.38% | 28.5% | 22.7% | 28.2% | 26.8% |

### 2.3.1 Performance merits of the MSM-2DES varactor

Figures of merit for a varactor include:

**Tuning Ratio/Range (TR)** indicates the range that the capacitance can be varied in the capacitance-voltage characteristics (C-V) of a varactor. It is defined as:

$$TR = \frac{C_{max}}{C_{min}}, \tag{2.21}$$

where $C_{max}$ and $C_{min}$ are the maximum and minimum attainable capacitances in C-V, respectively.

The tuning ratio for the MSM-2D varactors, shown in Table 2.2, surpasses 7,000 at $PF = 75kHz$ and remains above 100 for the rest of PFs, which, to the best of our knowledge, is higher than other reports. This is primarily due to the significantly small $C_{min}$ of MSM-2DES varactors, being in fF range-3fF for $7\mu m$ separation at $75kHz$ of PF. Distinctively, the CE feature, which is attributed to negative compressibility of 2DEG [23, 24, 26], further increases the TR as the peak capacitance, $C_{CE}$, of up to $24.94pF$ occurs at the peak of the "Batman" shape of CE, resulting in enhancements.

**Quality Factor, Q:** is a measure of the stored to dissipated energy, with an expected trade-off between Q and TR [76]. The MSM-2DES varactors reach maximum Q of up to 40, as indicated in Fig. 2.18 and Table 2.2, which is comparable to other reports [76].
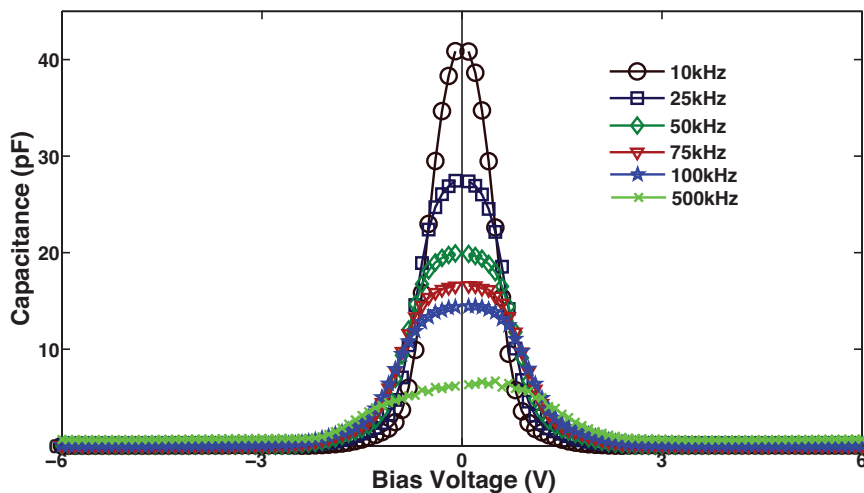


Figure 2.18: Quality factor vs. voltage for MSM-2DES varactor at various probe frequencies.

**Voltage Sensitivity (S):** is quantitatively defined by:

$$S = \frac{dC}{dV} \times \frac{V}{C} \tag{2.22}$$

Sensitivity indicates the normalized rate of change in the capacitance with respect to the applied voltage [35, 77], showing how abrupt in voltage the capacitance can vary within the tuning range. Importantly, sensitivity S demonstrates the level of nonlinearity in C-V, required for frequency multiplication applications. MSM-2DES varactors exhibit sensitivities of up to 370 at intermediate PFs, exceeding previous achievements [35, 77, 81].

### 2.3.2 MSM-2DES varactor as an integrated switched-capacitor

This large voltage sensitivity, combined with the bi-state behavior of pre-threshold "high" and post-threshold "low" capacitances, indicates the capability of MSM-2DES varactor to be utilized as a switchable capacitor, which are useful circuit elements in filters, modulators and rectifiers [126, 127], while it circumvents the need for additional switching elements.

### 2.3.3 MSM-2DES varactor for RFICs

Continuous down-scaling of integrated circuits (ICs) and closer placement of circuit elements and signal lines (SL) on chips have brought in new challenges to overcome the noise due to increased capacitive coupling and cross-talk among SLs [124]. Prediction of the performance of the ICs often require complicated models to account for delay and clock skew variations due to coupling capacitance [128].

The pre-threshold $C_{2DES}$ of the MSM-2DES varacor, being twice larger than previous predictions [29, 81, 112], indicates higher energy densities in the region underneath the cathode. Hence a better coupling between the cathode, serving as signal

carrier, and the reference plane (2DES), can be achieved and utilized in ICs to increase the signal-to-noise ratio. Additionally, the 2DES in the gap that extends to the anode, and is maintained at post-threshold "low" state, shields the electric field lines from lateral extension into the gap resulting in a minimal $C_{min}$. The value of this capacitance is calculated, similar to fringe capacitance in coplanar waveguides [122], to be $1.8fF$, which closely matches experimental results of 3fF. That is, maintaining a sufficient density of the 2DES under anode and between contacts allows the minimum capacitance to be much lower than the geometric capacitance of the coplanar cathode-anode structure [123, 186]. The latter is calculated to be $8.82, 6.06$, and $4.84fF$ for 10, 20, and 40 $\mu m$ separations, respectively, meaning that the embedded 2DES reduces the capacitance by a factor ranging from 2.7 to 4.9 for these structures. The decrease in inter-contact capacitance is suitable for reduction of cross-talk among SLs in ICs, and for removing the noise due to coupling of interconnects in VLSIs.

Negative capacitance is a feature with applications in voltage amplification [129], solar cells [130], and to overcome the 'Boltzmann tyranny' [131]. It has been observed in electrochemical capacitors [132], far-infrared [133], heterojunction dual-band [134] detectors, GaN Schottky diodes [182], and in ferroelectric materials [135]. Previous reports on the observation of negative capacitance in semiconductor devices [133, 136] attribute this phenomenon to transient currents in the device, recharging inertia of the QW [133] and, in general, dc/ac signal mixing across a nonlinear conductor [136, 182], all of which are feasible in the MSM-2D varactor. From the circuit level, a negative capacitance is viewed the same as an inductor. Currently, realization of inductors in RFICs is through placement of bulky elements on the chip affects both the performance and the cost of these circuits [137, 138]. The negative capacitance feature of MSM-2DES varactor can serve as a low cost and less bulky replacement for fabrication of inductors in microwave-photonics applications. Overall, an enhanced

performance for RFICs and a better cost efficiency are attainable through a) closer arrangement of the components on the chip and b) replacement of bulky elements, that are available through distinct features of the MSM-2DES varactor.

### 2.3.3.1   Scattering matrix measurement on MSM-2DES capacitor

The reflection coefficient, $S_{11}$, was measured using a vector network analyzer. Fig. 2.19(a) shows magnitude of $S_{11}$ for different applied voltages. Two resonant peaks near 1 and $1.8GHz$ are observed the magnitude of which is strongly dependent on applied voltage. Fig. 2.19(b) compares dark and white-microscope light responses with the same applied voltage, showing more than $20dB$ change due to illumination. These measurements were repeated with a laser light source, which confirmed device sensitivity to optical signal. The device sensitivity to voltage and light makes it an excellent candidate for microwave photonics applications like electro-optical modulations and frequency doublers.

## 2.4   Structural modifications for local manipulation of 2DES density

A layer of SiN, which is grown in the region between the contacts and on top of the AlGaAs layer introduces surface states and increases surface velocity at the SiN/AlGaAs interface. As a result, some portion of the 2DES in the "gap" region is depleted, while underneath the contacts it is maintained. This effect can be seen in the measured C-V characteristics for the MSM-2DES with SiN top layer, that is also shown in Fig. 2.20. The equilibrium capacitance is measured for a $100 \times 100\mu^2$ TLM device with $5\mu$ contact separation. It takes a $8.2pF$ value at a $2kHz$ probe frequency and drops to $1.9pF$ for probe frequencies greater than $500kHz$, which is significantly less than those reported for MSM-2DES capacitor. The quality factor for this SiN MSM-2DES capacitor remains less than 10 for all the measured probe frequencies.
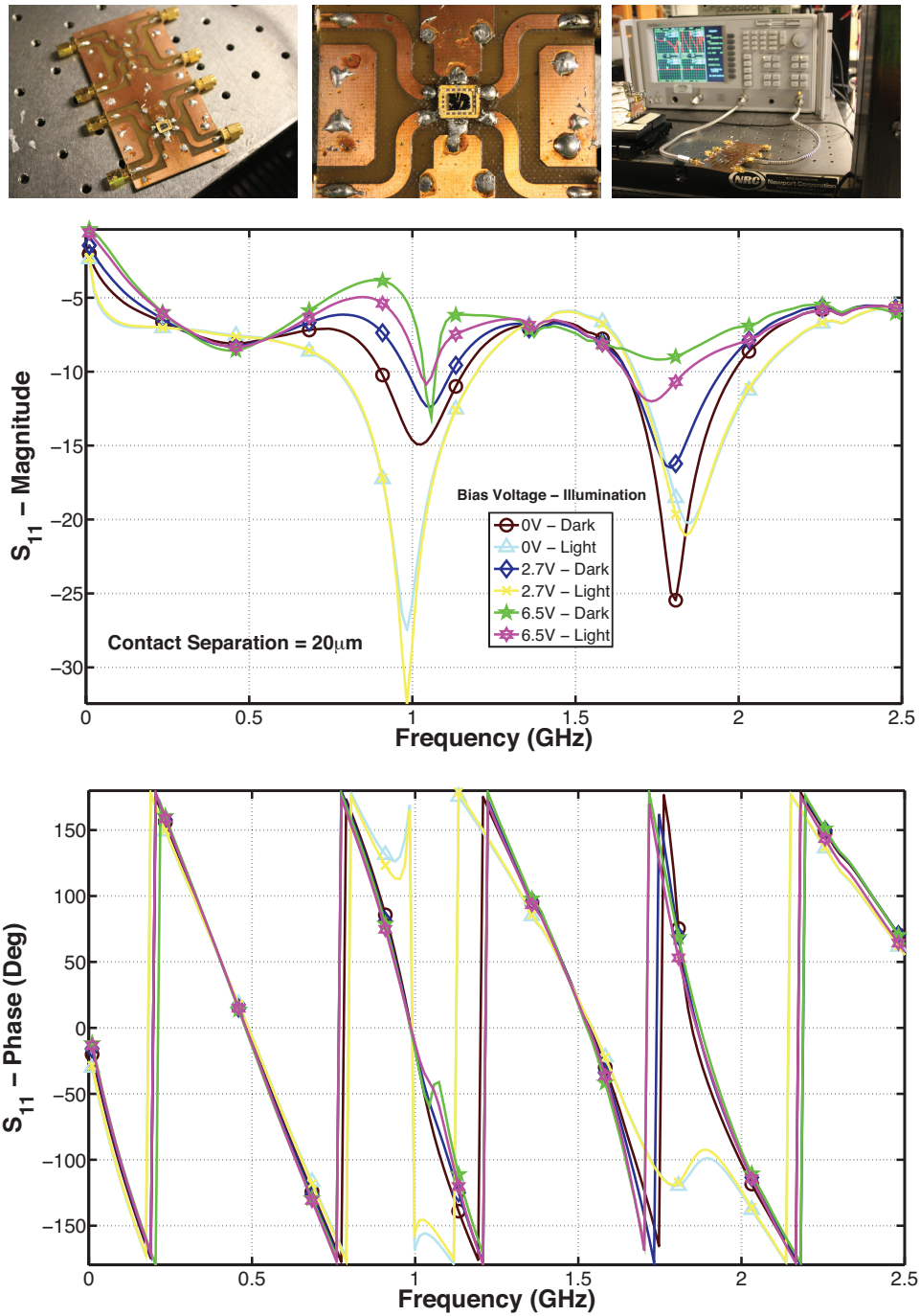
Figure 2.19: a) Magnitude, and b) phase of the $S_{11}$ parameter for MSM-2DES capacitor with a $20\mu m$ contact separation, measured under various bias and illumination conditions.
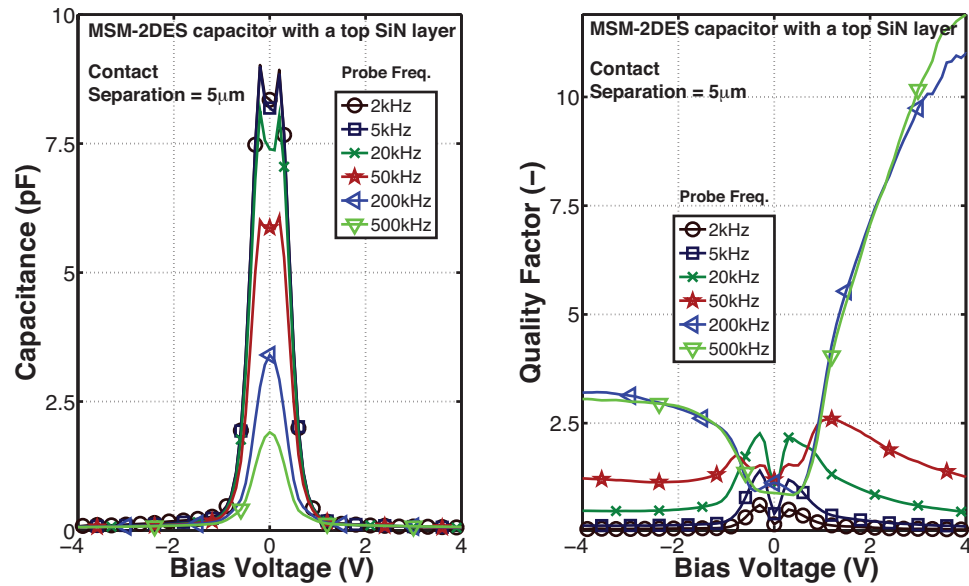
Figure 2.20: C-V characteristics for an MSM system with SiN in the "gap".

When the 2DES in the "gap" region between contacts is partially depleted, it can not screen the electric field any more. In this case, $C_{lat}||C_{dep}$ becomes significant, and the overall capacitive behavior follows the model proposed by Marso et al [29, 81, 110, 111, 112]. The pre-threshold capacitance then becomes an anti-series combination of anode- and cathode-to-2DES parallel plate capacitors.

Importantly, the C-V for the SiN MSM-2DES capacitor does not include a CE feature, which infers a relation between the CE and the 2DES density. This will be tested in further detail in Chap. 4.

## 2.5   A high-speed interdigitated MSM photodetector with a low-temperature grown GaAs layer

For MSM photodetectors, a limiting factor in the speed of operation is the carrier life-time, as also discussed in Sec. 1.5. The device speed performance can be enhanced if the life time of the photo-generated carriers in the absorption medium is reduced.

Low-temperature grown GaAs (LT-GaAs) is a good candidate for this purpose with a $\sim 1ps$ carrier life-time. This value is three orders of magnitude shorter than that of regular GaAs ($\sim 1ns$). The LT-GaAs MSM photodetectors, however, suffer from low light sensitivity, due to low carrier mobility. This problem can be addressed through using the LT-GaAs as the absorption medium of a MSM device with a *vertical electric field* similar to that of MSM-2DES varactor.

The MBE growth was performed on a semi-insulating (100) GaAs substrate, starting with a buffer layer, followed by a $500nm$ thick layer of unintentionally doped GaAs and a p-type (C-dopant) delta doping layer. An $85nm$ LT-GaAs active layer was then grown at $300°C$, followed by a $15nm$ undoped GaAs layer grown at the regular growth temperature of $600°C$, producing a channel with high mobility and long lifetime, hence momentum relaxation distance, for carrier transport. Growth of a $50nm$ AlGaAs layer formed a heterojunction with this RT-GaAs channel. Fig. 2.21 compares the current-voltage characteristics of MSM-2DES, control and LT-GaAs MSM devices. The measurements are performed for interdigitated contact patterns with and without transmission lines, and for dark and under red LED illumination. While the MSM-2DES device has an unusually large dark current ($\sim 10\mu A$), the control and the LT-GaAs MSMs have similar dark currents that remain in the $pA$ range, hence are ideal for low-noise photodetection purposes. Furthermore, the addition of the transmission lines to the typical interdigitated pattern does not change the current values, both in dark and under light, by an appreciable amount. This indicates that no significant leakage current from the lines is affecting the device performance.

Fig. 2.22 indicates the calculated electric field in this LT-GaAs MSM, at equilibrium (2.22(a)) and under $9V$ of applied bias(2.22(b)), and for contact spacings of 1 (top) 3 (middle) and $5\mu m$ (bottom). A vertical electric field exists in all of these
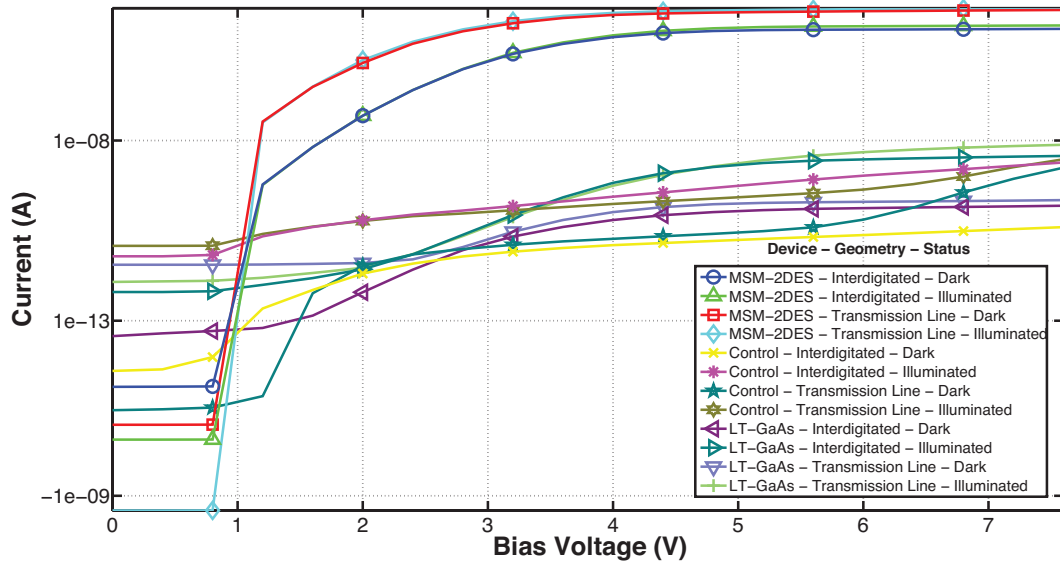
Figure 2.21: Comparison of I-V characteristics for MSM-2DES, control, and LT-GaAs MSM devices.

condition that drifts the photo generated carriers in the LT-GaAs absorption region to the channel of regular GaAs. Under applied bias, a large electric field exists underneath the cathode that collects the photo generated carriers that have reached the $15nm$ high-mobility channel of RT-GaAs. This condition can be seen in the calculated energy band diagram under a $9V$ bias and indicated in Fig. 2.23, for all the contact spacings. A band bending in the LT-GaAs absorption region favorably drifts the light generated electrons toward the RT-GaAs channel. With the high electron mobility of GaAs, the photo generated carriers quickly reach the region underneath the cathode with an electric field with minimal horizontal component. A very large band bending at the edge and underneath the cathode collects the carriers across the AlGaAs top layer.
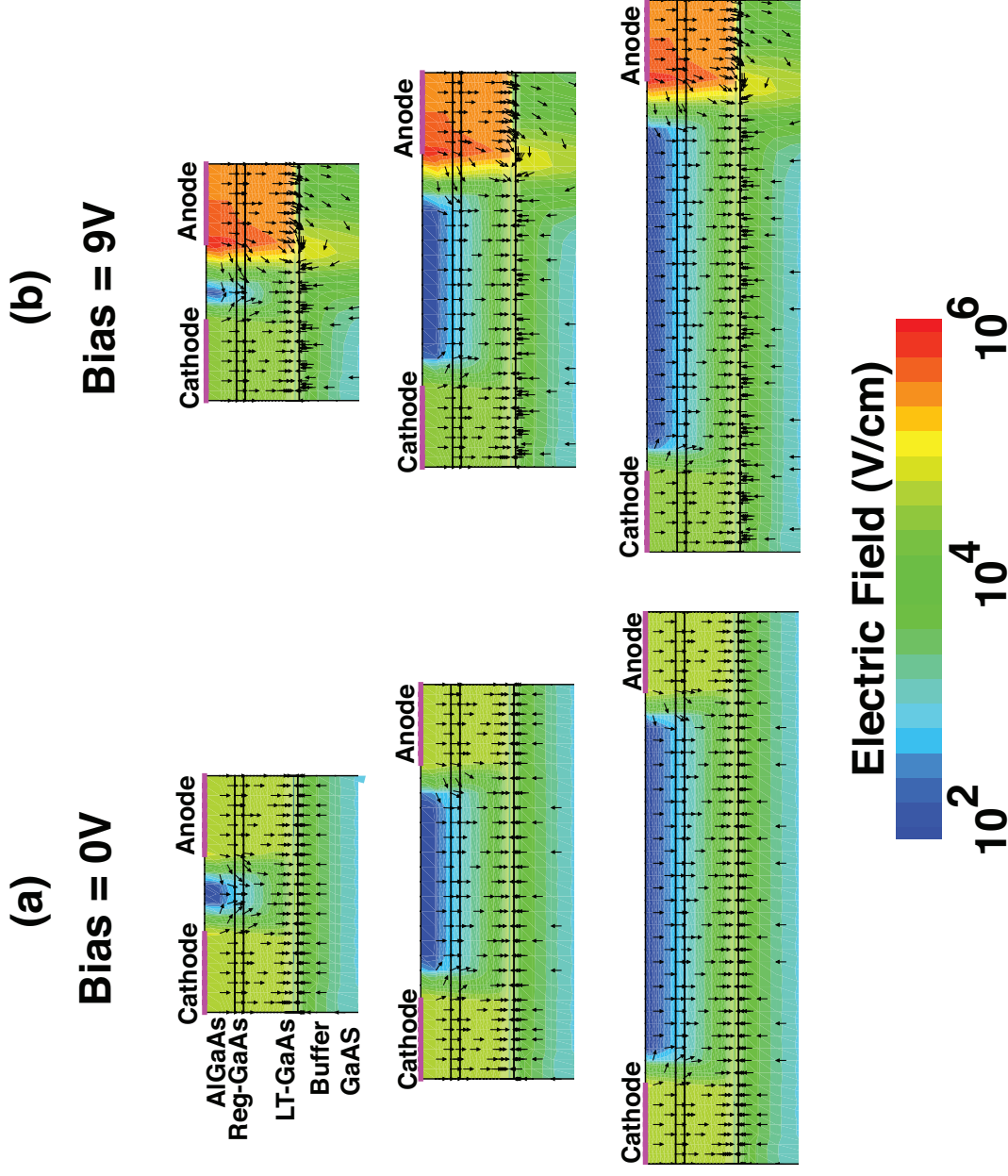
Figure 2.22: Calculated electric field inside the the LT-GaAs MSM device at a) equilibrium and b) under 9V bias for contact separations of 1µm, (top) b) 3µm, (middle) and c) 5µm (bottom).
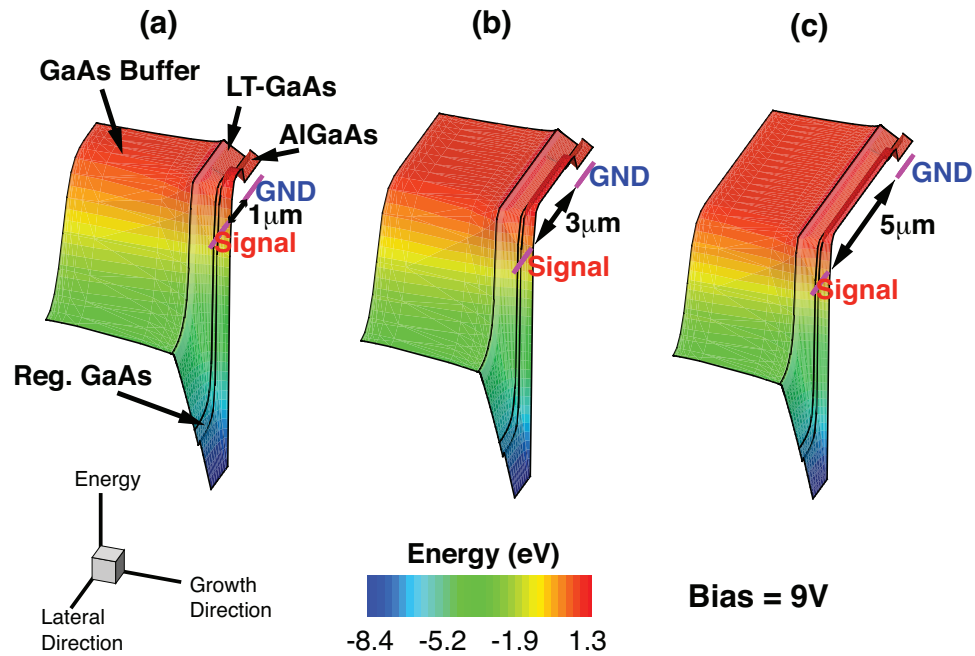
Figure 2.23: Calculated conduction band energy for the LT-GaAs MSM device for contact separation of a) $1\mu m$, b) $3\mu m$, and c) $5\mu m$.

The electro-optic sampling technique with picosecond resolution [139] was used to measure the time response of LT-GaAs MSM devices with an interdigitated structure with a layer structure and finger spacings similar to that of Fig. 2.22 [94]. These devices have detection efficiency near that of RT-GaAs yet provide pulse widths nearly an order of magnitude faster-6$ps$ for a contact separation of $1\mu m$ and 12$ps$ for distances more than $3\mu m$.

Through further inspection on the C-V characteristics of the LT-GaAs MSM, formation of a high-mobility channel under illumination and in the RT-GaAs layer of the device can be verified. Figs. 2.24(a) and (b) indicate the C-V in dark and under light for a LT-GaAs MSM with a TLM contact pattern of $20\mu m$ spacing. The lack of the bi-state of "high" and "low" in dark C-V shows that no 2D electron channel exists at the GaAs/AlGaAs interface. The C-V under red LED, however, exhibits a peak

at electrical equilibrium that gradually reduces to that of dark capacitance at higher bias values. Consequently, similar to the MSM-2DES varactor of previous sections, a sheets of charge is formed at the interface under illumination. Frequency dependence of this light-dependent behavior is shown in Figs. 2.24(b) and (c), for capacitance and quality factor respectively. They follow the trend as that of the MSM-2DES device.
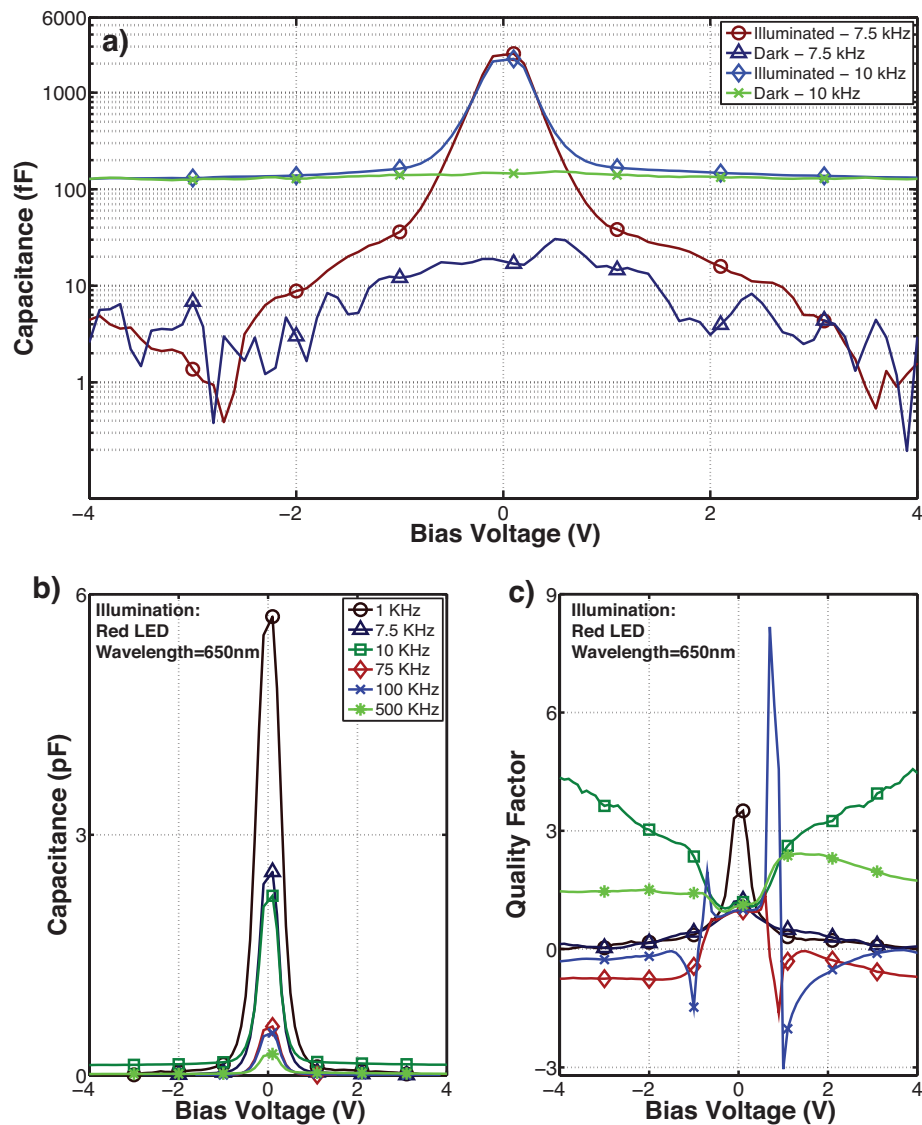


Figure 2.24: C-V characteristics for the LT-GaAs MSM device: a) at dark and under microscope illumination, b) under red LED light; c) Q-V characteristics under red LED light.

## 3. A Many-Body System of Electrons

### 3.1  Basic concepts

In chapter 2, the one electron approach to the Schrödinger equation was applied to many practical applications. It was seen to be adequate for prediction of transport properties of many solid-state devices so long as the device scale was not in the order of an electron de Broglie wavelength. The one electron problem, however, is not valid when an electronic system becomes correlated. That is when the inter-electron distance becomes small enough that the Coulombic interactions among electrons cannot be ignored. In such situations, it is necessary to include the potential energy term, which is due to the Coulombic forces among electrons, in the Hamiltonian of the system. Furthermore, as the electrons follow Fermi-Dirac statistics, they have to satisfy the Pauli's exclusion principle, which imposes an additional constraint on the wave function of the many-body system. In this section, the mathematical formalism of the many-body problem is presented. Various approaches toward this problem are explained, and the ground state energy of such many-body systems is described.

#### 3.1.1  Basic properties of many-electron systems

##### 3.1.1.1  Permutation symmetry: indistinguishable vs. distinguishable electrons

The many-body wave function, as in Eq. 3.1 represents a problem with distinguishable fermions. That is, if two of the fermions are exchanged, the state of the system is changed, or:

$$\Psi(1...i...j...N) \neq \Psi(1...j...i...N) \tag{3.1}$$

This, however, is not permissible in quantum mechanics, since the state of the system has to be independent of the exchange of the fermions and the overall state (wave function) of the many-body system is required to remain intact. Equivalently, the fermions are required to be indistinguishable. Unlike classical mechanics, individual particles cannot be labeled and distinguished. This condition can be satisfied by reconstructing the many-fermion wave function in a way that it satisfies the anti-symmetry requirement:

$$\Psi(1...i...j...N) = -\Psi(1...j...i...N). \tag{3.2}$$

One way of accomplishing this condition is by constructing $\Psi$ based on a sum series of complete set of orthonormal one-fermion problem states, as:

$$\Psi(1, 2, ..., N) = \frac{1}{N!} \sum_p sgn(p) \prod_{i=1}^{N} \psi_p(i). \tag{3.3}$$

### 3.1.1.2 Pauli's exclusion principle

The Pauli's exclusion principle is a condition that any solution to a many-electron problem has to satisfy: the wave function has to be invariant to exchange of any two particles. For a system of $N$ fermions, the simplest guess for the many-body wave function, $\Psi(1, 2, ..., N)$ is a product of one fermion wave functions at the allowable energy states; i.e.:

$$\Psi(1, 2, ..., N) = \prod_{i=1}^{N} \psi_i(i). \tag{3.4}$$

### 3.1.1.3 Basis states: Slatter determinent

Equation 3.3 can be rewritten as a determinant of a matrix with one-electron wave functions as its elements; known as the Slater determinant:

$$\Psi(1, 2, ..., N) = \begin{vmatrix} \psi_1(r_1) & \psi_2(r_1) & \ldots & \psi_N(r_1) \\ \psi_1(r_2) & \psi_2(r_2) & \ldots & \psi_N(r_2) \\ \vdots & \vdots & \ddots & \vdots \\ \psi_1(r_N) & \psi_2(r_N) & \ldots & \psi_N(r_N) \end{vmatrix} \tag{3.5}$$

Inspecting the Slater determinant in Eq. 3.5 indicates that if two electrons have the same quantum state, hence identical wave functions, the determinant becomes zero. Equivalently, such an event will have a zero likelihood. Consequently, for any physical system no two electrons can exist at the same quantum state. Noticeably, it is inferred from the above discussions that a "force" prevents indistinguishable fermions from co-existence at the same quantum state. This is known as the exchange force, that results in the inclusion of an additional energy term in the ground state energy of the many-body system, as will be discussed in Sec. 3.3.

While using the Slater determinant as the solution of the many-body Schrödinger equation addresses the indistinguishability requirement, the statement of the problem through this perspective is still deficient. Mainly, the notion of exchanging two separate fermions infers certain level of particle discretion, which is in contradiction with the indistinguishability of fermions in a quantum system. Hence, it is required to establish a complete quantum mechanical approach toward the many-fermion problem. This is accomplished by the second quantization method, which is described in the following sections.

### 3.1.2 An alternative approach: Second quantization

The concept of second quantization inherently satisfies the indistinguishability of fermions. Hence, the relevant quantity for this approach is the number of fermions, $n_i$ that occupy a certain eigenstate $i$ with an eigenenergy of $E_i$. It requires a basis set of complete orthonormal state vectors, on which other operators in the Hilbert space can be expanded. The time-independent occupation *number state* vector, $|n_i\rangle$, sufficiently represents the number of fermions that occupy the single-particle eigenstate $i$.

As a direct consequence of the Pauli's exclusion principle, the occupation number, $n_i = 0, 1$, since no more than one fermion can occupy a state. The creation, $c^\dagger$, and annihilation, $c$, operators of the number states, change the eigenvalue of the number operator, as:

$$c^\dagger |0\rangle = |1\rangle \,, c^\dagger |1\rangle = |0\rangle \,, \tag{3.6}$$

$$c |1\rangle = |0\rangle \,, c |0\rangle = |0\rangle \,. \tag{3.7}$$

These operators follow the rules of *anticommutation,* that is:

$$\{c_r, c_s^\dagger\} = c_r c_s^\dagger + c_s^\dagger c_r = \delta_{rs}, \tag{3.8}$$

$$\{c_r, c_s\} = \{c_r^\dagger, c_s^\dagger\} = 0. \tag{3.9}$$

The number operator, $\hat{n}_s$ for the mode $s$, can then be defined as:

$$\hat{n}_s = c_s^\dagger c_s, \tag{3.10}$$

$$n_s = \hat{n}_s |n_s\rangle = c_s^\dagger c_s |n_s\rangle \,. \tag{3.11}$$

It is now essential to define the many-body number state vector as $|n_1 n_2 ... n_\infty\rangle$ for a system of $N$ total electrons with $N = n_1 + n_2 + ... + n_\infty = \sum_i n_i$, and investigate

the effect of creation and annihilation operators on the many-particle wave function $\Psi$. Notably, the total number of carriers $N$ is a constant, which means the $c$ and $c^\dagger$ operators do not change the total number of electrons in the system. Since the occupation number state is a complete orthonormal set in the Hilbert space, it is logical to expand $\Psi$ based on this set:

$$|\Psi(t)\rangle = \sum_{n_1 n_2 ... n_\infty} f(n_1 n_2 ... n_\infty, t) |n_1 n_2 ... n_\infty\rangle \tag{3.12}$$

It can be shown that Eq. 3.12 is a solution to the Schrödinger equation, with the Hamiltonian $\hat{H}$ restated through creation and annihilation operators:

$$i\hbar \frac{\partial}{\partial t} |\Psi(t)\rangle = \hat{H} |\Psi(t)\rangle , \tag{3.13}$$

$$\hat{H} = \sum_{rs} c_r^\dagger \langle r| T |s\rangle c_s + \frac{1}{2} \sum_{rstu} c_r^\dagger c_s^\dagger \langle rs| V |tu\rangle c_u c_t, \tag{3.14}$$

in which T and V are the kinetic and potential energy operators, respectively. Eq. 3.14 generalizes the many electron problem to a number state with simplified operators of creation and annihilation. Conveniently, field operators can be defined based on $c$ and $c^\dagger$:

$$\hat{\psi}(x) = \sum_k \psi_k(x) c_k, \tag{3.15}$$

$$\hat{\psi}^\dagger(x) = \sum_k \psi_k(x) c_k^\dagger. \tag{3.16}$$

Field operators that are described in Eq. 3.16 are linear expansion of annihilation and creation operators, with the coefficients as the single-particle wave functions, $\psi_k(x)$. In general, any one-body operator, $J = \sum_{i=1}^{N} J(x_i)$ has a corresponding

second-quantized operator that is given by:

$$\hat{J} = \sum_{rs} \langle r| J |s \rangle c_r^\dagger c_s = \int d^3x \hat{\psi}^\dagger(x) J(x) \hat{\psi}(x). \qquad (3.17)$$

This constitutes the major distinction from the first quantization, in which the physical measurable quantities such as momentum and position are replaced with their corresponding quantum operators. In the second quantization formalism, the field variables such as wave functions are quantized into field operators, that are restated through the *creation* and *annihilation* operators. The essence of the second quantization method is that once the ground state of a system is found as a solution of the Schrödinger equation, all the excited states of the system can then be calculated by applying the creation and annihilation operators. Hence the ground state energy, $E_{gse}$, becomes a physically significant property of a given system. By knowing this quantity, the energies for all other excited states can be found through second quantization.

## 3.2 Correlated many electron systems

Defining the proper many-electron system (MES) Hamiltonian, $H_{mse}$,is the initial step in solving a given many-body problem. Particularly, for the case of a many electron system, it has to account for the Coulombic interactions among particles.

### 3.2.1 A degenerate electron gas

A degenerate electron gas is a system of interacting electrons, with density of $n_e(r)$, accompanied by a positive ion background, with density of $n_p(r)$, which provides the charge neutrality. This system is specifically selected to exclude the effect of the thermal energy on distribution of electrons in the available energy states; hence in

a degenerate electron gas all the states are occupied progressively, starting from the lowest energy level and according to Pauli's exclusion principle. A major assumption for this case is the homogeneity in the spatial distribution of the positive background, which along with the neutrality of this system requires that $n_e(r) = n_p(r) = n_0$. The dynamical behavior of the positive ions can practically be ignored due to their much heavier mass compared to the electrons. The Hamiltonian accounts for the repulsive force among the electrons, $H_{el}$, and the attractive force between the electrons and the positive background ions aka *Hartree interaction*, $H_{el-b}$, and the energy of the positive background, $H_b$. Hence:

$$H_{mse} = H_{el} + H_b + H_{el-b}. \tag{3.18}$$

The Hamiltonian terms can be expanded with respect to the specifics of the degenerate electron gas, with a *uniform* positive background with density $n(x)$.

$$H_{el} = \sum_{i=1}^{N} \frac{p_i^2}{2m} + \frac{1}{2}e^2 \sum_{i \neq j}^{N} \frac{e^{-\eta|r_i - r_j|}}{|r_i - r_j|}, \tag{3.19}$$

$$H_b = \frac{1}{2}e^2 \int \int d^3x d^3x' \frac{n(x)n(x')e^{-\eta|x - x'|}}{|x - x'|}, \tag{3.20}$$

$$H_{el-b} = -e^2 \sum_{i=1}^{N} \int d^3x \frac{n(x)e^{-\eta|x - r_i|}}{|x - r_i|}. \tag{3.21}$$

In Eqs. 3.19, 3.20, and 3.21 an exponential convergence factor is inserted to define the integrals, and $\eta$ will eventually be allowed to vanish ($\eta \to 0$). The second quantization Hamiltonian can now be constructed by applying the creation, $a^\dagger$, and annihilation, $a$, operators for fermions. Then the second quantized Hamiltonian, $\hat{H}$, can be reduced to [108, 140]:

$$\hat{H} = \frac{e^2}{a_0 r_s^2} \left( \sum_{\bar{k}\lambda} \frac{1}{2}\bar{k}^2 a_{\bar{k}\lambda}^\dagger a_{\bar{k}\lambda} + \frac{r_s}{2\bar{V}} \sum_{\bar{k}\bar{p}\bar{q}} \sum_{\lambda_1 \lambda_2} \frac{4\pi}{\bar{q}^2} a_{\bar{k}+\bar{q},\lambda_1}^\dagger a_{\bar{p}-\bar{q},\lambda_2}^\dagger a_{\bar{p}\lambda_2} a_{\bar{k}\lambda_1} \right). \tag{3.22}$$

Here $a_0 = \frac{\hbar^2}{me^2}$ is the Bohr radius, $V$ is the volume of the material, and $r_s$ is a normalized and dimensionless length variable, which is defined as:

$$r_s = \frac{r_0}{a_0}, \tag{3.23}$$

$$r_0 \equiv \sqrt[3]{\frac{4}{3}\pi \frac{N}{V}}, \tag{3.24}$$

$$n_0 = \frac{N}{V}. \tag{3.25}$$

At this point, it is worthwhile to derive the relationship between mean electron distance, $r_s$, and the Fermi energy, $E_F$, of the many electron system. This energy represents the lowest energy level at which all the states below are occupied by electrons. The electron density may be related to the Fermi wave vector, $k_F$ as:

$$n_0 = \frac{k_F^3}{3\pi^2}. \tag{3.26}$$

By combining Eqs. 3.26, 3.24, and 3.23, it can be shown that $k_F = \frac{1.9192}{a_0 r_s}$. Hence, the Fermi energy becomes:

$$E_F = \frac{3.6832}{r_s^2}E_{ry}, \tag{3.27}$$

where $E_{ry} = 13.60eV$ is the Rydberg energy and serves as a standard unit of energy.

Importantly, in Eq. 3.22, the first term on the right hand side represents the kinetic energy, $\hat{T}$, while the second term is for the potential energy, $\hat{V}$ of inter-electron Coulombic interactions:

$$\hat{T} = \frac{e^2}{a_0 r_s^2}\sum_{\bar{k}\lambda}\frac{1}{2}\bar{k}^2 a_{\bar{k}\lambda}^\dagger a_{\bar{k}\lambda}, \tag{3.28}$$

$$\hat{V} = \frac{e^2}{a_0 r_s^2}\frac{r_s}{2\bar{V}}\sum_{\bar{k}\bar{p}\bar{q}}\sum_{\lambda_1\lambda_2}\frac{4\pi}{\bar{q}^2}a_{\bar{k}+\bar{q},\lambda_1}^\dagger a_{\bar{p}-\bar{q},\lambda_2}^\dagger a_{\bar{p}\lambda_2} a_{\bar{k}\lambda_1}. \tag{3.29}$$

### 3.2.2 High density limit for a degenerate electron gas

In the high density limit for the case of the degenerate electron gas ($r_s \to 0$) and the inter electron distance becomes small. Inspection of Eqs. 3.22, 3.28, and 3.29 indicates that at high density limit the potential term, $\hat{V}$, becomes minimal and is indeed a perturbation for the kinetic energy term, $\hat{T}$. This is an interesting result, mainly because while the potential term is neither weak nor short range, the system can be solved through perturbation theory methods. The high density limit is a good approximation for metals, in which a high density electron gas exists with a positive background of ions. Hence, for metals it can conveniently be assumed that the electrons form a *free electron gas*.

## 3.3 Ground state energy of a many-electron systems

Calculation of the ground state energy (GSE) of a given many electron system is performed by various methods, the most well-known of which are perturbation theory, Hartree-Fock (HF) approximation, and density-functional theory methods. Regardless of the method of selection, the details of these calculations are mathematically involved and have been the subject of various advanced text books [108, 140, 141], and scholarly articles [142, 143]. The outcomes of the two simplest approximations– perturbation theory and HF methods–sufficiently provide insights on the physics of the devices that are discussed in this dissertation. Hence, here a brief introduction is presented on the specifics and outcomes of these methods.

The common general procedure in determining the GSE per particle, $E_{gse}$ is to expand it in terms of the energy of the equivalent non-interacting system, $E^{(0)}$, and additional energy terms, $E^{(i)}$ ($i = 1, 2, \ldots, \infty$), that are attributed to the potential

energies associated with inter-particle interactions:

$$E_{gse} = \frac{E}{N} = E^{(0)} + E^{(1)} + \sum_{i=2}^{\infty} E^{(i)}, \tag{3.30}$$

where $E$ and $N$ are the total energy and total number of electrons in the many-electron system.

The goal is now to find each term on the right hand side of Eq. 3.30. Various techniques exist for fulfillment of this step, however, the widely used methods are application of Green's function and Feynman diagrams, as well as perturbation theory. This step is usually mathematically involved and the method selection criteria heavily depend on the complexity of the problem, which remain as the major subject of concern in theoretical physics.

### 3.3.1 Hartree-Fock Approximation

The Hartree-Fock (HF) approximation assumes that the solution of the many-electron problem to have the form of the Slatter determinant of Eq. 3.5, that was described in Sec. 3.1.1.2. Consequently, the problem is reduced to finding the single-particle wave functions from the Hamiltonian of the many-electron system. Another simplification arises from the inclusion of interaction potential in the HF Hamiltonian. In this approximation, the interaction term is replaced by the mean field that is acting on an individual electron. This method ignores the dynamical behavior of electrons and any spatial correlation that mutual interactions among electrons causes in the energy of the system, and hence is inaccurate in this respect.

### 3.3.2 High electron density limit

As discussed in Sec. 3.2.2, at the high density limit of the degenerate electron gas ($r_s \to 0$), the system is treated by calculating the first order perturbation of the

potential term, $\hat{V}$ (Eq. 3.29), on the non-interacting Hamiltonian of the system. The overall Hamiltonian can be restated as the sum of the non-interacting Hamiltonian, $\hat{H}_0$, and the perturbation term, $\hat{H}_1$, as:

$$H\hat{}_{MES} = \hat{H}_0 + \hat{H}_1, \tag{3.31}$$

$$\hat{H}_0 \equiv \hat{T}, \hat{H}_1 \equiv \hat{V}. \tag{3.32}$$

Evaluation of the potential term is typically simplified through introduction of the HF approximation, by only accounting for the mean field of electron interactions. This results in the ground state energy per particle in this limit to become [140]:

$$\lim_{r_s \to 0} \frac{E}{N} = \frac{e^2}{2a_0} \left[ \frac{2.21}{r_s^2} - \frac{0.916}{r_s} + \mathcal{O}(r_s^0) \right]. \tag{3.33}$$

### 3.3.3 Exchange energy

The first term on the right hand side of Eq. 3.33 is the kinetic energy, while the second term is the so called *exchange* energy. The latter is a manifestation of Pauli's exclusion principle in the overall energy of the the interacting system and appears only in the quantum mechanical limit. Notably, the exchange energy contributes negatively to the GSE. Furthermore, this perturbation technique ignores the terms beyond the first order. These terms are called the correlation energies and are due to the Coulombic interactions among electrons that cause a spatial correlation in their position. For the case of the degenerate/homogenous electron gas, the exchange energy becomes:

$$E_x = -\frac{0.916}{r_s} E_{ry}. \tag{3.34}$$

### 3.3.4 Correlation energy

A major shortcoming of the Hartree-Fock approximation is in ignoring the high order interactions in the electron system. This approximation limits the usefulness of this method to the high density limit and cannot predict the energy term $\mathcal{O}(r_s^0)$ in Eq. 3.33. In fact, these energy terms can become significant at typical range of $1 < r_s < 6$ for metals. Consequently, it is essential to apply more advanced methods to determine higher order contributions to GSE, which are known as *correlation energy* terms, $E_c$. They account for spatial correlation in positions of electrons through Coulombic interactions. This is a major departure from the HF approximation, in which the effective mean potential field, due to a uniform electron distribution, was assumed. The techniques of *Random Phase Approximation* (RPA), linear response of the electron gas, and Green's function path integrals are among the methods of choice for evaluation of the correlation energy terms.

Inspecting Eq. 3.33 suggests an expectation of a power series expansion for the GSE with respect to $r_s$. The remaining terms can be calculated for the high density limit of homogenous electron gas, that is:

$$E_c = [-0.094 + 0.0622 \ln(r_s) + 0.018 r_s \ln(r_s)] E_{ry}, \tag{3.35}$$

and for the overall GSE to be [108]:

$$\lim_{r_s \to 0} E_{gse} = E_{kin} + E_x + E_c = \left[ \frac{2.21}{r_s^2} - \frac{0.916}{r_s} - 0.094 + 0.0622 \ln(r_s) + 0.018 r_s \ln(r_s) \right] E_{ry}. \tag{3.36}$$

### 3.3.5   Low electron density limit:Wigner lattice

At low electron densities in a homogenous electron gas, in which $r_s \to \infty$, and in the Hartree-Fock approximation of Eq. 3.33, the potential energy becomes the dominant term over the kinetic energy. This is because $E_{kin} \propto r_s^{-2}$, while $E_x \propto r_s^{-1}$. Hence it is expectedd [144] for electrons to form a solid lattice that would presumably be a close-packed structure such as bcc or ccc in three-dimension or a hexagonal form in a two-dimensional electron gas. A unit cell for this lattice is a sphere with a radius of $r_s a_0$ with an electron at the center. There is also a positive charge inside the unit cell, that neutralizes the overall charge. The localization of the positive background charge in this limit, is a deviation from the uniformity assumption of the degenerate electron gas. Hence, it becomes necessary to have a more accurate estimation for the potential energy of this system at low-density limit ($r_s \to \infty$).

Following the Wigner-Seitz model, the ground state energy at low-density limit becomes:

$$\lim_{r_s \to \infty} E_{gse} = \left[ \frac{2.21}{r_s^2} - \frac{0.916}{r_s} + E_c^{Wigner} \right] E_{ry}, \tag{3.37}$$

where

$$E_c^{Wigner} = \frac{0.88}{r_s + 7.8}. \tag{3.38}$$

The correlation energy that is given by Eq. 3.41 is correct for the low-density limit ($r_s \to \infty$) and fails to predict the right energy at high densities ($r_s \to 0$).

### 3.3.6   Intermediate electron densities

Practical materials have finite values for $r_s$, and estimation of the ground state energy that can account for the intermediate densities is critical. The GSE, however, will still follow the expansion format of Eq. 3.30, with individual terms being a function of $r_s$. In this case, the ground state energy is an interpolation of the two extreme

cases of the low- and high-density limits. Multiple interpolation schemes have been proposed, among which are the one by Nozieres and Pines [62], Carr and Maradudin [145], and Lindgren and Rosen (LR) [108]. The latter has better agreement with both the high-density limit of GSE of Eq. 3.36 and the low-density case of Eq. 3.37. The transitional ground state energy of LR is given by [108]:

$$E_{gse} = \left[ \frac{2.21}{r_s^2} - \frac{0.916}{r_s} + E_c^{LR} \right] E_{ry}, \tag{3.39}$$

$$E_c^{LR} = -\left[ r_s + 3 + 4\sqrt{r_s} - \frac{0.08}{\sqrt{r_s}} \right]. \tag{3.40}$$

### 3.3.7 Thermodynamic density of states

For a many electron system, the total energy of the system, $E$, is related to the GSE by following Eq. 3.30 as:

$$E = N E_{gse}(r_s). \tag{3.41}$$

The lack of experimental methods for direct measurement of the total and the ground state energies serves as a motivation to define and investigate other observable properties of the system that can be calculated from the derivatives of GSE with respect to the electron density, $n$. Specifically, the *pressure, P*, the *chemical potential, $\mu$,* and the *compressibility, K,* of the electron gas are of interest and can be calculated as:

$$\mu = \left( \frac{\partial E}{\partial N} \right)_V = \frac{\partial n E_{gse}(n)}{\partial n}, , \tag{3.42}$$

$$\frac{1}{nK} = -\frac{V}{n} \left( \frac{\partial P}{\partial V} \right)_N = \frac{\partial P}{\partial n} = n \frac{\partial \mu}{\partial n}. \tag{3.43}$$

The compressibility, $K$, of Eq. 3.43 is specifically of interest because of its dependence on the evolution of the chemical potential with electron density. For a free homogenous electron gas in which all interaction terms are suppressed, the compress-

ibility becomes $K_f = 3/(2E_F n)$. It can be shown that under HF approximation, a linear relationship holds between $K_f/K$ and $r_s$, as:

$$\frac{K_f}{K} = 1 - \frac{r_s}{6.02}. \tag{3.44}$$

This result is similar to the other ones that are achieved through more sophisticated assumptions, such as the one from RPA [146, 147], or that of Vashista and Singwi [148]. Particularly, the linear relationship with $r_s$ holds true for all of them, with the only difference being in the value of the denominator in the right hand side of Eq. 3.44. Interestingly, there exist a zero-crossing at a critical $r_s^{critical} \sim 6$. This means that for lower electron densities the compressibility is negative. Equivalently, at such critical $r_s$ value, insertion of additional electrons in the electron gas results in a decrease in chemical potential of the system. Conservation of energy requires that this decrement in $\mu$ to be restored elsewhere in the overall system. Furthermore, there exist no actual metal with $r_s > r_s^{critical}$. Hence, a corresponding critical electron density of $n_{critical}$ can be defined in a way that the electron gas displays "metallic" properties for $n > n_{critical}$, while an "insulating" state occurs for $n < n_{critical}$. Experimental examination of this model, however, is not possible in three-dimensional materials as there is no method for varying the volume electron density. Fortunately, two-dimensional electron system can be achieved in various material structures, as described in Chapters 1 and 2. The density of these 2D electron system can be varied through field effect or by light generated carriers.

## 3.4 A two-dimensional many-body fermion system

The concepts of the many-electron system that were discussed in previous sections of this chapter are independent of the spatial dimensionality of the system, and they

were quantified, however, for three-dimensional (3D) homogenous electron system of "jellium" model [108, 140, 141]. A fundamental challenge in testing the proposed models exist in experimentation of three-dimensional systems. Mainly, the total and per particle ground state energy terms cannot be measured directly through experiment. The principles of conservation of energy and momentum in a non-relativistic condition can be of assistance for designing experiments that probe the variations of GSE with a *macroscopically controllable variable* such as electron density, $n$. Hence a successful method should address the following requirements:

I. Probing the dynamics of energy transfer, relaxation and restoration in the overall system under test,

II. Relating the macroscopic measurable e.g. chemical potential and particle density to the microscopic GSE,

III. Including at least one controllable independent variable (mainly particle density).

There exist experimental methods that can accomplish the objectives of the first item in this list. Notably, the electric-field penetration technique [149, 150] and the differential capacitance measurement method [26] are applied for this purpose. These will be discussed in Sec. 3.5. The analytical principles that address the second item were defined in Sec. 3.3.7 through introduction of the compressibility, chemical potential and their dependence on macroscopic electron density. Item III in the list emphasizes the controllability requirement of the independent variable. This is the main discouragement for testing 3D many-electron systems, as it is impossible to change the electron density in metals. This can be resolved, however, by selecting two-dimensional (2D) many-electron gas as the system under test. For instance, the density of 2D electron systems (2DES) is commonly set through a gate voltage in field

effect transistors. Additionally, many established and novel 2D material systems, such as high-electron mobility transistors, graphene, oxides etc., are available, in which a 2DES exists and its density can be controlled. In this section, the major properties of a 2D many-fermion system are described with the intention of its application in experimental test set-up.

### 3.4.1  Ground state energy for a 2DFS

All the principles that were described for a three-dimensional many fermion system in previous sections are valid for a 2D election gas as well. The major difference, however, is on the electron interaction potential term, $H_{el}$, term in the many-body Hamiltonian that leads to quantitative deviations in the GSE for the 2D case. The Coulomb potential field of an electron takes the form of $v = \frac{e^2}{r}$. This indicates the long (and practically infinite) range of the Coulombic interaction. Application of this potential field in the Hamiltonian of the jellium model causes convergence problems in the overall interaction integral. In a mathematical procedure, known as *coulomb interaction regularization,* the interaction potential is replaced with one with a very long, yet finite, range and the overall system is analyzed in the limit in which this range is much larger than any other physical length scale except the spatial dimension of the device, $L$. A convenient choice for this potential is known as "Yukawa" interaction [151], in which:

$$v(r, \kappa) = e^2 \frac{exp(-\kappa r)}{r},$$ 

(3.45)

and $e = 1.6 \times 10^{-19} C$ is the charge of an electron. The solution to the many body problem essentially converges to that of a system with Yukawa interaction potential in the limit of $\kappa \to 0$. The same procedure was taken into account for derivation of the many-body Hamiltonian, $\hat{H}_{MBS}$ of Eq. 3.22. In systems with lower spatial

dimensionality, it is the interaction potential that is different from the 3D case. This is better understood by investigating the Fourier transform of the interaction potential:

$$v_q(\kappa) = v(q, \kappa) = \int v(q, \kappa) e^{-i\vec{q}.\vec{r}} d\vec{r}. \tag{3.46}$$

The value of the integral in Eq. 3.46 depends on the dimensionality of the system, i.e.,

$$v_q(\kappa) = \begin{cases} \frac{4\pi e^2}{q^2 + \kappa^2}, & 3-D, \\ \\ \frac{2\pi e^2}{\sqrt{q^2 + \kappa^2}}, & 2-D. \end{cases}$$

Taking the limit $\kappa \to 0$ in the above expression results in the interaction potential as:

$$v_q(\kappa) = \begin{cases} \frac{4\pi e^2}{q^2}, & 3-D, \\ \\ \frac{2\pi e^2}{q}, & 2-D. \end{cases}$$

Eq. 3.4.1 indicates that the interaction potential has different range and strength which depends on the dimensionality of the system. The rest of the procedure for computing the GSE for a 2DFS is similar to the 3D case, that was explained in Sec. 3.2. The inter particle mean distance corresponding to a two-dimensional electron density, $n_{2D}$, becomes $r_s = \frac{(\pi n)^{-1/2}}{a_0}$. The outcomes for the three cases of high, low and moderate electron density in a 2DFS case are as the following:

**High density limit:** Following the random phase approximation (RPA) theory [185], the ground state energy in the 2D case becomes[141]:

$$\lim_{r_s \to 0} E_{gse}^{2D} = \left( \frac{1}{r_s^2} - \frac{1.2}{r_s} - (0.38 \pm 0.04) - 0.1726 r_s \ln r_s + \mathcal{O}(r_s) \right) E_{ry}. \tag{3.47}$$

**Low density limit:** Here a 2D electron Wigner solid is formed with a hexagonal lattice and using the quantum Monte Carlo numerical techniques [152], the

ground state energy becomes:

$$\lim_{r_s \to \infty} E_{gse}^{2D} = \left( \frac{-2.21}{r_s} + \frac{1.59}{r_s^{3/2}} + \frac{0.15}{r_s^2} \right) E_{ry}. \qquad (3.48)$$

**Intermediate density limit:** The ground state energy for a 2D electron system at intermediate electron densities becomes: [153]

$$E_{gse}^{2D} = \left( \frac{1}{r_s^2} - \frac{1.2}{r_s} e^{-1.39 r_s} - 0.38 + (0.086 r_s + 0.057 r_s^2 + 0.003 r_s^3) \right.$$

$$\left. \times \ln(1 + \frac{1}{1.002 r_s - 0.021 r_s^{3/2} + 0.340 r_s^2 + 0.002 r_s^3}) \right) E_{ry}. \quad (3.49)$$

### 3.4.2 Significance of exchange-correlation energies in 2D

Reduced dimensionality thus increases the contribution of the exchange and correlation energies to the ground state energy. Table 3.1 summarizes the values for GSE in 3D and 2D and for all the electron density limits. It can be seen that for a 2DES, the kinetic energy term takes a lower value compared to its 3D counterpart. More importantly, the ratio of the exchange and correlation energies to the kinetic term is larger in lower dimensions. This indicates the significance of the quantum mechanical exchange and correlation energies in lower dimensions.

### 3.4.3 Compressibility for a 2DFS

Experimental procedures are required to verify the theories described in previous sections. A macroscopically measurable is required to be identified that could probe the microscopic energy evolutions with variations in $r_s$. For this reason, compressibility of a 2DFS is specifically interesting as it may be quantified experimentally. It is essential to derive the relation between the compressibility, the ground state energy, and the inter-particle distance $r_s$. Eq. 3.43 provides a dimensional-independent

Table 3.1: Ground State Energy dependence on dimensionality.

| GSE | | = Kinetic + | Exchange + | Correlation |
|---|---|---|---|---|
| $\lim_{r_s} E_{gse}(r_s)$ | | $= E_{kin}(r_s)+$ | $E_x(r_s)$ + | $E_c(r_s)$ |

| | | Kinetic | Exchange | Correlation |
|---|---|---|---|---|
| $r_s \to 0$ | 3D : | $\frac{2.21}{r_s^2}$ + | $(-\frac{0.916}{r_s})$ + | $(-0.094 + 0.0622\ln(r_s) + 0.018 r_s \ln(r_s))$ |
| | 2D: | $\frac{1}{r_s^2}$ + | $(-\frac{1.2}{r_s})$ + | $-(0.38 \pm 0.04) - 0.1726 r_s \ln r_s$ |
| $0 < r_s < \infty$ | 3D: | $\frac{2.21}{r_s^2}$ + | $(-\frac{0.916}{r_s})$ + | $-\left(r_s + 3 + 4\sqrt{r_s} - \frac{0.08}{\sqrt{r_s}}\right)$ |
| | 2D: | $\frac{1}{r_s^2}$ + | $(-\frac{1.2}{r_s}e^{-1.39 r_s})+$ | $\Big[ -0.38 + (0.086 r_s + 0.057 r_s^2 + 0.003 r_s^3)$ $\times \ln(1 + \frac{1}{1.002 r_s - 0.021 r_s^{3/2} + 0.340 r_s^2 + 0.002 r_s^3})\Big]$ |
| $r_s \to \infty$ | 3D: | $\frac{2.21}{r_s^2}$ + | $(-\frac{0.916}{r_s})$ + | $\frac{0.88}{r_s+7.8}$ |
| | 2D: | $\frac{0.15}{r_s^2}$ + | $(-\frac{2.21}{r_s})$ + | $\frac{1.59}{r_s^{3/2}}$ |

definition for compressibility, and the respective GSE equation from Table 3.1 can be utilized to find the compressibility and the chemical potential for a $d$-dimensional system:

$$\mu = \left(\frac{\partial E}{\partial N}\right)_V = E_{gse}(r_s) - \frac{r_s}{d} E_{gse}'(r_s),, \tag{3.50}$$

$$\frac{1}{nK} = n\frac{\partial \mu}{\partial n} = \frac{r_s}{d}\left[\frac{1-d}{d}E_{gse}'(r_s) + \frac{r_s}{d}E_{gse}''(r_s)\right]. \tag{3.51}$$

The normalized compressibility, $\frac{K_f}{K}$, then follows from Eq. 3.51:

$$\frac{K_f}{K} = 1 + \frac{d+1}{d+2}\frac{E_x(r_s)}{2E_{kin}(r_s)} - \frac{r_s}{2E_{kin}(r_s)(d+2)}\left[(d-1)E_c'(r_s) - r_s E_c''(r_s)\right]. \tag{3.52}$$

### 3.4.4 Phase transition in a 2DFS

Interestingly, investigation of Eq. 3.52 indicates that for the jellium model at low densities of $r_s > 2.03$ in 2D and $r_s > 5.25$ in 3D the compressibility, $K$, becomes negative. This is in contrast with the necessary condition for the stability of a thermodynamic system, as it requires $K > 0$. In reality, the stiffness of the positive background compensates for the negative compressibility of the electron gas and maintain the overall stability of the system. This is, however, a deviation from the initial assumption of charge uniformity in jellium model [141]. Furthermore, since $K^{-1} \propto \frac{d\mu}{dn}$, a negative compressibility infers that a decrement in charge density results in an enhancement in chemical potential. Conversely, this contradicts the predictions of classical thermodynamics, and this feature is exclusive to quantum many-electron system.

The anti-symmetric nature of the fermions and long-range Coulombic interactions among electrons adds the exchange and correlation energy terms that contribute negatively to the GSE, also seen in Table 3.1. As the electron density decreases $(r_s \to \infty)$, at certain critical value of $r_s^{critical} = 2.03$ in 2D and $r_s^{critical} = 5.25$ in 3D, the exchange and correlation energy terms become larger than the kinetic energy and both the chemical potential, $\mu$ and the compressibility $K$ become negative. These critical points are the transition from a metallic phase $(r_s \to 0)$ to an insulating phase $(r_s \to \infty)$. At the metallic phase, the Coulombic interactions are treated as a perturbation on the kinetic term, while in the insulating phase the latter becomes insignificant and the whole system approaches the state of a Wigner lattice.

### 3.4.5 Critical carrier densities for a metal-insulator transition

Electron density is the main macroscopic measurable in electronic and photonic devices, hence it is helpful to determine the electron densities that correspond to the

critical inter particle distance, at which a metal-insulator transition (MIT) occurs for a many-electron system [181, 188]. Since $r_s a_0$ is the radius of the $d$-dimensional sphere it encloses, on the average, one electron, the electron density is given by:

$$\frac{1}{n} = \begin{cases} \frac{4\pi}{3}(r_s a_0)^3, & 3 - D, \\ \pi(r_s a_0)^2, & 2 - D. \end{cases}$$

For the critical $r_s^{critical}$ of a MIT that was calculated in Sec. 3.4.3, the corresponding critical densities become:

$$\begin{aligned} r_s^{critical}\Big|_{3D} &= 5.25 \leftrightarrow n_{critical}^{3D} = 1.11 \times 10^{22} cm^{-3}, \\ r_s^{critical}\Big|_{2D} &= 2.03 \leftrightarrow n_{critical}^{2D} = 4.13 \times 10^{14} cm^{-2}. \end{aligned} \tag{3.53}$$

The critical densities of Eq. 3.53 are valid for many-electron systems of a jellium model. In practical structures, however, the values of the effective mass, $m_e^*$, and the dielectric constant $\epsilon_s$ are set by the background material. For instance, for GaAs the effective mass and dielectric function are $m_e^* \simeq 0.067 m_e$, and $\epsilon_s \sim 12$, respectively. Consequently, it is required to define the effective Bohr radius, $a^*$ for the material of interest according to:

$$a^* = \frac{\hbar^2 \epsilon_s \epsilon_0}{m^* e^2} = \frac{\epsilon_s}{m^*} a_0. \tag{3.54}$$

For the case of GaAs the resulting effective Bohr radius is $a_{GaAs}^* \simeq 9.5 nm$, which is much larger than that of the hydrogen atom ($a_0 = 0.5294 Å$). In GaAs then, the de Broglie wavelength of an electron is comparable with the effective Bohr radius and the overlap of wave functions for electrons is enhanced. This enhances the inter-electron interactions, hence the $r_s^{critical}$ value for GaAs becomes much smaller compared to Eq. 3.53. Consequently, any calculation of the critical particle density for a MIT has

to account for the effective Bohr radius of the host material.

## 3.5 Unconventional capacitors with 2DFS

Two dimensional charge systems can be utilized to replicate metallic contacts for electrical connection. Specifically, a set of "unconventional" devices can be imagined by substitution of conventional metal contacts by a 2DCS counterfeit. For instance an "Unconventional" capacitor (UC) has a 2DCS replacing one or both of its metal plates. Unlike metals, however, the particle density of an artificial 2DCS can be varied through an applied external field, such as electric potential, or through deposition of carriers generated by incident photons. Following the discussions in Sec. 3.4, the carrier density in a 2D fermion system determines its ground state energy, comprised of the kinetic, exchange and correlation energy terms. Variations in the carrier density of 2DCS, hence, provides a degree of freedom in manipulating the GSE and control the performance characteristics of any unconventional device that includes a 2DCS. Specifically, in an unconventional parallel plate capacitor the evolution of the chemical potential (and the GSE) with carrier density can be traced through measurement of differential capacitance of the UC. Compressibility of the 2DCS can then be extracted to verify the theoretical predictions of Sec. 3.4.

### 3.5.1 Finite density of states in a 2DFS

In classical mechanics, it is a fact that a metal plate screens the electric field around it, hence if such a plate is inserted in a parallel plate capacitor, as in Fig. 3.1(a), the overall capacitance becomes $C_{tot} = C_1 = \epsilon_1/d_1$, in which $C_1$ is the geometric capacitance of the inserted and the top plate with $d_1$ being the distance between the planes, and $\epsilon_1$ is the dielectric constant of the enclosed medium. The equivalent circuit is indicated in Fig. 3.1(b). In contrast to this is the case where the inserted

plate is replaced with a two-dimensional fermion system(Fiq. 3.1(c)). Such a system is typically attained in a quantum well in III-V semiconductor heterojunctions [16, 37, 134, 154, 155], the inversion layer of field effect transistors [156, 157, 158], or other novel material structure [13, 14, 15, 38, 159] as detailed in Chaps. 1 and 2. Here an additional capacitive mechanism is defined as a "quantum capacitance," $C_Q$, that is found by [22]:

$$C_Q = g_v \frac{m^* e^2}{\pi \hbar^2}, \tag{3.55}$$

in which $g_v$ is the valley degeneracy factor and $m^*$ is fermion effective mass in a direction transverse to the 2D plane. This quantum capacitance effect is a property of the many-body 2D system, and has a different origin from inversion-layer capacitance in field effect transistors. Since Pauli's exclusion principle requires a finite energy expenditure for addition of an extra fermion to a many-particle system, the density of states (DOS) of this system becomes finite. In the unconventional structure of Fig. 3.1(c), the Fermi level of the 2DFS is kept constant. Hence it can not accommodate an increment of charge $dq$ due to its finite DOS. The conservation of energy, however, requires any potential variation of $dV$, that is applied to the top plate, and hence its associated electric field $dE$, to penetrate through the 2D plane. The equivalent circuit, then takes the form of Fig. 3.1(d). In the classical limit, at which $\hbar \rightarrow 0$, the quantum capacitance $C_Q \rightarrow \infty$ and the system is reduced to the capacitance of $C_1$.

The quantum capacitance of Eq. 3.55 depends on the effective mass. For electrons in the inversion layer of a Si-based FET, $m* = 0.98m_0$, hence $C_Q$ is much larger than any geometric capacitance at the practical sizes of FETs. Hence no significant effect from $C_Q$ is generally observed in the capacitance performance of conventional FETs. In devices that are based on other materials, such as GaAs, in which the effective mass is much smaller $(m*|_{GaAs} = 0.067m_0)$, the quantum capacitance becomes critical in determining the overall performance of the device [8, 22, 23, 24, 26, 89, 149, 150,
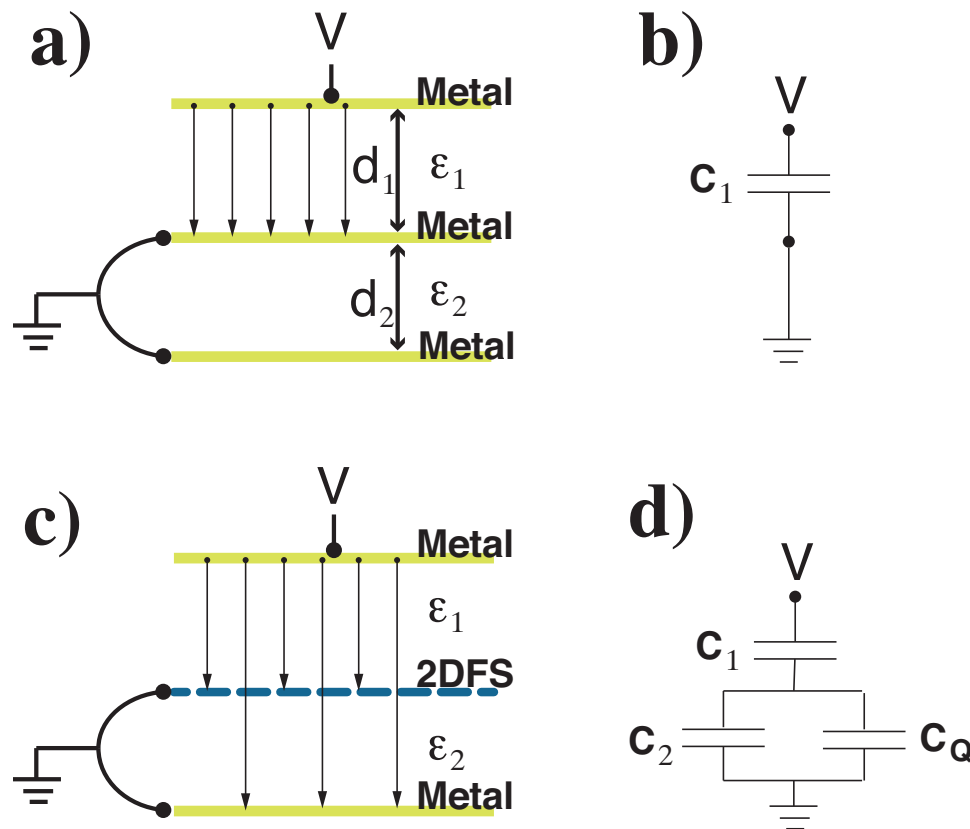
Figure 3.1: a) A series of three parallel metal sheets, with the middle metal screening all the electric field, b) the equivalent circuit model for the structure in (a), c) a structure similar to (a) but with a 2D fermion system utilized as the middle plate; electric field lines penetrate through the 2DFS, as it has a finite density of states, and d) the equivalent circuit model for the structure in (c); notably, additional capacitive elements of $C_Q$ and $C_2$ appear in the model because of quantum nature of the 2DFS.

159, 160, 161, 162, 163, 164, 165]. This feature of the 2DFS is utilized to construct experiments for probing the GSE of the many-body system. As a final note, the quantum capacitance, as defined in Eq. 3.55, is merely a consequence of the finite density DOS that originates from Pauli's exclusion principle. Another capacitive mechanism is also related to the Pauli's exclusion principle, however, that is due to the anti-symmetry wave function and indistinguishability of fermions. The latter is called the "exchange" capacitance and will be the subject of discussion in Sec. 3.5.4.

### 3.5.2 Experimental measurement of the ground state energy of a 2DFS

The standard experimental method for probing the thermodynamic density of states for a 2DFS is based on a "field penetration technique" [149]. Fig. 3.2 shows the general scheme for performing this measurement. In this method two layers of 2DES are places in parallel with each other and under a top gate contact. A DC bias voltage, $V_g$, is applied to the top gate, which induces an electric field $E_0$ and controls the density of the 2DES. An ac voltage, $V_{ac}$ is also superimposed to $V_g$ that adds an increment of electric field, $\delta E_0$ to the DC field. Since the 2DES has a finite density of states, as described in Sec. 3.5.1, the electric field penetrates through the top 2DES and reaches the bottom (2D) layer. Hence, a signal voltage $V_{sig}$, which is proportional to the penetrated field, $\delta E_p$, can be measure at the bottom 2DES layer. The thermodynamic density of states $(d\mu/dn)$ for the top and bottom 2DES layers are then found from the ratio $\delta E_p/\delta E_0$ [149, 150]:

$$\frac{\delta E_p}{\delta E_0} = \frac{d_t}{a^* + d_t + d_b},\tag{3.56}$$

$$\text{where} d_{t,b} = (\frac{\epsilon_r \epsilon_0}{e^2}) \times \frac{\partial \mu_{t,b}}{\partial n_{t,b}},\tag{3.57}$$

and $a^*$ is the effective Bohr radius, $n$ is the electron density, and subscripts $t$ and $b$ denote the top and the bottom 2DES layers, respectively.

### 3.5.3 Classical definition of capacitance

The mutual capacitance, $C$, between two conductors is defined as the amount of charge that can be stored on each plane, $Q$, per unit of voltage difference between the planes, $V$.

$$Q = CV\tag{3.58}$$
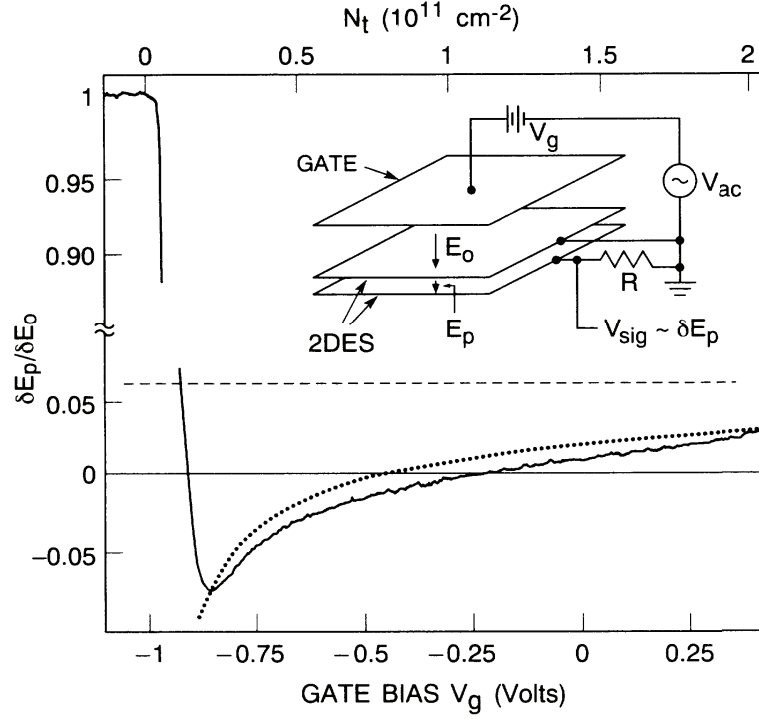
Figure 3.2: Experimental set up for measuring the compressibility by Eisenstein et al [150].

Classical calculation of this capacitance is generally done by applying Gauss's and Poisson's equation for a given system. Conventional capacitors are composed of two metallic electrodes that are separated by a dielectric medium. The geometry of each electrode can be arbitrary. Following classical electrostatics, if a charge of $+Q$ is delivered to one of the electrodes, a charge of $-Q$ will be induced on the other electrode in order to keep the overall system neutral. An electric field, $\vec{E}$, then exists between the electrodes and is calculated through applying Gauss's law:

$$Q = \oiint_S \epsilon_r \epsilon_0 \vec{E}.d\vec{A}, \tag{3.59}$$

where $d\vec{A}$ is a vector representing an infinitesimal element of area, $\epsilon_r$ is the relative dielectric constant of medium, and $\epsilon_0$ represents the dielectric constant of the vacuum.

The electric field $\vec{E}$, the charge distribution $Q$, and the potential are related through Poisson's equation as:

$$\nabla^2.V = \frac{Q}{\epsilon_r \epsilon_0}. \tag{3.60}$$

The rest of the problem becomes a matter of algebraic calculations of the integrals in Eqs. 3.59 and 3.60. The most well-known instance of this classical problem is the case of a parallel plate capacitor with two metallic electrodes with area $S$ and separation distance of $d$. The geometrical capacitance is:

$$C = \frac{\epsilon_r \epsilon_0 S}{d}. \tag{3.61}$$

Importantly, the capacitance, in its classical calculation, is solely determined by the geometry of the system and the dielectric properties of the medium. Hence it is often called the "geometrical" capacitance for a given structure. Additionally, classical electrostatics require any conductor to be equipotential, hence for a capacitor all the voltage difference between the conducting planes essentially drops across the dielectric. The work, $dW$, that is required to add an increment charge of $dq$ to capacitor plates with charge $q$ and against the potential $V$ is provided by an external force, and equals:

$$dW = V.dq = \frac{q}{C}dq. \tag{3.62}$$

Hence, total energy to place total charge of $Q$ against a potential difference $V$ on capacitor plates is derived by integration of Eq. 3.62:

$$W_{charging} = \int dW = \int_0^Q \frac{q}{C}dq = \frac{1}{2}\frac{Q^2}{V} = \frac{1}{2}CV^2. \tag{3.63}$$

This energy is stored in the electric field that exists between the capacitor plates, and:

$$W_{storage} = W_{charging}. \tag{3.64}$$

In the classical definition of capacitance, the energy expenditure is only for keeping the charges separated by the distance between the capacitor plates. Hence the amount of the work for adding an increment of charge to a metal contact is zero. Equivalently the chemical potential of the individual plates of the capacitor does not change with addition of charge. This assumption is valid for metals, in which adding an extra electron to the metal does not significantly change the total energy of the system. Conversely, if the metal contact is substituted by an "unconventional" system of charge, such as a 2D fermion system, the amount of energy that is required to add an increment of charge to the system becomes non-zero, and depending on the properties of the 2DFS, it can become a significant factor. It is thus necessary to define new capacitive mechanisms that account for such energy dynamics inside the 2DFS.

### 3.5.4 Revisiting capacitance definition for an unconventional capacitor

When a 2DFS substitutes one or both plates of a parallel plate capacitor, the classical electrostatics will not be valid anymore. Specifically, following the discussions of Secs. 3.3 and 3.4, adding an incremental charge of $dq$ to the unconventional plate requires a non-zero energy expenditure $d\mu$ and the chemical potential,$\mu$, of the many-body system changes. This is in contrast with classical calculations, in which $d\mu = 0$. In an unconventional parallel plate capacitor, the overall energy of the device has to account for the quantum mechanical energy terms for both plates:

$$E_{tot} = E_{Hartree} + \sum_i E_{kin,i} + \sum_i E_{ex,i} + \sum_i E_{corr,i} + \sum_i E_{ext,i} \tag{3.65}$$

$$C_{tot}^{-1} = C_{geo}^{-1} + \sum_i C_{kin,i}^{-1} + \sum_i C_{ex,i}^{-1} + \sum_i C_{corr,i}^{-1} + \sum_i C_{el-ncc,i}^{-1} \qquad (3.66)$$

The exchange capacitance becomes [89]:

$$4\pi\epsilon_0/C_{ex,i}^{(2D)} = -\sqrt{2}a_B r_s/\epsilon_{eff,i}, \qquad (3.67)$$

and the correlation capacitance is defined as:

$$4\pi\epsilon_0/C_{corr,i}^{(2D)} = \frac{\pi a_B r_s^2}{\epsilon_{eff,i}} \frac{a_0}{y}\left[ -\frac{3}{32}u + \left(1 + \frac{3}{4}u\right)\frac{x}{y} + (1+u) \times \left(\frac{x^2}{y^2} - \frac{z}{y}\right)\right], \quad (3.68)$$

where $u$, $x$, $y$, and $z$ are auxiliary coefficients that depend on $r_s$ and are defined as:

$$u(r_s) = 1.13r_s^{0.5}, \qquad (3.69)$$

$$y(r_s) = 1 + 1.13r_s^{0.5} + 0.9052r_s + 0.4165r_s^{1.5}, \qquad (3.70)$$

$$x(r_s) = \frac{1.13}{4}r_s^{0.5} + \frac{0.9052}{2}r_s + \frac{3}{4} \times 0.4165r_s^{1.5}, \qquad (3.71)$$

$$\text{and } z(r_s) = \frac{5}{32} \times 1.13r_s^{0.5} + \frac{3}{8} \times 0.9052r_s + \frac{21}{32} \times 0.4165r_s^{1.5}. \qquad (3.72)$$

## 3.6   Conclusion

In this chapter, the theoretical background for a quantum many fermion system was described. A second quantization approach was taken by which the property of indistinguishability of fermions was inherently accounted for. By using this method, the number density of the particles and the ground state energy of the system were calculated. It was shown that for a correlated system of fermions (electrons), exchange and correlation energy terms exist in addition to the kinetic energy of the particles. The contribution of these energy terms to the ground state was negative. Importantly, these energy terms depend on the electron density and the degree of freedom

in spatial dimensionality of the system. Specifically, the exchange-correlation energies are emphasized for a 2D system due to higher level of Coulombic correlations among electrons. Furthermore, capacitive mechanisms related to exchange and correlation energies, were identified in an unconventional capacitor at which a 2DES comprises one or both plates. Such quantum capacitors may contribute negatively to the overall equivalent capacitance of the unconventional device. In the next chapter, these capacitive mechanisms are observed and described in the C-V characteristics of unconventional MSM-2DCS devices. Moreover, methods for judicious manipulations of the exchange and correlation energies are presented and applied for electronic and photonic applications.

## 4. Correlated 2D charge systems for optoelectronic applications

The quantum mechanical exchange and correlation energy terms were identified in Chap. 3 to contribute negatively to the ground state energy of a many-fermion system. It was shown (3.1) that reduced spatial dimensionality emphasizes their contribution to the overall energy. Furthermore, these energies are dependent on the inter-particle distance, $r_s$, hence can be controlled by varying the particle density. At this chapter, exchange and correlation energies are manipulated by means of a bias voltage and light-generated carriers in unconventional MSMs.

### 4.1  Anomalous features in capacitance of MSM-2DES varactor

Moderation of internal quantum mechanical energies, such as exchange energy of an unconventional contact, comprised of a system of two-dimensional charge carriers, improves performance merits of varactors, mainly in tuning ratio and sensitivity. Energy transfer from the unconventional contact to the dielectric increases energy density and enhances the capacitance of the varactor. The anomalous capacitance enhancement was observed in the C-V characteristics of the MSM-2DES varactor in Chap. 2. The explanation of the underlying physics for this "Batman" shape CE is the subject of this section. We argue that manipulation of ground state energy of the embedded correlated 2DCS account for the exotic features in the C-V. Furthermore, a new photodetector device is proposed in Sec. 4.2 that functions based on light-triggered capacitance enhancement in an "unconventional" MSM with a 2D hole system.

### 4.1.1 Very large capacitance enhancement in an MSM-2DES capacitor

The C-V characteristics of the MSM-2DES capacitor (Fig. 2.9) includes an anomalous capacitance enhancement feature, that resembles a "Batman" shape. At around a threshold voltage of $V_{th}$, the capacitance of the device increases by up to 26% from the pre-threshold capacitance of $C_{2DES}$. This is in contrast with semi-classical expectation, following the charge control model (Sec. 2.2.9) [30], that predicts a gradual decline in capacitance with depletion of the electrons from the "unconventional" contact. Distinctively, the CE for the MSM-2DES capacitor occurs at probe frequencies of up to $500kHz$ and at room temperature, while prior reports on CE had observed it only up to 'tens' of Hertzs.

Interestingly, the CE feature was not observed in the C-V of the control device of Chap. 2 that lacked the 2DES. Hence, it can be attributed to the quantum aspects of the 2D electron layer discussed in Chap 3. The existence of the CE feature, also, positively impacts the performance of the MSM-2DES as a varactor. The tuning ratio of this MSM-2DES varactor increases linearly with the peak capacitance in C-V. Hence, with a 26% increase in maximum capacitance, that is achieved at the peak of the "Batman" shape of CE, the tuning ratio improves with the same relative value. Similar CE features have been proposed as a gate capacitance enhancer for MOSFETs [26] as an alternative to high-$\kappa$ dielectric materials [184].

### 4.1.2 Metal-insulator transition (MIT) in MSM-2DES capacitor

In Sec. 2.2.10 three charge control mechanisms were identified for the capacitance performance of the MSM-2DES capacitor:

1. $C_{2DES}$ : the quasi-constant pre threshold capacitance that has the 2DES underneath the cathode for its "unconventional contact.

2. $C_{lat}$ : the post-threshold lateral capacitance with the edge of the preserved 2DES as its "unconventional" contact.

3. $C_{bulk}$ : the post-threshold depletion capacitance of the Schottky-semiconductor junction.

While these mechanisms were identified by a semi-classical charge control model, the concepts of many-body interactions can be applied to them. Specifically, $C_{2DES}$ and $C_{lat}$ both include certain forms of a correlated many-electron contact and can be treated by the theory of Sec. 3.5 for "unconventional" capacitors. $C_{2DES}$ and $C_{lat}$ have the 2D plane of electrons underneath the cathode and the quasi 1D edge of the conserved 2DES in the gap as their respective unconventional plates. The essential theory for treating the correlated 1D charge system will be addressed in Chap. 5.

The giant "Batman" shaped CE feature is attributed to the negative compressibility of the 2DES. It is manifested as a negative exchange-correlation capacitor, $C_{ex-corr}$, that is in series with the geometrical capacitance of the plate capacitor. It has been previously observed for a two-dimensional electron system and is attributed to the negative compressibility of the 2DES [26], which occurs when the 2DES transitions from a high density interacting system to a depleted non-interacting one. This is due to negative thermodynamic density of states for a 2DEG [25]. Here, the addition of exchange and correlation energies of the interacting many-body system of 2DEG, as the unconventional contact, to the stored energy inside the electric field of the dielectric, results in an enhancement in the overall capacitance, as an energy storage device [23, 24].

To the lowest order of approximation, Coulombic interactions produce a negative exchange contribution to the chemical potential of the electron system. This term that is inversely proportional to the mean inter-electron spacing, $r_s$, as described in Chap. 3, exceeds the kinetic energy at low densities. With $K_0$ being the compress-

ibility of the non-interacting system, for a 2DES, the ratio $K/K_0$ declines linearly with an increase in $r_s$, and becomes negative at $r_s = 2.2$ in the limit of the Hartree-Fock approximation. It corresponds to a critical density $n_{critical} = 6.5 \times 10^{10} cm^{-2}$ for GaAs [150]. In other approximations, such as the one by Tanatar and Ceperley [142], $n_{critical}$ is 20% larger than the one by Hartee-Fock. The electron concentration of the 2DES layer for the MSM-2DES capacitor was calculated by the charge control model (Sec. 2.2.10) to be $n_{2DES} = 4.6 \times 10^{11} cm^{-2}$, which is greater than the critical value; hence, this 2DES is in a metallic phase in which the positive kinetic energy term is the dominant factor in the ground state energy. By applying a bias voltage between the anode and cathode, the latter Schottky contact will be inversely biased, and its depletion field depletes the 2DES underneath. At $V_{CE} = 1.5V$, the electron density reaches the critical value: $n_{2DES}|_{1.5V} \sim n_{critical}$, at which the negative exchange and correlation terms become equal or greater than the kinetic energy, hence the compressibility becomes negative (see sec.3.4.3) and the 2DES enters an insulating phase. This metal-insulator transition is typically observed as an enhancement in capacitance [26, 89], that is larger than the geometrical value associated with the structure as was shown in Sec. 3.5. Consequently, in this unconventional MSM-2DES capacitor, exchange and correlation energies are controlled by manipulating the 2DES density. As a result, device performance as a varactor is greatly improved surpassing geometrical capacitance values, hence setting a performance record.

### 4.1.3   C-V characteristics under a light source

Fig. 4.1 compares the dark and under illumination C-V characteristics of the "small" MSM-2DES capacitor with $5\mu m$ of pad separation. A white microscope light was incident on the device, however, the specifics of the illumination remained uncharacterized. The C-V under illumination exhibits features that are starkly different

from the dark. Interestingly, a giant secondary peak that takes a shape similar to a sail, as large as $50pF$ at $PF = 10kHz$, appears at the post-threshold bias voltages ($\sim V_{bias} = 3.9V$). The peak value decreases with an increase in probe frequency. Such behavior is entirely absent in the dark C-V at similar probe frequency range. Furthermore, no negative capacitance exists in the C-V under light. At its peak, the capacitance under light, $C_{light}$, becomes more than 12 times greater the dark value, $C_{dark}$, at the same bias point. This C-V characteristics under an illumination resemble that of the MSM-2DES at dark that were measured at frequencies less than $3kHz$ (see Fig. 2.9). This "sail" shape peak exists in addition to the "Barman" shape capacitance enhancement feature. The "Barman" CE feature in the C-V un-
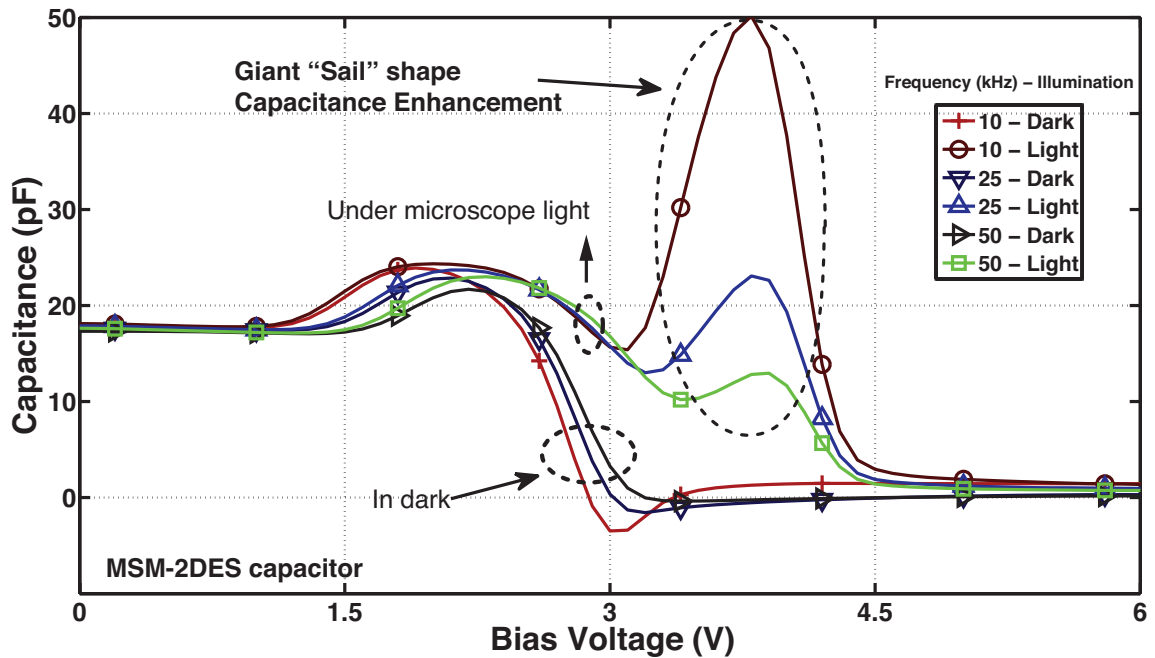


Figure 4.1: Capacitance-Voltage of MSM-2DES capacitor under microscope light.

der light does not exhibit significant differences, in magnitude and shape, with the

one observed at dark. The bias voltage at which the peak of the CE is observed and the threshold voltage, where an abrupt decline in C-V occurs, however, increases by $\sim 0.25V$ in presence of an illumination. This shift is expected since addition of the light-generated electrons to the 2DES increases its density which then requires a greater bias voltages to be fully depleted from underneath the cathode. It can be concluded that the "Batman" CE that is observed in C-V under illumination incurs the same physical origin similar to its counterpart in the dark C-V, as explained in Sec. 4.1.1.

The "sail" CE feature that is present in the C-V under illumination is its major distinction with the one in the dark. It occurs at bias voltages that the 2DES underneath the cathode is totally depleted and the main charge control mechanisms are due to $C_{lat}$ and $C_{bulk}$. The latter is not expected to exhibit significant changes under light, as the incident microscope light is neither coherent nor of high intensity, hence the bulk carrier distribution, i.e., $C_{bulk}$ will not vary.

There have been suggestions on giant capacitance values for low-dimensional conductors arising from the long-range Coulomb potential [193]. An inspection of the charge control mechanism for $C_{lat}$ leads us to suggest that the negative thermodynamic density of states associated to the edge of the preserved 2DES may be responsible for the giant "sail" shape CE feature. $C_{lat}$ is an "unconventional" capacitor with the edges of the cathode and the preserved 2DES as its contacts. These edges can be considered a quasi one-dimensional electron system (1DES), the density of which can be varied by applying a bias voltage, as well as by addition of light-generated carriers. Coulombic interactions in a 1DES is generally stronger than the 2- and 3-D cases, and the exchange and correlation energies are expected to be more critical. Hence capacitance enhancements in a 1DES is more pronounced. In the case of the MSM-2DES device, it is feasible that in dark the edge 1DES density is below a

certain critical value, $n_{critical}^{1DES}$, (that can be different from the $n_{critical}$ for the 2DES). Under illumination, the 1DES density surpasses the critical value due to addition of the light-generated electrons. It is then depleted to levels below $n_{critical}^{1DES}$ by means of a bias voltage. This enforced transition could appear as the "sail" CE feature in the C-V under illumination. This proposal, however, requires further experimental verification with less uncertainty in the incident illumination conditions.

### 4.1.4   Local triggering of a MIT: Capacitance mapping

Further evidence in support for the hypothesis of Sec. 4.1.3 is attained through C-V measurement under a local excitation of the MSM-2DES by a coherent illumination. In order to exclusively probe the CE due to the lateral $C_{lat}$, a $50nm$ insulating SiN layer is grown on top of the AlGaAs layer. The contacts are then deposited on the SiN. The density of the 2DES in the QW is then reduced to an "insulating" phase due to surface states introduced by the SiN/AlGaAs interface. This is verified by examining the C-V characteristics of this device at dark, which is shown in Fig. 4.2(a). The C-V has an equilibrium capacitance of $C_{0V} = 5pF$ at no bias. At a threshold voltage of $V_{th} = 1V$, capacitance abruptly drops to and remains less than $200fF$. This behavior is similar to the MSM-2DES capacitor of Secs. 2.2.1 and 2.4. The transition of the 2DES underneath the cathode from a dense could of 2D electrons at equilibrium to a total depletion under adequate bias voltage accounts for the bi-state behavior in the C-V. Consequently, the unconventional parallel-plate capacitor that is comprised of the cathode and the 2DES as its plates, is varied from a finite value to zero. A band bending that is due to the SiN/AlGaAs interface states reduces the 2DES density to a level below $n_{critical}$; hence no CE feature is observed in dark.

A laser light with a spot size of $\sim 1\mu m$ at the wavelength of $780nm$ (optical density of $260W/mm^2$), and a variable location is then incident on the MSM-2DES device
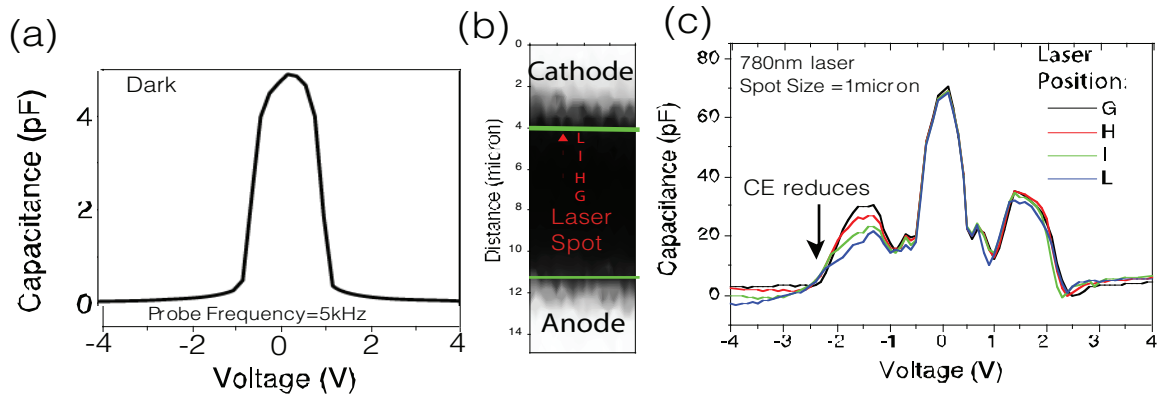
Figure 4.2: Capacitance mapping of the MSM-2DES capacitor by a location varying coherent illumination. [Data courtesy of Anna Persano]

with an overall top SiN layer. The C-V characteristics is measured at various location of the laser light on top of the contacts and across the gap between them. A "small" device with a $7\mu m$ contact separation was selected for this purpose. Figs. 4.2(b) and (c) indicate the incident illumination spots on the device and the associated C-V characteristics, respectively. The C-V under light was measured using the same LCRmeter and an optical scanning system while the photocapacitance vs. voltage was recorded as a function of the laser spot position on the sample, as indicated in Fig. 4.2(b). All photo-capacitance measurements were performed at room temperature. The C-V under light, shown in Fig. 4.2(c), exhibits significant differences with the dark, mainly in a larger $C_{0V}$ value of $80pF$, and existence of a capacitance enhancement of up to 70% at the threshold voltage, $V_{th}$. With the illumination present on the device, generated electron-hole pairs in the GaAs absorption region are separated by the vertically aligned internal electric field. The electrons are then drifted to the QW, while the holes are pushed deeper in the device. Consequently, the net density of the 2DES increases, which is observed as a larger $C_{0V}$ in the C-V. Noticeably, the equilibrium capacitance is about 8 times greater than the expected geometrical capacitance of the cathode-to-2DES of $\sim 10pF$. The underlying reason for this drastic change is

deferred to further investigation and is beyond the scope of this dissertation.

Importantly, at the bias voltage of $V_{th} = -1V$ in the C-V under light, a "sail" shape CE feature is observed, where the capacitance is $17pF$, and enhances to $30pF$ at $V_{CE} = -1.5V$, which is an enhancement of more than 70%. This peak appears in a post-threshold bias voltage, at which $C_{lat}$ is the dominant charge control mechanism and $C_{0V}$ has no effect. The light-to-dark capacitance ratio at the same bias voltage is $C_{light}/C_{dark} = 150$, showing an enlargement of more than two orders of magnitude. This suggests suitability of the SiN-capped MSM-2DES device for capacitive based photo-detection.

The wavelength of the incident illumination is selected to insure that absorption only occurs at the GaAs layer. With the movement of the laser spot toward cathode, the pre-threshold $C_{0V}$ capacitance does not show appreciable changes. This indicates that addition of the photo-generated electrons does not significantly change the equilibrium state of the system. When the laser spot is moved away from the anode, the observed "sail" peak at $V_{CE} = -1.5V$ decreases from $30pF$ for spot $G$ to $18pF$ at point $L$. Equivalently, as the region at which carriers are generated by light, is moved away from the reversely biased anode, the value of $C_{lat}$ reduces. This "unconventional" capacitor has the edge of the anode and the quasi 1DES edge of the existing two-dimensional system in the gap as contacts. It can be hypothesized that distancing the laser spot from the edge results into fewer carriers to add to the edge 1DES; hence the transition to levels above $n_{critical}^{1DES}$ could not happen, which is manifested in the C-V as a reduced peak value of the "sail" shape CE. Thus the quantum capacitance of $C_{lat}$ can only be activated when enough carriers are provided through light-generated electrons to force the transition from a metallic into an insulating system. Finally, the internal energies of the edge 1DES are manipulated by light-generated carriers by a local excitation. This features adds a spatial resolu-

tion for this class of capacitive-based photodetectors that operate on management of exchange and correlation energies of unconventional capacitors.

## 4.2  An MSM-2DHS capacitor for photo-detection

In this section a capacitive-based photodetection method is proposed that manipulates $U_{ex-corr}$ of an embedded 2DCS through introduction of light-generated carriers. This technique is demonstrated in a device with a planar MSM structure[93] that includes an additional embedded third plate consisting of a 2D hole system (2DHS). In dark, the C-V characteristic of this device shows behavior of a switchable capacitor. Under sufficient optical power, however, it exhibits a giant CE of more than 200% at critical bias voltages. This feature of CE is attributed to the negative $C_{ex-corr}$, and is triggered when addition of light-generated carries increases the density of the embedded 2DHS to above a certain critical threshold, at which contribution of $U_{ex-corr}$ becomes significant. Since the peak capacitance under light reaches values that are over two orders of magnitude greater than its dark amount, this unconventional MSM-2DHS device opens a new concept in realization of capacitance-based photodetectors.

### 4.2.1  MSM-2DHS fabrication

The device is comprised of two Schottky contacts, fabricated on the top surface, with an embedded 2DHS, as seen in the layer structure in Fig. 4.3(a). On a GaAs substrate, 200nm of GaAs buffer layer was grown by molecular beam epitaxy (MBE). A 118nm GaAs absorption layer and a consecutive 57nm $Al_{0.5}Ga_{0.5}As$ barrier layer were then grown to form a heterostructure on top of the Bragg reflector. Specifically, the thickness of the GaAs absorption layers was chosen to address the trade-off between quantum efficiency and speed of response, similar to that of MSM photodetectors [36, 77]. The selection of the AlGaAs layer thickness follows the design considera-

tions of modulation-doped field effect transistors [30]. A p-type $2.5 \times 10^{12} cm^{-2}$ Be delta-doping layer was introduced at 7nm distance from the GaAs/AlGaAs hetero-interface on the AlGaAs side. Schottky contacts were defined by optical lithography, Ti(10nm)/Au(90nm) metal deposition, and subsequent lift-off. An interdigitated pattern was fabricated on a $60 \times 40 \mu m^2$ active area on the top layer, as shown in the SEM image in Fig. 4.3(c). Additionally, control devices with identical layer structure
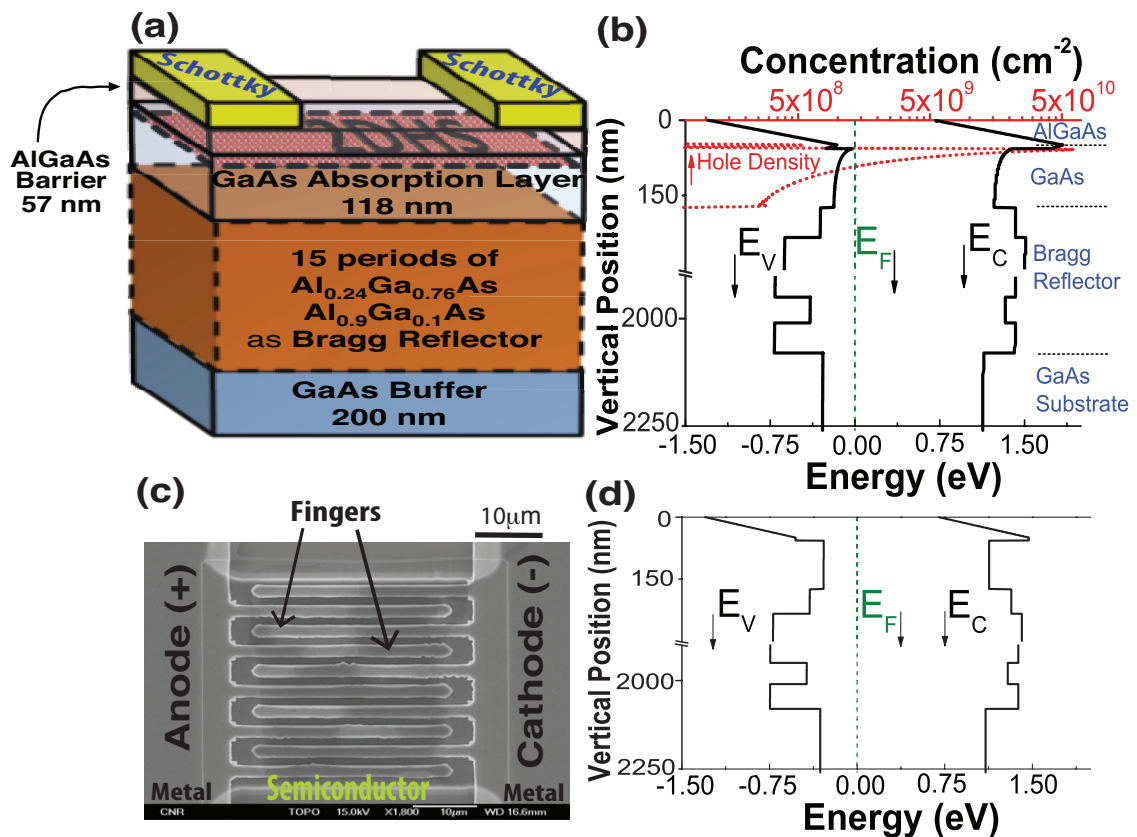


Figure 4.3: MSM-2DHS capacitor: a) Layer structure, b) Energy band diagram for the main device, c) Top view SEM image of the capacitor, and d)Energy band diagram for the "control" device.

were fabricated with the delta-doping level reduced to $1.0 \times 10^{12} cm^{-2}$.

The energy band diagrams and carrier (hole) densities were calculated by a Poisson-Schrödinger equation solver for this MSM-2D capacitor, which indicate formation of a triangular quantum well at the GaAs/AlGaAs interface, populated by a 2D sheet of holes, as shown in Fig. 4.3(b). For the control device, however, such 2D hole system does not exists, as it is inferred from the Fermi level location in Fig. 4.3(d).
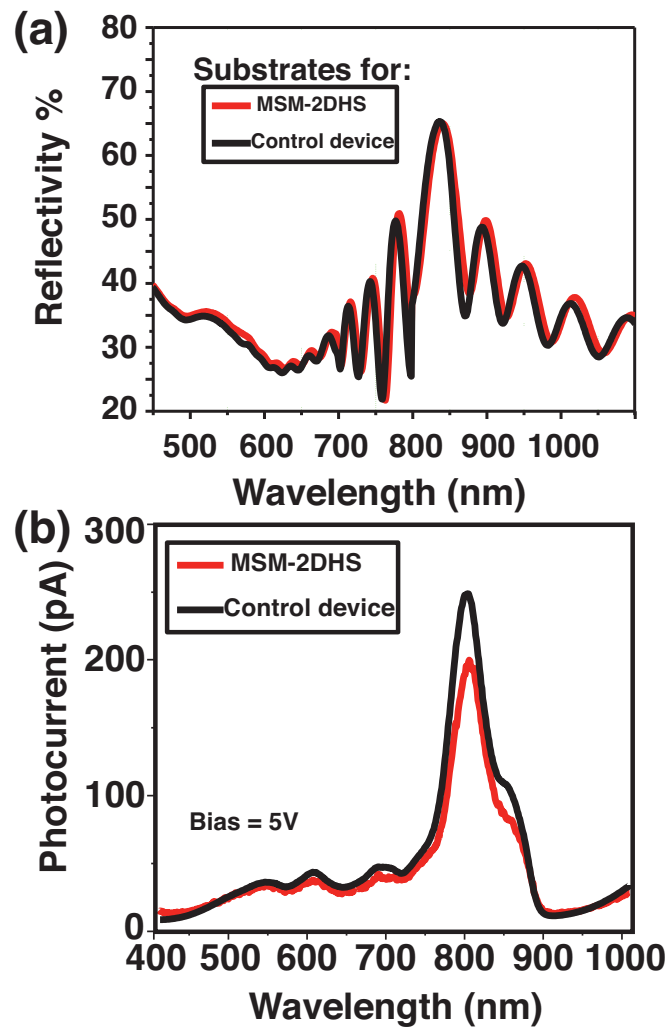


Figure 4.4: a) Reflectivity- and b) Current-Wavelength characteristics for MSM-2DHS and control devices.

The reflectivity vs. wavelength of an incident illumination on both of the devices is shown in Fig. 4.4(a), with highest value observed at $830nm$, which corresponds to the band gap of GaAs (1.42eV). This is mainly because of the incorporated Bragg reflector in the layer structure, to maximize the absorption of light in the GaAs absorption region. The majority of all other wavelengths pass through the layer structure, while the photons with $830nm$ of wavelength are reflected back to the GaAs region and also observed as a peak in the reflectivity curve. The maximized absorption can is verified in the current vs wavelength characteristics of Fig. 4.4. Both devices have a maximum photocurrent at a $5V$ bias and under $830nm$ of illumination. Importantly, MSM-2DHS and the control device have identical dependencies on the incident light. This is critical for fair comparison of the device capacitive performance under light, that will be discussed in Sec. 4.2.4.

### 4.2.2 I-V characteristics at dark

Figs. 4.5(a) and (b) show the current-voltage (I-V) characteristics of the MSM-2DHS and the control devices in dark and under various optical powers in a $3-353\mu W$ range of an incident $850nm$ laser light with a spot size of $20\mu m$, that covers the whole active area of the interdigitated structure. At dark both devices exhibit currents levels that are smaller than $10pA$, indicating the influence of Schottky contacts and a high quality GaAs/AlGaAs interface with limited surface states. The MSM-2DHS device has a larger dark current, compared to the control device. Under coherent illumination, the current level in both devices increases with applied bias voltages with an eventual saturation at $V_{bias} = 1.5V$ for MSM-2DHS and $V_{bias} = 1V$ for the control device. Notably, a shoulder appears in the I-V under light for the MSM-2DHS device at $V_{bias} \sim 0.75V$. An increase in the power of the incident laser light, also increases the current level in the devices. It changes from $100nA$ under $3\mu W$

of laser power to $3\mu A$ under $353\mu W$ pf the incident illumination. The current level at the saturation region for the MSM-2DHS device is equal or slightly less than the current for the control device under similar optical powers. Both devices exhibit very large light-dark current ratios of greater than 10000, and have a good functionality as conventional HMSM transport-based photodetectors.
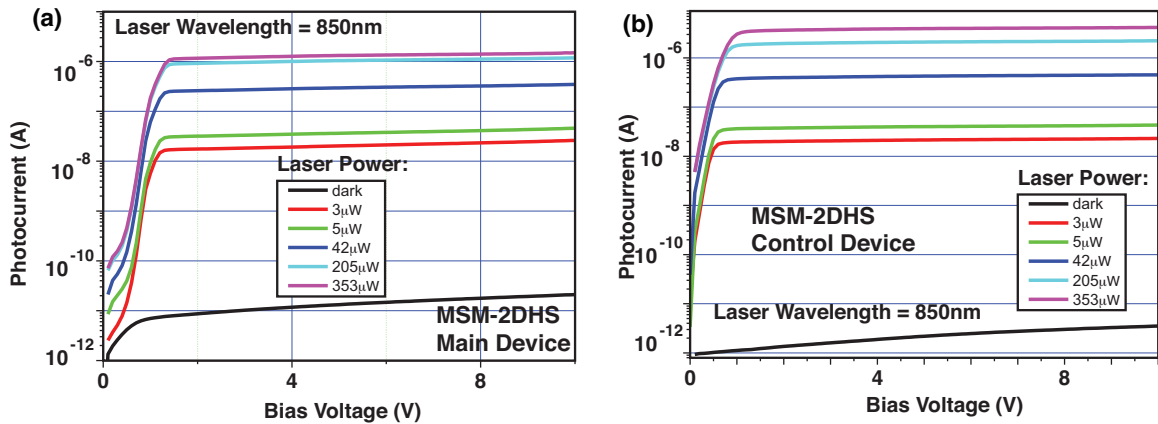


Figure 4.5: Current-Voltage characteristics under various incident 850nm laser power for a) MSM-2DHS and b) control devices.

### 4.2.3   C-V characteristics of MSM-2DHS capacitor in dark

C-V characteristics were obtained using an HP4284 LCRmeter with a $30mV$ ac excitation level at room temperature for measuring the parallel capacitance of the device under test. The dc bias voltage is applied between the two Schottky contacts, and since the measured current values remain less than 10pA, no significant heating affects the capacitive performance of the device, considering the rather large surface area. A bi-state behavior, as that of a switch-capacitor, is observed in the measured C-V for the MSM-2DHS capacitor under dark, shown in Fig. 4.6(a). This feature is similar to other reports [27, 35, 77, 166] on MSMs that were based on 2DES;

consequently it verifies the existence of 2DHS at the GaAs/AlGaAs interface.
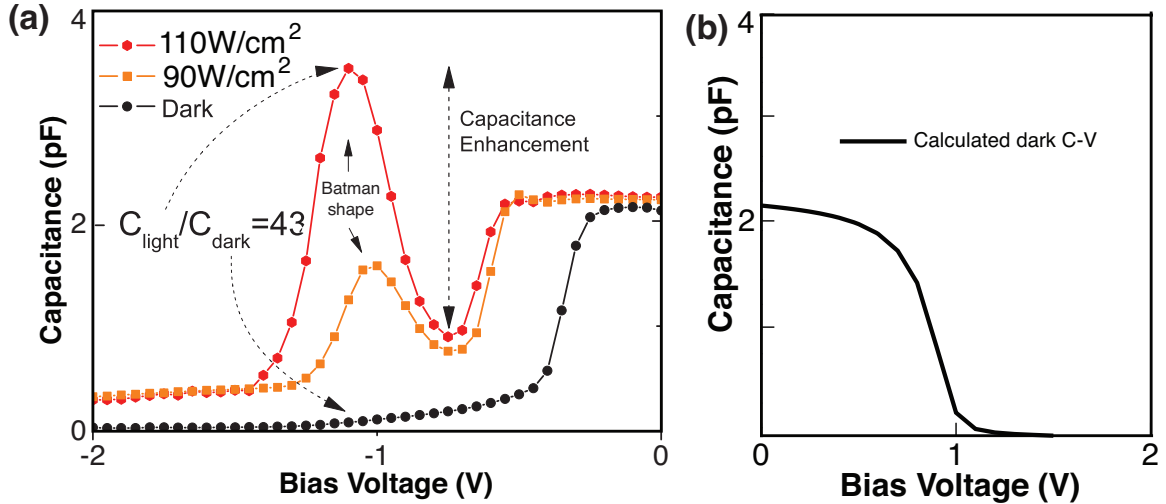


Figure 4.6: a) Capacitance-Voltage of MSM-2DHS in dark and under different optical powers at 10kHz of probe frequency, b) calculated dark C-V for the same device as in (a).

An MSM device with similar structure, but lacking the 2DHS, has a geometrical capacitance of $29.2fF$, calculated based on standard conformal mapping techniques [99]. This is in agreement with $31.4fF$ of the measured dark capacitance for the control device. Addition of 2DHS, remarkably, increases that capacitance, close to two orders of magnitude, to $2.36pF$, signifying the critical role of the 2DHS on the performance of the device. For planar MSMs with embedded 2DCS [35, 166], the pre-threshold capacitance may be modeled as series connection of capacitances of the cathode and the anode, connected by the 2D charge layer. If the charge density of the 2DCS is not large, the zero bias capacitance is $C_{0V} = C_{2DCS}/2$, where $C_{2DCS} = \epsilon A/d$ is the parallel plate capacitance between metal contacts of cathode (and anode) of area $A$, and $d$ is the distance between these contacts and the 2D. However, if 2D layer has sufficient charge density, the gas can rearrange itself to within a Debye

length in response to applied bias, shielding the electric field, and terminating the field lines. In this case $C_{0V} = C_{2DCS}$ as we have previously shown [27, 166]. In any case, application of bias depletes the charge on the (reverse biased) contact on which voltage drops; i.e., the second (unconventional) plate of charge disappears, and the device capacitance is determined by the very small (fringe) capacitance between this contact and the 2DCS. A tuning range, defined as maximum-to-minimum capacitance ratio, as large as 90 and a voltage sensitivity, $(dC/dV) \times (V/C)$, as high as 79 are observed, which are comparable with previous reports on performance of MSMs with 2DCS in dark[35, 77]. This single device thus is a switched capacitor without needing switching elements.

Fig. 4.6(b) shows the calculated dark capacitance of a device with similar structure as the MSM-2DHS capacitor. It is found by numerical solution of the drift-difussion and Poisson equations using Synopsys Sentaurus device simulation package. It matches the measured dark C-V of Fig. 4.6(a), in the pre-threshold capacitance value and the transition voltage.

### 4.2.4   C-V characteristics of MSM-2DHS capacitor under coherent illumination

The C-V for MSM-2DHS device, obtained at a 10kHz of probe frequency and under various optical powers of an 850nm laser exhibits, as indicated in Fig. 4.7(a), very large CE when its value reaches $\sim 1pF$. This light-triggered "Batman" shape, as highlighted in Fig. 4.6(a), is the distinctive anomalous feature reported in (dark) C-V [23, 24, 26, 167], and only appears here at high laser intensities and around a certain threshold voltage, $V_{critical}$, where a transition from a "high" to a "low" state occurs in the dark C-V. The pre-threshold characteristics of C-V do not change significantly with variations in the laser power, although a slight increase in threshold voltage-

moving from $0.4V$ in dark to $0.6V$ under $350\mu W$ laser light is observed. This is mainly due to an increase in the population of the 2DHS by light-generated carriers. The post-threshold behavior, however, exhibits significant differences compared to the one in dark. Distinctively, a shoulder in C-V appears under low power light, when the capacitor is biased around $V_{critical}$. With further increase in incident light intensity, capacitance reaches a peak value of $3.45pF$ at 1.1V of bias and under $350\mu W$ illumination, while the preceding valley capacitance is $0.76pF$ at $0.75V$ of bias. This is a 4.5:1 ratio corresponding to CE of 200%, which is much higher than previous, if any, reports. Furthermore, based on intended application of the device, enhancements of 40% is achieved when compared to 0-bias plateau capacitance of $2.1pF$. Also with the dark capacitance at $1.2V$ of bias, being $69.7fF$, the light-to-dark capacitance ratio of over 45 makes the MSM-2DHS an excellent candidate for capacitance-based photodetectors, pixels similar to charge coupled devices, and phototransistors. Finally, the enhancement occurs at probe frequency of $10kHz$, far larger than other observations of CE in devices with 2DCS [23, 24, 26, 167], giving MSM-2DHS practical applications. Furthermore, generation and storage of electron-hole pairs by light in a semiconductor device with a quantum well are suggested to function as a photonic memory cell [183]. Such an application may be possible in this MSM-2DHS photo capacitor with the changes of of capacitance serving as the required memory states.

As indicated in Fig. 4.7(c), the dark C-V of the control sample does not exhibit a plateau, which is consistent with the lack of 2DHS and its value equals the the co-planar geometric capacitance. Under illumination, however, the equilibrium capacitance changes from $43fF$ at dark to $1.2pF$ under $350\mu W$ of optical power, indicating the establishment of a 2DHS by optically generated holes. The general characteristics of C-V for control sample conform into that of the main device, with
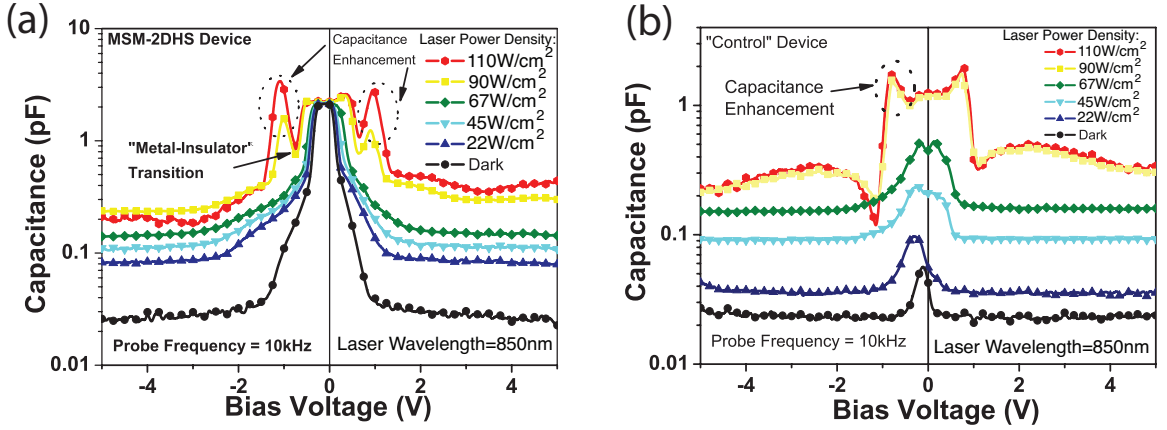
Figure 4.7: Capacitance-Voltage characteristics under various illumination intensities for a) MSM-2DHS capacitor, and b) "control" device.

increased intensity, and eventually exhibit CE feature at optical powers greater than $250\mu W$ and bias voltage of 0.8V. Incidentally, inclusion of the 15 periods of Bragg reflector with a reflection coefficient of close to unity and a bandwidth of 670nm for the 850nm laser light, confines the generation of electron-hole pairs inside the GaAs absorption layer. Additionally, the electric field due to the band bending in the absorption layer of the main device, as shown in Fig. 4.3(b), assists collection of the light-generated holes inside the quantum well by drifting them toward the 2DHS. The light-generated electrons, however, are moved by the electric field deeper into the device, and do not contribute to capacitance. Saturation of the pre-threshold capacitance at higher optical powers for both samples implies formation of a dense sheet of 2DHS serving as an unconventional contact.

Fig. 4.8 shows C-V at various probe frequencies ranging from $10kHz$ to $200kHz$ under a $350\mu W$ of incident 850nm illumination. The pre-threshold decrease in capacitance with an increase in frequency has previously been observed and attributed to fast capture and slow re-emission of charge carriers at GaAs/AlGaAs interface [118]. Furthermore, the CE feature is present in frequencies as high as $100kHz$, however, the
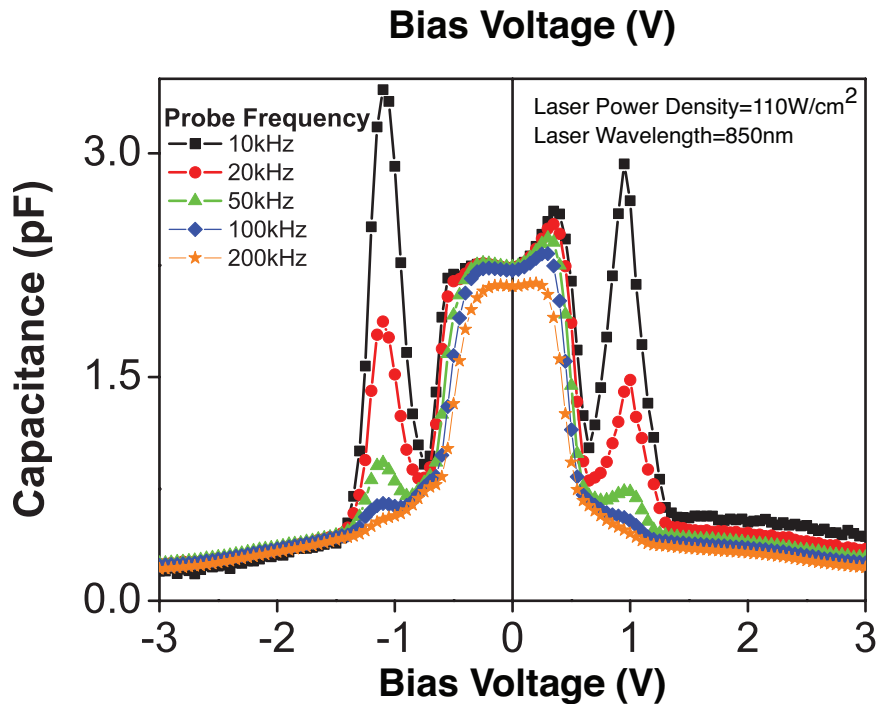
Figure 4.8: Capacitance-Voltage of MSM-2DHS capacitor under various probe frequencies.

amount of enhancement decreases with an increase in the probe frequency. This gives the MSM-2DHS more practical applications compared to other devices with 2DCS [26], in which the range of frequency for observations of CE is limited to under $10Hz$. The underlying physical explanation for the frequency dependence of CE, however, is deferred to further investigations.

### 4.2.5 Light-triggered metal-insulator transition in the MSM-2DHS capacitor

In an UC, where one or both contacts are replaced with a 2DCS, the control over the particle density, $p$, of the 2D system alters the ground state energy, $\mu$, of the

unconventional contact, as described in Chap. 3:

$$\mu = \frac{1}{{r_s}^2} - \frac{1.2}{r_s} - 0.38 - 0.17 r_s \ln(r_s), \qquad (4.1)$$

where $r_s = \sqrt{\frac{1}{p a_0{}^2}}$ is the normalized inter-particle distance in 2DHS and $a_0$ is the Bohr radius in the surrounding material. In Eq. 4.1, the first positive term is due to $U_{kin}$ and the remaining negative terms represent $U_{ex-corr}$. Since $r_s$ inside the 2DCS for $p > p_{critical}$ is comparable with the wavelength of individual particles, the wave functions overlap and the 2D system is in an interacting "metal" phase, while for a non-interacting "insulator" phase, $p$ is less than $p_{critical}$ and the overlap disappears, in which exchange forces become insignificant. Consequently, at densities around $p_{critical}$, an infinitesimal decrement of density, $dp$, causes the overall energy of the system to increase by $d\mu$ due to the removal of negatively contributing $U_{ex-corr}$. This energy is stored in the electric field among the contacts and an enhancement in capacitance is observed [23, 24]. This "metal-insulator" transition around $p_{critical}$ is attributed to negative compressibility, $d\mu/dp$, of a 2DES [25, 149, 168] and a 2DHS [25, 168], as detailed in Chap. 3.

For a 2DHS in GaAs, the critical transition density [25] is $p_{critical} = 5.5 \times 10^{10} cm^{-2}$. The charge control model [30] applied to the dark C-V, yields $p_{2DHS} = 5.1 \times 10^{10} cm^{-2}$ for the dark 2D hole concentration for MSM-2DHS, which is less than the $p_{critical}$. This shows that under dark the 2DHS is a non-interacting system hence no CE is observed. The solution to Poisson Equation was obtained using Synopsys Sentaurus$^{TM}$ device simulation package and calculated 2DHS density inside the device is reported in Fig. 4.9 for $0 - 1.5V$ bias range. Device capacitance is defined by the anode and the 2DHS underneath, when no bias is applied [27, 35, 77, 166]. Depletion of holes under anode, with an applied 1.5 V of the bias, as Fig. 4.9 shows, reduces the total capacitance to the small fringe capacitance between the anode and the pre-
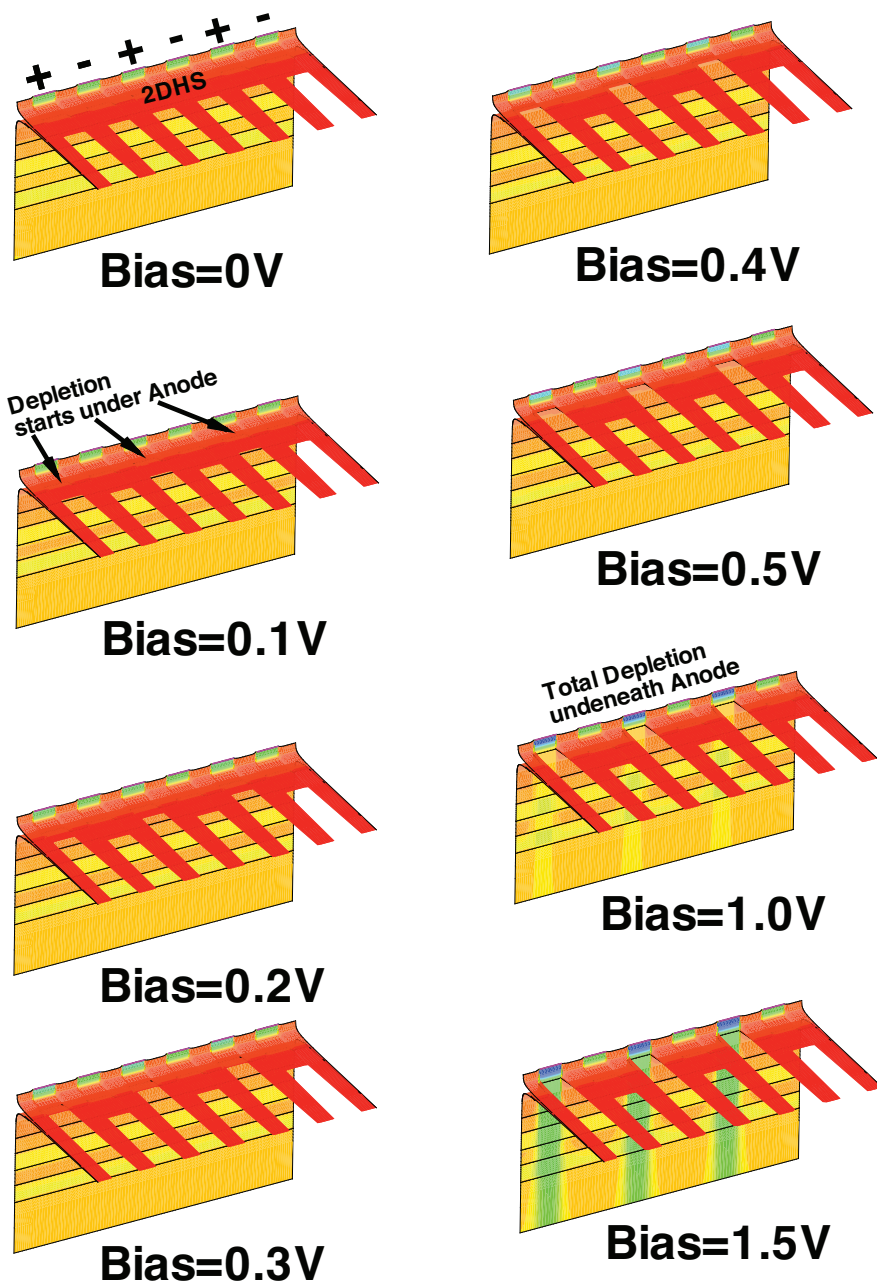
Figure 4.9: Calculation of hole density inside the MSM-2DHS capacitor under various bias voltages.

served 2DHS between the contacts, hence a transitions from a pre-threshold plateau to a post-threshold minimal capacitance is observed. Addition of optically generated holes raises 2DHS density to larger than $p_{critical}$ and the 2DHS becomes interacting, showing CE. Consequently the ground state energy of the 2DHS decreases due to significant exchange and correlation forces among particles [23]. Thus manipulation of the light-enhanced 2DHS density with bias voltage can account for the observed enhancement in C-V. Noticeably, comparison between the under-light C-V for the main and control samples reveals that, under the conditions of existence of a high-density 2DHS occurring at optical powers larger than $280\mu W$, both samples exhibit clear CE feature when the capacitance value reaches 1pF, which essentially corresponds to the same 2DHS critical density for a "metal-insulator" transition to be observed. Similar behavior has previously been observed for MSMs with 2DES [166] (Chap. 2) in which the dark electron density was above the critical value and CE was observed in dark as well as under illumination.

## 5. Conclusion and Future Research

### 5.1  Contributions of this dissertation

In this dissertation, significant electronic properties of two-dimensional fermion systems (2DFS) were presented, in both verification of theories of quantum mechanics and in engineering applications in electronics, photonics and optoelectronics. A class of unconventional devices was designed, fabricated, characterized, and analyzed. The main design feature of these unconventional devices is embedding of a 2DFS in the planar structure of an otherwise conventional metal-semiconductor-metal photodetectors. The capacitive performance of these unconventional MSM-2DFS devices were characterized by performing admittance spectroscopy measurements under various experimental conditions. Specifically, the C-V characteristics of these MSM-2DFS devices, exhibit large dependencies on applied bias voltage and/or the intensity of the incident illumination. Major features of this class of MSM-2DFS devices include:

1. A large pre-threshold "high" capacitance that is twice larger than previous reports [35, 81, 112]: This is due to the localized depletion of the 2DFS density by the applied bias, as discussed in Chap. 2. Semi-classical calculations of the MSM-2DES device indicates that the 2DFS depletion is only limited to the carriers underneath the reverse-bias contact, while it is preserved elsewhere in the device.

2. A minimal post-threshold "low" capacitance values: The MSM-2DFS capacitor can reach values that are less than the minimum conceivable geometrical capacitance of similar structures without embedded 2DFS. This feature can be applied to reduce transmission line cross-talk and clock skewing in integrated circuits.

3. Application as a voltage controlled capacitor: With the very large pre-threshold and the minimal post-threshold capacitance values, the MSM-2DFS reaches tuning range (TR) as high as 5000. This is the largest reported value, to the best of our knowledge. The TR is furthered increased by including the effects of the anomalous capacitance enhancement on the C-V.

4. A sharp transition between the two states of "high" and "low:" There exists a bi-state behavior in the C-V with voltage sensitivities as large as 400 at around the threshold voltage. Hence this single device can be applied as a switched capacitor without the need for additional switching elements.

5. An anomalous "Batman" shape capacitance enhancement (CE): At around the high-to-low transition, an enhancement in capacitance appears in C-V that can not be predicted by semi-classical models [30, 31]. This value surpasses the geometrical capacitance of contact-to-2DFS underneath. This anomalous feature is explained based on the negative compressibility of the 2DFS at certain critical density. Application of quantum theories of many-body physics indicate that the manipulation, release, and storage of the exchange and correlation energies of the 2DFS contact in the unconventional capacitor is the underlying reason for the "Batman" shape CE.

6. A giant CE in the capacitance under light: A CE feature appears in C-V when an adequately intense illumination is incident on the MSM-2DFS device. In the MSM-2DHS capacitor, such a feature is absent at dark. By introduction of light on the device electron-hole pairs are generated and the holes are collected at the 2DHS. This increases the hole density of the unconventional contact to above the critical value, at which the exchange-correlation energies become significant. They are then released and stored in the dielectric, which causes the giant CE

to appear in the C-V.

7. The light-to-dark capacitance ratio of over 40 at the peak of the giant CE: This indicates that the MSM-2DFS can be designed and utilized as a sensitive capacitance based photodetector. This method will not suffer from the traditional limitations of transport-based photodetectors, such as mediocre noise performance due to high dark currents.

Fig. 5.1 summarizes the contributions of this dissertation with an emphasis on the MSM-2DFS capacitor.
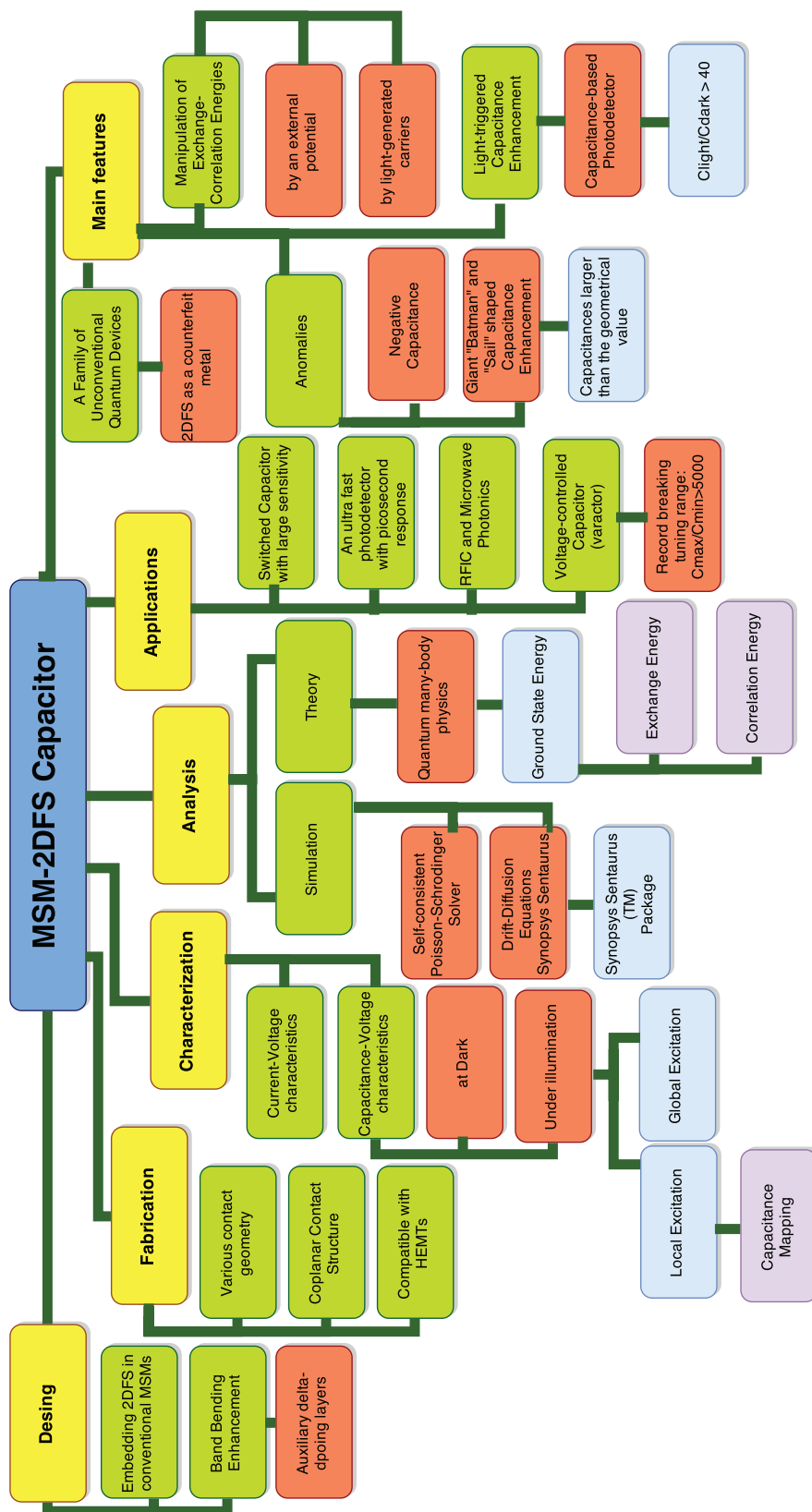
Figure 5.1: Summary of the contributions of this dissertation.

## 5.2 Outline of the future work

Based on the findings of this research, multiple paths may be taken to apply the theoretical framework of many-body physics to new engineering applications. These include making hybrid devices that include both the electron and hole systems. Specifically, it will be interesting to probe the mutual interactions of 2D planes on the overall device performance. Depending on the distance of placements of the 2DES and the 2DHS in a device, the strength and wave-function overlap of fermions could drastically change the Hamiltonian, and result into interesting features. This line of research faces challenges on discovery of the underlying physics, and it will be discussed in Sec. 5.3.

Another route for continuation of this research is on extending the theory of many-fermion systems to practical devices and functional materials that include a one-dimensional electron system (1DES). Carbon nanotubes and core-shell nanowires [7] are well-known instances of such systems. Theoretical studies on electron correlations in a 1DES dates back to 50 years ago, following the work of Luttinger [169]. Experimental observations and practical applications for many-body features of a 1DES, however, has remained scarce. The challenge is mainly on limitations in experimental procedures to isolate, extract and ascertain signatures of electron correlation in the overall device performance. This issue will further be discussed in Sec. 5.4.

## 5.3 A hybrid unconventional capacitor with bilayers of 2D electron and hole systems

The MSM-2DES and MSM-2DHS capacitors, that were described in Chaps. 2 and 3, function based on localized density control over the 2D charge layer. This was either with applying a bias voltage or through deposition of light-generated carriers. In this section, a new unconventional MSM device is introduced which includes bilayers of

two-dimensional electron (2DE) and two-dimensional hole (2DH) systems.

### 5.3.1 Layer structure for MSM-2DEHS capacitor with symmetric contact geometry

Fig. 5.2 indicates the layer structure (LS) for two variations of the MSM-2DEHS capacitors. The devices are comprised of a $200nm$ of $GaAs$ buffer layer, followed by a $60nm$ of $Al_{0.3}Ga_{0.7}As$ and $8nm$ of $InGaAs$, which forms a quantum well for holes. A C-doped p-type delta doping layer, with a concentration of $2.5 \times 10^{12} cm^{-2}$, is placed $5nm$ below the $AlGaAs/InGaAs$ interface. A $110nm$ thick $GaAs$ absorption region is then grown, followed by a $60nm$ barrier enhancer layer of $Al_{0.3}Ga_{0.7}As$. A $6 \times 10^{12} cm^{-2}$ Si-doped n-type delta doping (DD) layer provides the electrons for the 2DES in the triangular quantum well at the $GaAs/AlGaAs$ interface. This DD is located $5nm$ above the hetero-interface. The main distinction of the two LSs is in the placement of a Bragg reflector (BR) on top of the $GaAs$ buffer layer. The BR is comprised of 15 periods of $62nm$ of $AlAs$ and $73nm$ of $Al_{0.3}Ga_{0.7}As$, and is utilized to maximize the $830nm$ light absorption in the $GaAs$ absorption region. Schottky metal contacts were defined on the top $AlGaAs$ barrier layer by using standard optical lithography processing. The contact patterns and spacings are the same as that of TLM structure of Fig. 2.1.

### 5.3.2 Capacitance-voltage characteristics for symmetric MSM-2DEHS capacitor

The capacitance vs. voltage characteristics of the MSM-2DEHS devices exhibit numerous features, including a multiple plateau behavior, and giant local enhancement peaks at or around the transitions between plateaus. Interestingly, the multi-plateau behavior in the C-V only appears under coherent illumination, while the
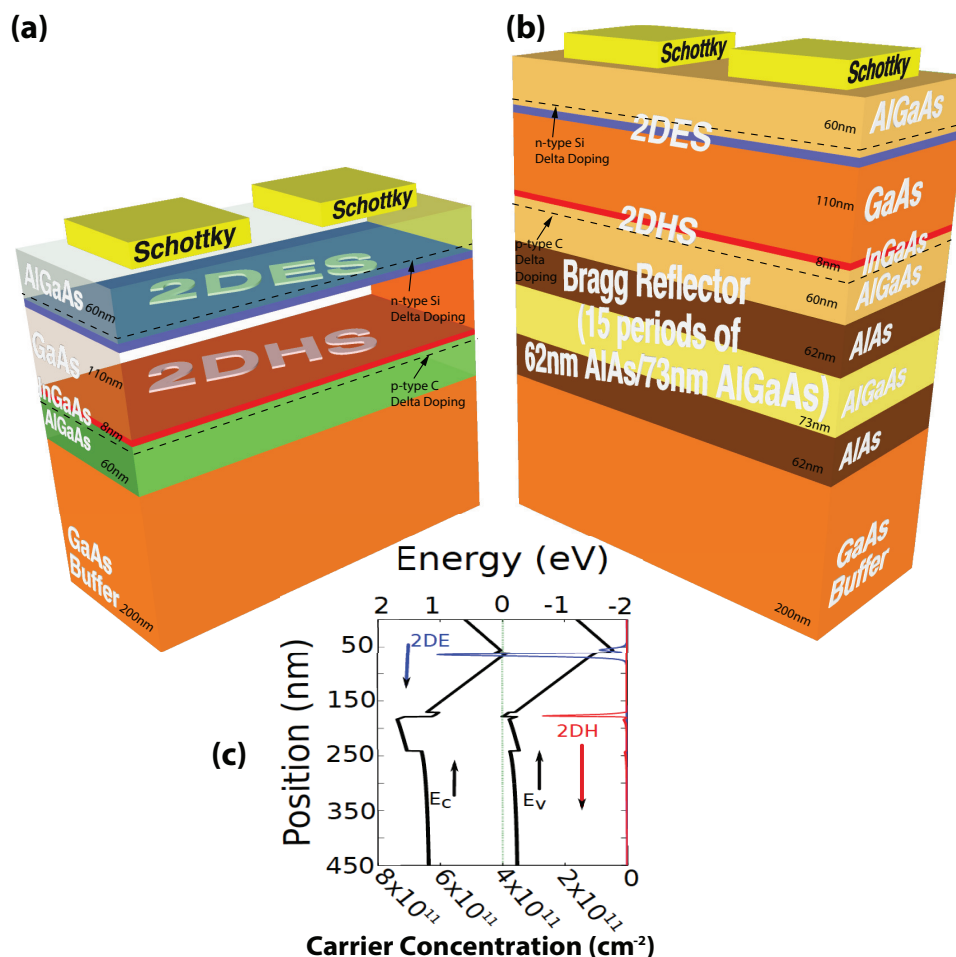
Figure 5.2: a) Non-Bragged, b) Bragged MSM-2DEHS capacitor layer structures, and c) Energy band diagram and carrier concentration in a direction normal to the interfaces.

peaks are present in the dark C-V and are further pronounced under light. Fig. 5.3(a) shows the capacitance of the symmetric MSM-2DEHS capacitor with Bragg reflector (Fig. 5.2(b)) in dark (left) and under white microscope light (right). Both cases exhibit large dependencies in the applied probe frequency of the LCRmeter. The general behavior of the C-V follows that of the MSM-2DES capacitor. The CE feature, however, becomes as large as 300%. Presence of white incoherent light, however, does not alter the capacitance significantly. Comparison of the quality factor for the same

device in dark and under light (Fig. 5.3(b)) shows an increase in Q when the light is incident. Hence, introduction of light enhances the capacitive performance of the device. Further insight into the C-V performance of the MSM-2DEH device can be reached by inspecting the capacitance mapping of the device.
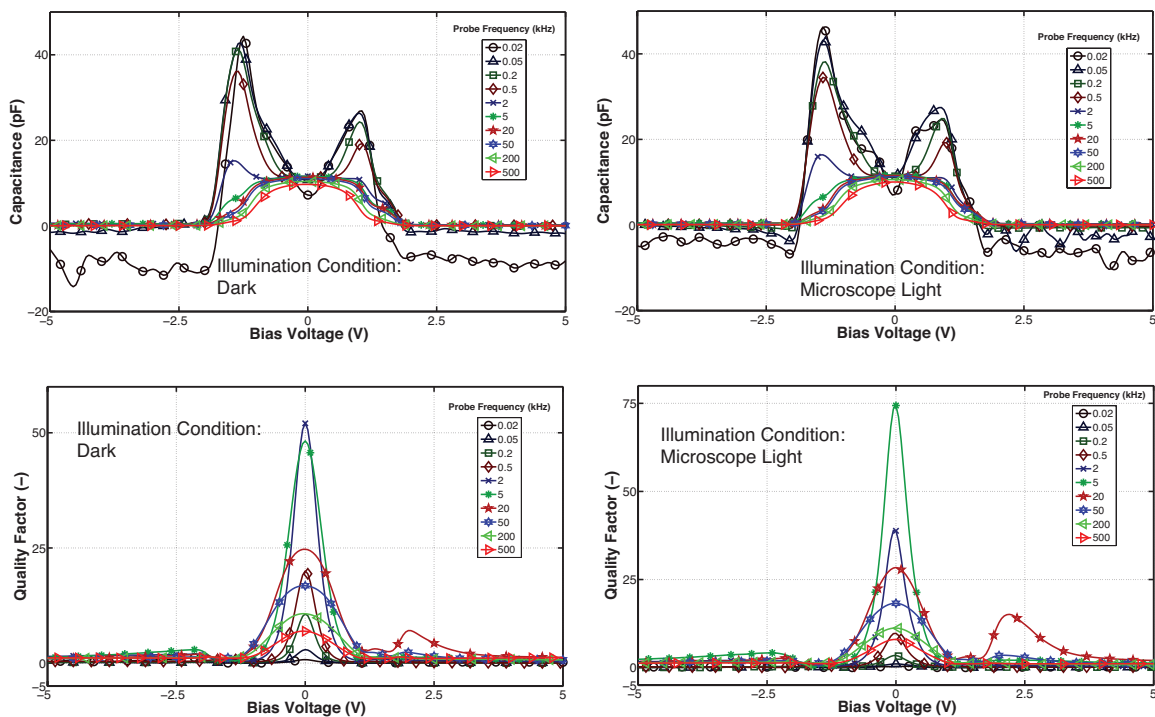


Figure 5.3: a) Capacitance and b) Quality factor vs. voltage for various probe frequencies, in dark and under light for the symmetric MSM-2DEHS capacitor.

Figs. 5.4 shows the capacitance of the same MSM-2DEHS capacitor with local coherent illumination. A laser light at $780nm$ and the spot size of $1\mu m$ is present on the device. The location of the laser spot is varied across the device from the cathode (C lines), to the Cathode Edge (L lines), the gap (G lines), the anode edge (R lines) and the Anode (A lines). At each location the C-V characteristics are measured, and indicated in Fig. 5.4. The C-V exhibits drastic changes under laser

light, when compared to dark. Mainly, the equilibrium capacitance value becomes twice larger under light. The multiple plateau behavior appears in the C-V and giant capacitance enhancement is observed at a threshold bias voltage of $1.8V$, between the plateaus. Interestingly, the capacitance value shows negligible variation on light location, when the spot is situated in the gap region. For other locations, however, the plateaus coincide on comparable values regardless of the location, while the CE features change significantly by laser position.
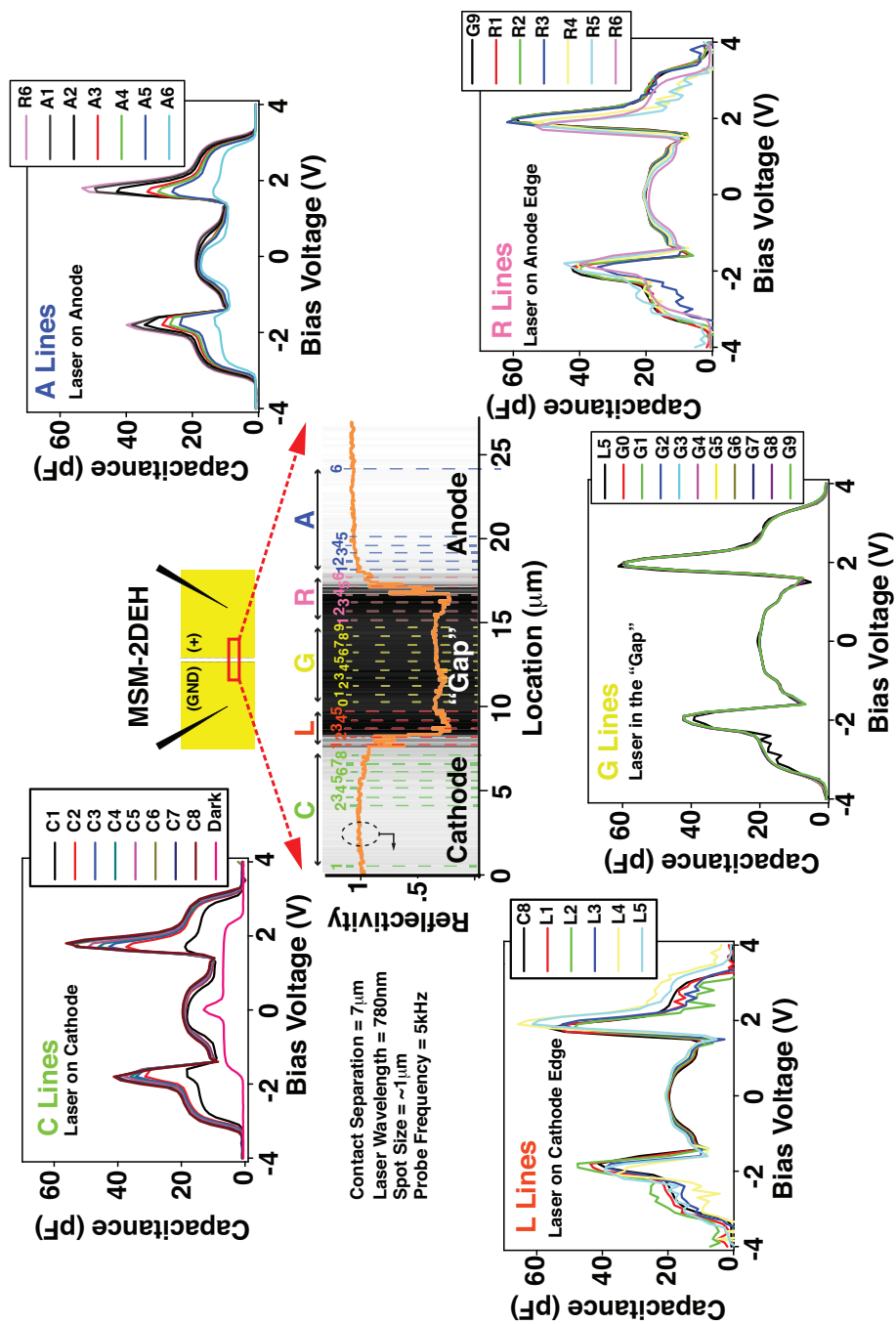
Figure 5.4: C-V mapping of the symmetric MSM-2DEHS capacitor with $7\mu m$ of gap separation C, L, G, R, and A lines correspond to the laser spot location over the cathode, on the left edge, top of the gap, on the right edge, and over the anode. [Data courtesy of Anna Persano]

Fig. 5.5 demonstrates the CE peak variations (measured at $V_{bias} = \pm 1.8V$,) on the location of laser spot across the device. On the regions far from both of the contacts, no light reaches the device, hence no electron-hole pair is generated and the capacitance is equal to the dark values. As the light moves toward the edges, the capacitance increases until it reaches its maximum when the laser spot is exactly on or in the vicinity of the edges. As the spot moves further into the gap and away from the edges, the capacitance value drops and remains rather constant.
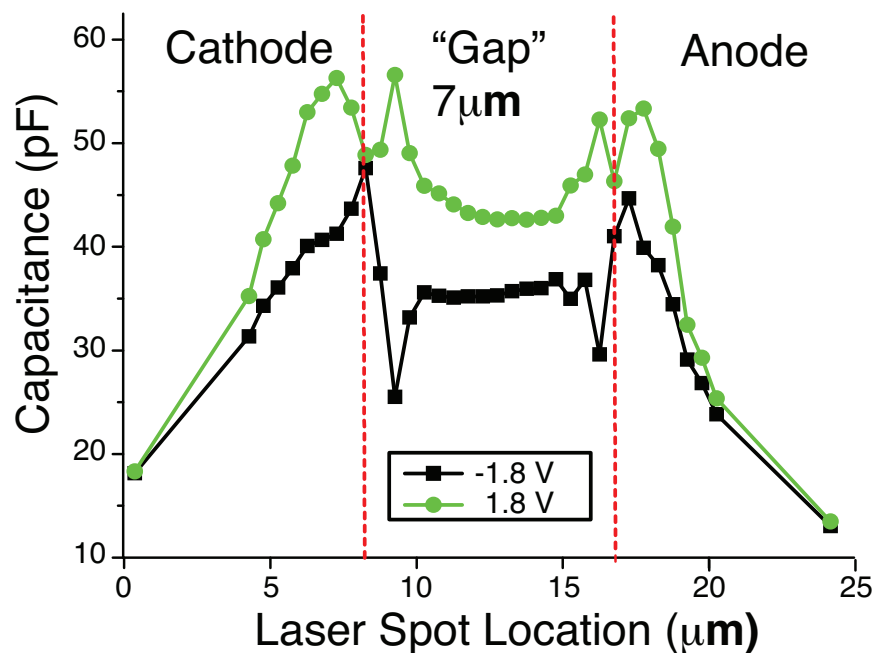


Figure 5.5: Changes in the peak capacitance of the CE feature with respect to the location of the laser spot. The capacitance is measured at $V_{bias} = \pm 1.8V$ for the symmetric MSM-2DEHS capacitor with $7\mu m$ of gap separation. [Data courtesy of Anna Persano]

The arias of the plateaus may be attributed to the localized depletion of 2DE and 2DH systems underneath cathode and anode, respectively. Additionally, by applying the theories of Chap. 3 to the MSM-2DEHS capacitor, the 2DE and 2DH systems

are to be preserved in the "gap" and underneath anode and cathode, respectively. This means that these localized depletion mechanisms are both simultaneous but in spatially separated regions underneath anode and cathode. Conversely, the 2DES layer has to shield the electric field from penetrating deeper into the device, hence classically, the 2DH layer could not "feel" the electric field. Such a complication can be explained based on the finite density of state of quantum 2D charge systems [22]. This description requires further verifications and is deferred to future investigations. Furthermore, any possible capacitive mechanism that arises from electrostatic coupling among the 2DE and 2DH layers is not account for.

### 5.3.3 A hybrid MSM-2DEHS capacitor with an asymmetric contact geometry

MSM-2DEHS devices with the same layer structure as Fig. 5.2 but with an asymmetric contact geometry have been applied for high-speed photodetection [107]. In this application, an interdigitated contact geometry similar to Fig. 4.3(c) was used. Fig. 5.6 shows the pattern for one period of the finger arrangement. One set of fingers is placed on the *AlGaAs* layer, while another set is deposited in an etched region to make direct contact to the 2DHS layer. The fingers are fabricated on a $25 \times 25\mu m^2$ mesa-isolated active region with their spacing and separation to be 2, and $8\mu m$, respectively.

The calculated electric field lines for the asymmetric MSM-2DEHS device are shown in Fig. 5.7 for various reverse and forward bias voltages, as well as in equilibrium. A vertically aligned electric field exists in the GaAs absorption region. This field assists the drift of the light generated electrons and holes toward the 2DE and 2DH channels, respectively. This causes a local disturbance in the charge density of the 2D charge reservoirs, which is transferred to the contacts through a charge density
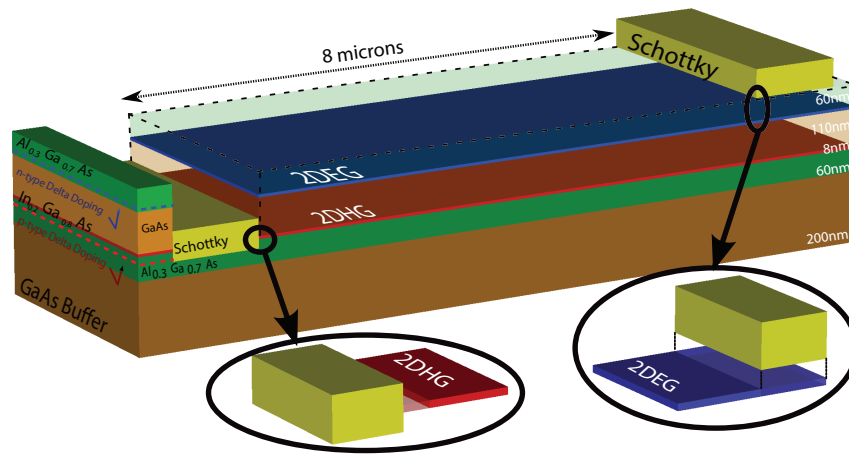
Figure 5.6: Layer structure for the asymmetric MSM-2DEH capacitor.

wave. This circumvents the individual charge transport for eventual collection at the contacts for an event of detection [107], hence it is much faster than conventional MSM photodetectors, as discussed in 1.5. A time-response of 10s of picosecond is reported for this asymmetric MSM-2DEHS photodetector [107], while conventional MSMs with similar size have response time in nanoseconds. Furthermore, the field lines in Fig. 5.7 indicate a large electric field at the edges and underneath the contacts, while the rest of the regions maintain the same field strength. This case is valid for both negative and positive biases, suggesting the possibility of a dielectric break-down at smaller bias voltages. Consequently, this photodetector will not be sensitive enough at larger bias voltages, since the break-down current would mask any current due to photo generation.
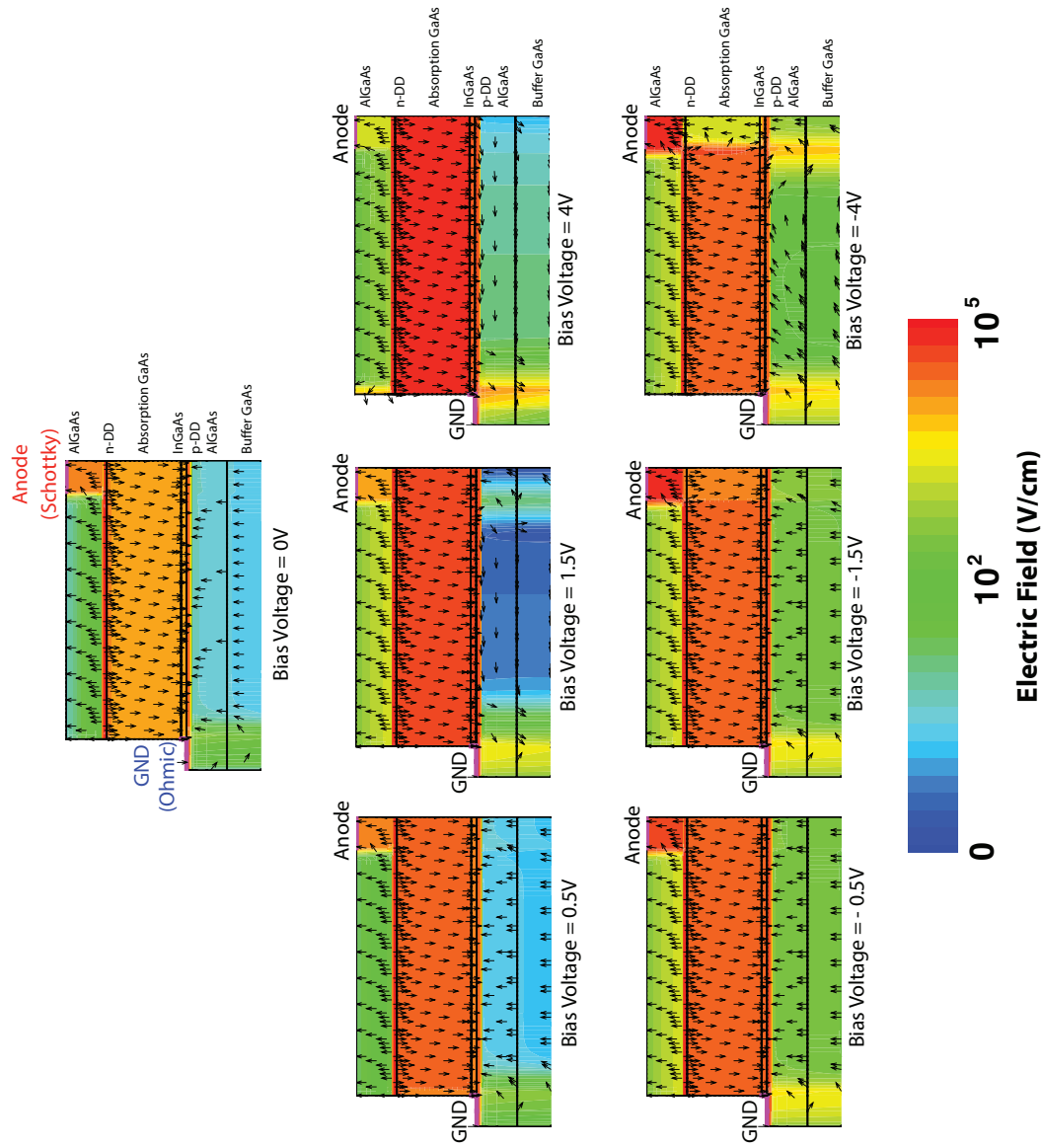
Figure 5.7: Calculated electric field distribution in MSM-2DEHS photodetector under various bias conditions.

### 5.3.4 Influence of the Bragg reflector on device performance

The inclusion of the Bragg reflector has major influence on the quantum efficiency of the MSM-2DEHS photodetector, mainly on quantum efficiency and wavelength selectivity. Fig. 5.8 shows the photocurrent spectrum for asymmetric interdigitate structures with gap and finger width of $2\mu m$, fabricated on layer structures with and without the Bragg reflector. The photocurrents are measured under various bias voltages in a $0 - 15V$ range. For both samples, a peak in current exists at $830nm$ of incident illumination. This corresponds to band gap of $GaAs$, which serves as the absorption region. While for the non-bragged sample the current levels remain less than $3nA$, the bragged device exhibit current levels as high as $30nA$. This indicates that a larger number of light generated carriers for the Bragged device, due to the existence of the reflector. Another major difference between the two samples is on the general behavior of the photocurrent spectrum. The bragged sample indicate less selectivity with respect to wavelength. At the $600 - 830nm$ wavelength range, this sample has an insignificant variation in current level, while for the non-bragged device, current can span close to two orders of magnitude.

### 5.4 One dimensional correlated electron systems: Luttinger liquid

Many electron systems in three and two dimensions are adequately treated through perturbation methods, as was discussed in Chap. 3. These many electron system are often called a Fermi liquid. There has been efforts in applying the properties of a Fermi liquid to a 1D electron system (1DES), mainly in the capacitive properties of such structures [8, 170]. It is shown that similar to a the case of the 2DES (Chap. 3), at a critical electron density of a 1DES, a singularity may appear in the quantum capacitance with very large negative values [170]. Furthermore, in a 1DES the corre-lations among electrons are much more significant, compared to bulk and 2D systems,
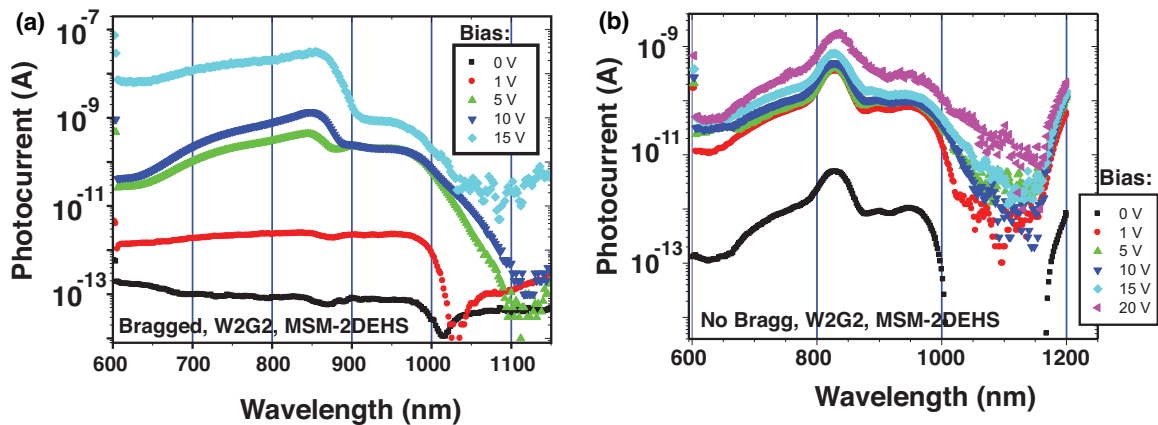
Figure 5.8: Photocurrent spectrum for a) Bragged and b) non-Bragged interdigitated MSM-2DEHS capacitor with finger and gap widths of $2\mu m$. [Data courtesy of Adriano Cola]

due to higher degrees of confinement. The electrons can either be moving to the left or right and any small or localized interaction can cause a collective response from the whole system. This is the condition of broken symmetry, in which the overall status of the system has to be reformulated [141]. For a 2DES, a broken symmetry occurs at very low densities of fermions, in which formation of a Wigner lattice is expected, that is due to the Coulombic interactions of electrons. Interestingly for a 1DES, the direction of movement for fermions is restricted to the left or right. Consequently, the particle density of the system becomes irrelevant with respect to the determination of the status of the system. Such a 1D many electron system is often called a Luttinger liquid, as he was the first person who successfully formulated these systems [169]. This behavior was observed in carbon nanotubes as a 1DES [171]. One-dimensional many electron systems can be a host of various peculiarities, among which are the spin-charge separation and 'bosonization' of fermions [172]. The explanation of these properties require development of the Luttinger liquid theory for the system of interest [141].

Among various material systems that incur a 1DES are carbon nanotubes [173],

electrons at the edges of a 2DES [174, 175], and epitaxial nanowires [176, 177]. Among these the latter can have more immediate applications as it is more compatible and can be integrated with current semiconductor technologies.

### 5.4.1 Core-Shell Nanowires

A core-shell nanowire (CSNW) is a quasi-one dimensional structure with a wide band gap material, such as AlGaAs, wrapping around a low band gap semiconductor, such as GaAs. Importantly, the reduced dimensionality can potentially save valuable space on the substrates. Furthermore, the vertical growth of the compound nanowires on Si substrates [178] has given these structures promising applications in integrated photonics and three-dimensional integrated circuits.

In CSNWs, a radial heterojunction can be formed and modulation doping may be introduced at any of the materials by using epitaxial growth methods [176]. In such structures, electrons and holes can be confined at the interface between the core and the shell, and depending on the geometry of the interface, it is possible to attain quasi 1- and 2-dimensional particle systems. Specifically, for the growth of GaAs/AlGaAs core-shell nanowires, a metalorganic chemical vapor deposition (MOCVD) with Au nanoparticles as catalyst is selected [177]. Application of such a method results in a hexagonal radial cross-section for the CSNWs. Fig. 5.9 shows the as-grown Core-Shell nanowires under different magnifications and view angles. The hexagonal cross-section can be seen in the top-view image of a single nanowire at highest magnification.

Fig. 5.10(a) shows a sketch of a GaAs/AlGaAs CSNW with an emphasis on the electron density at the hetero-interface. The calculated carrier density at the hexagonal cross-section, as shown in Fig. 5.10(b), indicates formation of two distinct class of many-electron systems at the interface. Specifically, six pillars of 1-dimensional
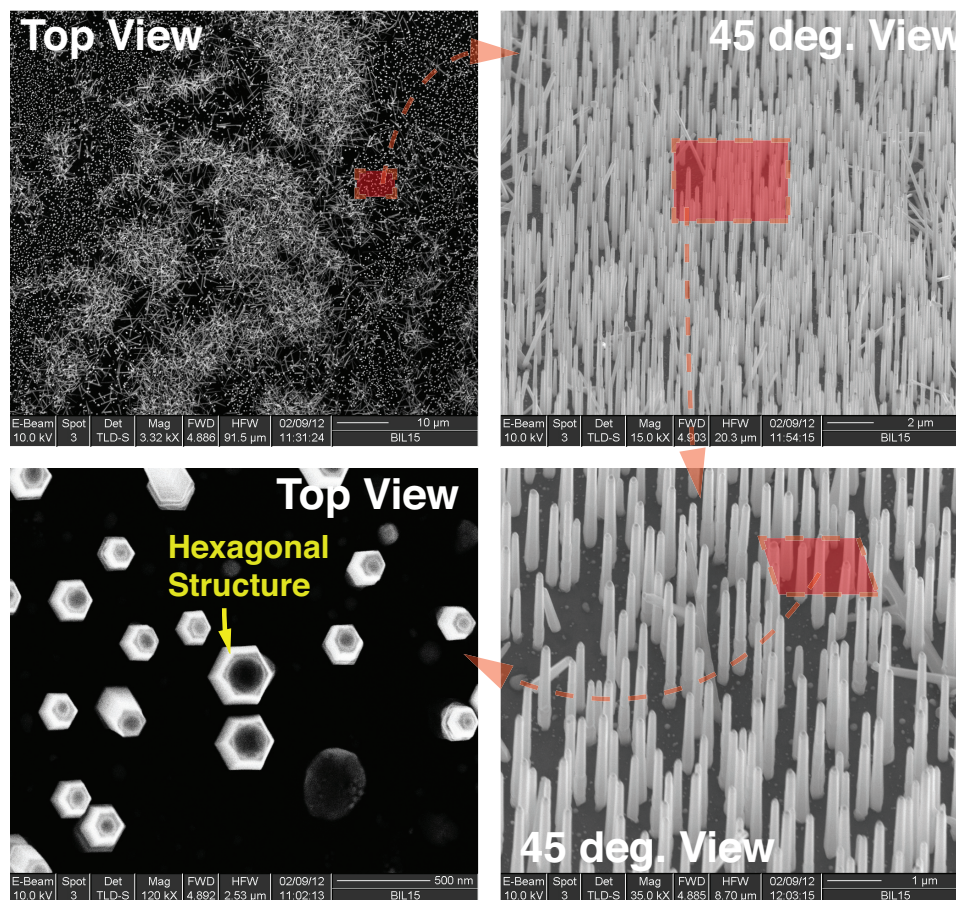
Figure 5.9: SEM image of as-grown GaAs/AlGaAs core-shell nanowires taken at different magnifications and view angles.

electron system are identified at the edges of the hexagonal interface, while six facets of 2DES with lower density exist at the faces. Consequently, this CSNW is a'super-host' for quantum many-electron systems with expectation of various exotic quantum features.

It is expected that the lower dimensionality in CSNW to have a significant influence on both optical and electrical properties of the structure. For instance, it is shown that a CSNW with a certain volume has a giant light absorption coefficient, which is much higher than the 2D thin film counterpart with similar volume [179]. Furthermore, CSNWs can function as a semiconductor laser without the need
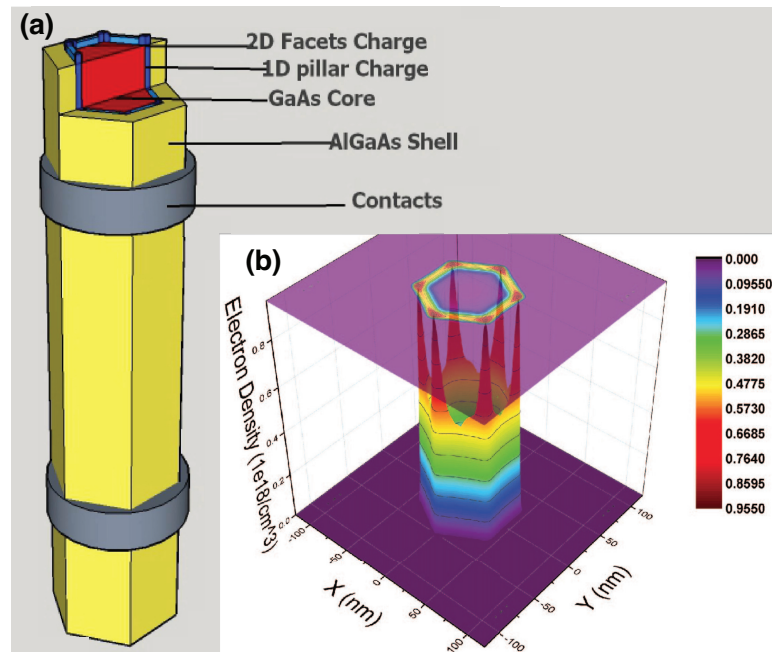
Figure 5.10: Photo Courtesy of Zhihuan Wang. A metal-semiconductor-metal core-shell nanowire. b) Electron density inside the core-shell nanowire.

for sophisticated mirror structures as in vertical cavity surface emitting lasers [179]. These remarkable features may be explained based on increased wave function overlap, increased exception oscillator strength, and strong dimensional dependency joint optical density if states [180]. Furthermore, both absorption and emission transition rates are strong functions of dimensionality.

Electrically it is important account for the electron correlations in order to determine the behavior of the structure. The significant values for exchange and correlation energies in 1DES, makes them an interesting candidate for probing the energy dynamics. The unique optical properties of CSNWs and their many-body properties makes these 1-dimensional structures an interesting candidate for further investigations. This, however, imposes various experimental challenges and theoretical considerations and are deferred to future investigations.

# Bibliography

[1] D. C. Johnson, "The puzzle of high temperature superconductivity in layered iron pnictides and chalcogenides," *Advance in Physics*, vol. 59, no. 6, pp. 803–1061, 2010.

[2] K. S. Novoselov, Z. Jiang, Y. Zhang, S. V. Morozov, H. L. Stormer, U. Zeitler, J. C. Maan, G. S. Boebinger, P. Kim, and A. K. Geim, "Room-temperature quantum hall effect in graphene," *Science*, vol. 315, pp. 1379–1379, March 2007.

[3] K. S. Novoselov, A. K. G. Geim, S. V. Morozov, D. Jiang, Y. Zhang, S. V. Dubonos, I. V. Grigorieva, and A. A. Firsov, "Electric field effect in atomically thin carbon films," *Science*, vol. 306, pp. 666–669, October 2004.

[4] D. A. Siegel, C. H. Park, C. Hwang, J. Deslippe, A. V. Fedorov, and S. G. L. A. Lanzara, "Many-body interactions in quasifreestanding graphene," *Proceeding of the National Academy of Sciences of the United States of America*, vol. 108, pp. 11365–11369, July 2011.

[5] M. R. Lukatskaya, O. Mashtalir, C. E. Ren, Y. Dall'Agnese, P. Rozier, P. L. Taberna, M. Naguib, P. Simon, M. W. Barsoum, and Y. Gogotsi, "Cation intercalation and high volumetric capacitance of two-dimensional titanium carbide," *Science*, vol. 341, pp. 1502–1505, September 2013.

[6] Q. H. Wang, K. Kalantar-zadeh, A. Kis, J. N. Coleman, and M. S. Strano, "Electronics and optoelectronics of two-dimensional transition metal dichalcogenides," *Nature Nanotechnology*, vol. 7, pp. 11699–712, November 2012.

[7] M. Law, J. Goldberger, and P. D. Yang, "Semiconductor nanowires and nanotubes," *Annual Review of Materials Research*, vol. 34, pp. 83–122, 2004.

[8] S. Ilani, L. A. K. Donev, M. Kindermann, and P. L. McEuen, "Measurement of the quantum capacitance of interacting electrons in carbon nanotubes," *Nature Physics*, vol. 2, pp. 687–691, 2006.

[9] K. Schmidt, U. Kunze, G. Medeiros-Ribeiro, J. Garcia, P. Wellmann, and P. Petro, "Field dependent carrier dynamics and charged excitons in inas self-assembled quantum dots," *Physica E*, vol. 2, pp. 627–631, July 1998.

[10] A. P. Alivisatos, "Semiconductor clusters, nanocrystals, and quantum dots," *Science*, vol. 271, pp. 933–937, February 1996.

[11] M. W. Cole, "Electronic surface states of liquid helium," *Review of Modern Physics*, vol. 46, July 1974.

[12] L. P. Gorkov and D. M. Chernikova, "Concerning the structure of a charged surface of liquid helium," *JETP Letters*, vol. 18, pp. 68–70, 1973.

[13] C. W. Bark, D. A. Felker, Y. Wang, Y. Zhang, H. W. Jang, C. M. Folkman, J. W. Park, S. H. Baek, H. Zhou, D. D. Fong, X. Q. Pan, E. Y. Tsymbal, M. S. Rzchowski, and C. B. Eom, "Tailoring a two-dimensional electron gas at the laalo3srtio3 (001) interface by epitaxial strain," *Proceeding of the National Academy of Sciences of the United States of America*, vol. 108, pp. 4720–4724, March 2011.

[14] H. Y. Hwang, Y. Iwasa, M. Kawasaki, B. Keimer, N. Nagaosa, and Y. Tokura, "Emergent phenomena at oxide interfaces," *Nature Materials*, vol. 11, pp. 103–113, January 2012.

[15] A. Ohtomo and H. Y. Hwang, "A high-mobility electron gas at the laalo3/srtio3 heterointerface," *Nature*, vol. 427, pp. 423–426, January 2004.

[16] S. Hiyamizu, T. Mimura, T. Fujii, and K. Nanb, "High mobility of twodimensional electrons at the gaas/nalgaas heterojunction interface," *Applied Physics Letters*, vol. 37, no. 9, p. 805, 1980.

[17] L. Esaki and R. Tsu, "Internal report rc 2418," tech. rep., IBM Research, March 1969.

[18] D. Kahng, "Electric field controlled semiconductor device," 1963. US Patent 3102230.

[19] G. Careri, U. Fasoli, and F. S. Gaeta, "Experimental behaviour of ionic structures in liquid helium - ii," *Nuovo Cimento*, vol. 15, pp. 774–783, March 1960.

[20] W. T. Sommer, "Liquid helium as a barrier to electrons," *Physical Review Letters*, vol. 12, pp. 271–273, March 1964.

[21] H. L. Stormer, D. C. Tsui, and A. C. Gossard, "The fractional quantum hall effect," *Review of Modern Physics*, vol. 71, pp. S298–S305, March 1999.

[22] S. Luryi, "Quantum capacitance devices," *Applied Physics Letters*, vol. 52, pp. 501–503, February 1988.

[23] B. Skinner and B. I. Shklovskii, "Anomalously large capacitance of a plane capacitor with a two-dimensional electron gas," *Physical Review B*, vol. 82, p. 155111, October 2010.

[24] M. S. Loth, B. Skinner, and B. I. Shklovskii, "Non-mean-field theory of anomalously large double layer capacitance," *Physical Review E*, vol. 82, p. 016107, July 2010.

[25] S. C. Dultz and H. Jiang, "Thermodynamic signature of a two-dimensional metal-insulator transition," *Physical Review Letters*, vol. 84, pp. 4689–4692, May 2000.

[26] L. Li, C. Richter, S. Paetel, T. Kopp, J. Mannhart, and R. C. Ashoori, "Very large capacitance enhancement in a two-dimensional electron system," *Science*, vol. 332, p. 825, May 2011.

[27] P. Dianat, R. W. Prusak, E. Galo, A. Cola, P. Persano, F. Quaranta, and B. Nabet, "A highly tunable heterostructure metal-semiconductor-metal capacitor utilizing embedded 2-dimensional charge," *Applied Physics Letters*, vol. 100, p. 153505, April 2012.

[28] R. Dingle, H. L. Stormer, A. C. Gossard, and W. Wiegmann, "Electron mobilities in modulation-doped semiconductor heterojunction superlattices," *Applied Physics Letters*, vol. 33, pp. 665–667, October 1978.

[29] M. Marso, M. Horstmann, H. Hardtdegen, P. Kordos, and H. Luth, "Electrical behaviour of the inp/ingaas based msm-2deg diode," *Solid-State Electronics*, vol. 41, pp. 25–31, January 1997.

[30] M. Shur, *GaAs devices and circuits*. New York, NY: Plenum Press, August 1987.

[31] T. J. Drummond, H. Morkoc, K. Lee, and M. Shur, "Model for modulation doped field effect transistors," *IEEE Electron Device Letters*, vol. EDL-3, no. 11, pp. 338–341, 1981.

[32] P. Dianat, R. W. Prusak, A. Persano, F. Quaranta, A. Cola, and B. Nabet, "Giant light-induced capacitance enhancements in an unconventional capacitor with two-dimensional hole gas," in *IEEE Photonics Conference (IPC)*, pp. 792–793, November 2012.

[33] P. Dianat, A. Persano, F. Quaranta, A. Cola, and B. Nabet, "Anomalous capacitance enhancement triggered by light," *IEEE Journal of Selected Topics in Quantum Electronics*, vol. 21, p. 3800605, July/August 2015.

[34] P. Dianat, R. W. Prusak, F. Quaranta, A. Cola, and B. Nabet, "A planar switchable capacitor with embedded two-dimensional electron system for higher integrations in vlsi and rfic," in *IEEE Compound Semiconductor Integrated Circuit Symposium*, (La Jolla, CA), pp. 1–4, October 2012.

[35] M. Horstmann, M. Marso, A. Fox, F. Ruders, M. Hollfelder, H. Hardtdegen, and P. Kordos, "Inp/ingaas photodetector based on a high electron mobility transistor layer structure: Its response at 1.3 micron wavelength," *Applied Physics Letters*, vol. 67, pp. 106–108, July 1995.

[36] X. Zhao, M. Currie, A. Cola, F. Quaranta, E. M. Gallo, J. E. Spanier, and B. Nabet, "Time response of two-dimensional gas-based vertical field metal–semiconductor–metal photodetectors," *IEEE Transactions on Electron Devices*, vol. 55, no. 7, pp. 1762–1770, 2008.

[37] M. E. Lazzouni and L. . Sham, "Theory of the electronic properties of delta-doped layers with dx centers in semiconductor heterostructures," *Physical Review B*, vol. 48, pp. 8948–8958, September 1993.

[38] J. Mannhart and D. G. Schlom, "Oxide interfaces—an opportunity for electronics," *Science*, vol. 327, pp. 1607–1611, March 2010.

[39] T. Ando, A. B. Fowler, and F. Stern, "Electronic properties of two-dimensional systems," *Review of Modern Physics*, vol. 54, no. 2, pp. 437–672, 1982.

[40] C. C. Grimes and G. Adams, "Plasmons in a sheet of electrons on liquid helium," *Surface Science*, vol. 58, pp. 292–294, 1976.

[41] R. S. Crandall and R. Williams, "Crystallization of electrons on the surface of liquid helium," *Physical Review A*, vol. 34, pp. 404–405, 1971.

[42] G. Deville, F. Gallet, D. Marty, J. Poitrenaud, A. Valdes, and F. I. B. Williams, "Detection of ordering of electrons on liquid helium," in *Ordering in Two Dimensions* (S. K. Sinha, ed.), pp. 309–312, Elsevier, 1980.

[43] M. Z. Hasan and C. L. Kane, "Colloquium: Topological insulators," *Review of Modern Physics*, vol. 82, pp. 3045–3067, October-December 2010.

[44] J. Moore, "Topological insulators: The next generation," *Nature Physics*, vol. 5, pp. 378–380, 2009.

[45] C. L. Kane and E. J. Mele, "Quantum spin hall effect in graphene," *Physical Review Letters*, vol. 95, November 2005.

[46] L. Fu, C. L. Kane, and E. J. Mele, "Topological insulators in three dimensions," *Physical Review Letters*, vol. 98, March 2007.

[47] D. Hsieh, Y. Xia, D. Qian, L. Wray, J. H. Dil, F. Meier, J. Osterwalder, L. Patthey, J. G. Checkelsky, N. P. Ong, A. V. Fedorov, H. Lin, A. Bansil, D. Grauer, Y. S. Hor, R. J. Cava, and M. Z. Hasan, "A tunable topological insulator in the spin helical dirac transport regime," *Nature*, vol. 460, pp. 1101–1105, August 2009.

[48] M. Naguib, V. N. Mochalin, M. W. Barsoum, and Y. Gogotsi, "25th anniversary article: Mxenes: A new family of two-dimensional materials," *Advanced Materials*, vol. 26, pp. 992–1005, February 2014.

[49] K. S. Novoselov and A. K. Geim, "The rise of graphene," *Nature Materials*, vol. 6, pp. 183–191, March 2007.

[50] K. S. Novoselov, A. K. Geim, S. V. Morozov, D. Jiang, M. I. Katsnelson, I. V. Grigorieva, S. V. Dubonos, and A. A. Firsov, "Two-dimensional gas of massless dirac fermions in graphene," *Nature*, vol. 438, pp. 197–200, November 2005.

[51] A. H. C. Neto, F. Guinea, N. M. R. Peres, K. S. Novoselov, and A. K. Geim, "The electronic properties of graphene," *Review of Modern Physics*, vol. 81, pp. 109–162, January/March 2009.

[52] L. Vicarelli, M. S. Vitiello, D. Coquillat, A. Lombardo, A. C. Ferrari, W. Knap, M. Polini, V. Pellegrini, and A. Tredicucci, "Graphene field-effect transistors as room-temperature terahertz detectors," *Nature Materials*, vol. 11, pp. 865–871, October 2012.

[53] D. Goldberg, Y. Bando, Y. Huang, T. Teraro, M. Mitome, C. C. Tang, and C. Y. Zhi, "Boron nitride nanotubes and nanosheets," *ACS Nano*, vol. 4, pp. 2979–2993, June 2010.

[54] E. A. Guggenheim, *Thermodynamics. An Advanced Treatment for Chemists and Physicists.* Amsterdam, The Netherlands: North Holland, seventh ed., 1985.

[55] R. C. Tolman, *The Principles of Statistical Mechanics.* Mineola, NY: Dover Publications, 1938.

[56] J. W. Gibbs, *Elementary Principles in Statistical Mechanics.* New York, NY: Charles Scribner's Sons, 1902.

[57] M. Razeghi and B. Nguyen, "Advances in mid-infrared detection and imaging: a key issues review," *Reports on Progress in Physics*, vol. 77, August 2014.

[58] J. Faist, F. Capasso, D. L. Sivco, C. Sirtori, A. L. Hutchinson, and A. Y. Cho, "Quantum cascade laser," *Science*, vol. 264, pp. 553–556, April 1994.

[59] L. E. Ballentine, "The statistical interpretation of quantum mechanics," *Review of Modern Physics*, vol. 42, pp. 358–381, October 1970.

[60] J. C. Slater, "A simplification of the hartee-fock method," *Physical Review*, vol. 81, pp. 385–390, 1951.

[61] M. Gell-Mann and K. A. Brueckner, "Correlation energy of an electron gas at high density," *Physical Review*, vol. 106, pp. 364–368, 1957.

[62] P. Nozieres and D. Pines, "Correlation energy of a free electron gas," *Physical Review*, vol. 111, p. 442, 1958.

[63] J. Lindhard and A. Winther, "Stopping power of electron gas and equipartition rule," *Matematisk-fysiske Meddelelser Det Kongelige Danske Videnskabernes Selskab*, vol. 34, no. 4, 1964.

[64] P. W. Anderson, *Basic Notions of Condensed Matter Physics.* Addison Wesley Publishing Company, 1984.

[65] Y. Zhu and S. Zhou, "An analytical expression for the dispersion relation of surface plasmons in a bounded and layered two-dimensional electron gas," *Journal of Physics C: Solid State Physics*, vol. 20, March 1987.

[66] J. Bardeen, "Surface states and rectification at a metal semi-conductor contact," *Physical Review*, vol. 71, pp. 717–727, May 1947.

[67] D. Geldart, A. Das, and G. Gumbs, "Plasmon dispersion relation for a disordered interacting quasi-two-dimensional electron gas," *Solid State Communications*, vol. 60, pp. 987–990, December 1986.

[68] S. Kawata and V. M. Shalaev, eds., *Nanophotonics with surface plasmons.* Amsterdam, The Netherlands: Elsevier, 1st ed., 2007.

[69] E. H. Hwang and S. D. Sarma, "Dielectric function, screening, and plasmons in two-dimensional graphene," *Physical Review B*, vol. 75, p. 205418, May 2007.

[70] T. Otsuji, H. Karasawa, T. Watanabe, T. Suemitsu, M. Suemitsu, E. Sano, W. Knap, and V. Ryzhii, "Emission of terahertz radiation from two-dimensional electron systems in semiconductor nano-heterostructures," *Comptes Rendus Physique*, vol. 11, no. 421-423, 2010.

[71] P. Penfield and R. P. Rafuse, *Varactor Applications.* Cambridge, MA: MIT Press, 1962.

[72] A. R. Brown and G. M. Rebeiz, "A varactor-tuned rf filter," *IEEE Transaction on Microwave Theory and Techniques*, vol. 48, pp. 1157–1160, July 2000.

[73] L. Athukorala and D. Budimir, "Compact second-order highly linear varactor-tuned dual-mode filters with constant bandwidth," *IEEE Transaction on Microwave Theory and Techniques*, vol. 59, pp. 2214–2220, September 2011.

[74] E. Hegazi and A. A. Abidi, "Varactor characteristics, oscillator tuning curves, and am-fm conversion," *IEEE Journal of Solid-state Circuits*, vol. 38, pp. 1033–1039, June 2003.

[75] J. Vukusic, T. Bryllert, T. A. Emadi, M. S. Sadeghi, and J. Stake, "A 0.2-w heterostructure barrier varactor frequency tripler at 113 ghz," *IEEE Electron Device Letters*, vol. 28, pp. 340–342, May 2007.

[76] M. P. J. Tiggelman, K. Reimann, F. V. Rijs, J. Schmitz, and R. J. E. Hueting, "On the trade-off between quality factor and tuning ratio in tunable high-frequency capacitors," *IEEE Transactions on Electron Devices*, vol. 56, pp. 2128 – 2136, September 2009.

[77] X. Zhao, A. Tersigni, F. Quaranta, E. Gallo, J. E. Spanier, and B. Nabet, "Optically modulated high-sensitivity heterostructure varactor," *IEEE Electron Device Letters*, vol. 27, pp. 710–712, September 2006.

[78] P. Kordos, M. Marso, A. Fox, M. Hollfelder, and H. Luth, ""n-ingaas schottky diode with channel current transport along 2deg channel," *Electronic Letters*, vol. 28, pp. 1689–1690, August 1992.

[79] S. M. Sze and K. K. Ng, *Physics of Semiconductor Devices*. Hoboken, NJ: John Wiley and Sons, Inc., 3 ed., 2006.

[80] B. Nabet, A. Cola, A. Cataldo, X. Chen, and F. Quaranta, "Photodetectors based on heterostructures for opto-electronic applications," *IEEE Transaction on Microwave Theory and Techniques*, vol. 51, pp. 2063–2072, October 2003.

[81] M. Marso, A. Fox, G. Heidelberger, P. Kordos, and H. Luth, "Comparison of algan/gan msm varactor diodes based on hfet and moshfet layer structures," *IEEE Electron Device Letters*, vol. 27, pp. 945–947, December 2006.

[82] C. Lee, W. Pang, S. J. Chen, D. Chi, H. Yu, and E. S. Kim, "Surface micro-machined, complementary-metal-oxide-semiconductor compatible tunable capacitor with 14:1 continuous tuning range," *Applied Physics Letters*, vol. 92, p. 044103, January 2008.

[83] J. Chen, J. Zou, C. Liu, J. E. Schutt-Aine, , and S. Kang, "Design and modeling of a micromachined high-q tunable capacitor with large tuning range and a vertical planar spiral inductor," *IEEE Transactions on Electron Devices*, vol. 50, pp. 730–739, March 2003.

[84] A. Anwar, B. Nabet, and J. Culp, "An electrically and optically gate-controlled schottky/2deg varactor," *IEEE Electron Device Letters*, vol. 21, pp. 473–475, October 2000.

[85] M. H. T. Dastjerdi, A. Sanz-Velasco, J. Vukusic, E. L. Kollberg, M. Sadeghi, and J. Stake, ""ingaas/inalas/alas heterostructure barrier varactors on silicon substrate," *IEEE Electron Device Letters*, vol. 32, pp. 140–142, February 2011.

[86] A. Reklaitisa, "Efficient heterostructure doped-barrier varactor diodes," *Journal of Applied Physics*, vol. 105, pp. 1–5, January 2009.

[87] W. Jaskolski, "Confined many-electron systems," *Physics Reports-Review section of Physics Letters*, vol. 271, pp. 1–66, June 1996.

[88] H. Seo, C. Hotta, and H. Fukuyama, "Toward systematic understanding of diversity of electronic properties in low-dimensional molecular solids," *Chemical Reviews*, vol. 104, pp. 5005–5036, November 2004.

[89] T. Kopp and J. Mannhart, "Calculation of the capacitances of conductors: Perspectives for the optimization of electronic devices," *Journal of Applied Physics*, vol. 106, p. 064504, September 2009.

[90] N. F. Mott and R. W. Gurney, *Electronic Processes in Ionic Crystals*. London: Oxford University Press, 1940.

[91] W. Schottky, "Vereinfachte und erweiterte theorie der randschicht-gleichrichter," *Zeits. f. Physik*, vol. 118, pp. 539–592, February 1942.

[92] S. K. Cheung and N. W. Cheung, "Extraction of schottky diode parameters from forward currentvoltage characteristics," *Applied Physics Letters*, vol. 49, no. 2, pp. 85–87, 1986.

[93] S. M. Sze, D. J. Coleman, and A. Loya, "Current transport in metal-semiconductor-metal (msm) structures," *Solid-State Electronics*, vol. 14, pp. 1209–1218, December 1971.

[94] M. Currie, P. Dianat, A. Persano, M. C. Martucci, F. Quaranta, A. Cola, and B. Nabet, "Performance enhancement of a gaas detector with a vertical field and an embedded thin low-temperature grown layer," *Sensors*, vol. 13, pp. 2475–2483, February 2013.

[95] B. Nabet, ed., *Photodetectors: materials, devices, applications*. Cambridge, UK: Woodhead Publishing, 2015.

[96] P. Dianat, *Photodetectors: materials, devices, applications*, ch. 33: Unconventional photo capacitor with giant light induced capacitance enhancement. Cambridge, UK: Woodhead Publishing, 2015.

[97] J. A. Harari, J. P. Vilcot, and D. J. Decoster, *Metal Semiconductor Metal Photodetectors. Wiley Encyclopedia of Electrical and Electronics Engineering*. John Wiley and Sons, Inc., 1999.

[98] O. Wada, H. Nobuhara, H. Hamaguchi, T. Mikawa, A. Tackeuchi, and T. Fujii, "Very high speed gainas metalsemiconductormetal photodiode incorporating an alinas/gainas graded superlattice," *Applied Physics Letters*, vol. 54, no. 1, pp. 16–17, 1989.

[99] Y. C. Lim and R. A. Moore, "Properties of alternately charged coplanar parallel strips by conformal mappings," *IEEE Transactions on Electron Devices*, vol. ED-15, pp. 173–180, March 1968.

[100] P. Chattopadhyay and B. Raychaudhuri, "Frequency dependence of forward capacitance-voltage characteristics of schottky barrier diodes," *Solid-State Electronics*, vol. 36, no. 4, pp. 605–610, 1993.

[101] J. W. Chen, D. K. Kim, and M. B. Das, "Transit time limited high frequency response characteristics of msm photodetectors," *IEEE Transactions on Electron Devices*, vol. 43, pp. 1839–1843, 1996.

[102] I. S. Ashour, H. E. Kadi, K. Sherif, J. P. Vilcot, and D. Decoster, "Cutoff frequency and responsivity limitation of alinas/gainas msm pd using a two dimensional bipolar physical model," *IEEE Electron Device Letters*, vol. 42, pp. 231–237, 1995.

[103] D. C. Look, "Molecular beam epitaxial gaas grown at low-temperatures," *Thin Solid Films*, vol. 231, pp. 61–73, August 1993.

[104] S. Y. Chou and M. Y. Liu, "Nanoscale tera-hertz metal-semiconductormetal photodetectors," *IEEE Journal of Quantum Electronics*, vol. 28, no. 10, pp. 2358–2368, 1992.

[105] X. Zhao, *Carrier transport in high-speed photodetectors based on two-dimensional-gas.* PhD thesis, Drexel University, 2006.

[106] A. A. Seddik, *Heterodimensional Schottky contacts to modulation-doped heterojunction with application to photodetection.* PhD thesis, Drexel University, 2001.

[107] B. Nabet, M. Currie, P. Dianat, F. Quaranta, and A. Cola, "High-speed high-sensitivity optoelectronic device with bilayer electron and hole charge plasma," *ACS Photonics*, vol. 1, no. 7, pp. 560–569, 2014.

[108] G. D. Mahan, *Many particle physics.* New York, NY: Kluwer Academic/Plenum Publishers, 3rd ed., 2000.

[109] F. Bloch, "Über die quantenmechanik der elektronen in kristallgittern," *Zeits. f. Physik*, vol. 52, no. 7-8, pp. 555–600, 1929.

[110] M. Marso, P. Kordos, A. Fox, H. Hardtdegen, R. Meyer, and H. Luth, "A novel ingaas schottky-2deg diode," in *Proceedings of 1993 IEEE 5th International Conference on Indium Phosphide and Related Materials (IPRM)*, pp. 397– 400, April 1993.

[111] M. Marso, M. Horstmann, F. Ruders, O. Hollricher, H. Hardtdegen, P. Kordos, and H. Luth, "A novel inp/ingaas photodetector based on a 2deg layer structure," in *Proceedings of 1994 IEEE 6th International Conference on Indium Phosphide and Related Materials (IPRM)*, pp. 512–515, March 1994.

[112] M. Marso, A. Fox, G. Heidelberger, J. Bernat, and H. Luth, "An algan/gan two-color photodetector based on an algan/gan/sic hemt layer structure," *physica status solidi (c)*, vol. 3, pp. 2261–2264, May 2006.

[113] G. Snider, "1d poisson solver."

[114] D. K. Schroder, *Semiconductor material and device characterization.* Hoboken, NJ: John Wiley and Sons, Inc., 2006.

[115] "http://www.ioffe.ru/sva/nsm/semicond/."

[116] P. Bhattacharya, *Semiconductor optoelectronic devices.* Upper Saddle River, NJ: Prentice-Hall Inc., 2 ed., 1997.

[117] Agilent Technologies, *Agilent Impedance Measurement Handbook: A guide to measurement technology and techniques*, 4th ed.

[118] M. Sakhaf and M. Schmeits, "Capacitance and conductance of semiconductor heterojunctions with continuous energy distribution of interface states," *Journal of Applied Physics*, vol. 80, p. 6839, December 1996.

[119] S. K. Chung, Y. Wu, K. L. Wang, N. H. Sheng, C. P. Lee, and D. L. Miller, "Interface states of modulation-doped algaas-gaas heterostructures," *IEEE Transactions on Electron Devices*, vol. 34, pp. 149–153, February 1987.

[120] D. Delagebeaudeuf and N. T. Ling, "Metal-(n)algaas-gaas two dimensional electron gas fet," *IEEE Transactions on Electron Devices*, vol. ED-29, p. 955, 1982.

[121] C. Hepburn, "http://britneyspears.ac/lasers.htm."

[122] A. Bansal, B. C. Paul, and K. Roy, "An analytical fringe capacitance model for interconnects using conformal mapping," *IEEE Transactions on Computer-aided Design of Integrated Circuits and Systems*, vol. 25, pp. 2765–2774, December 2006.

[123] E. S. Krichevskii and O. S. Protopopov, "Nomographs for finding the capacitance of coplanar-plate capacitors," *Measurement Techniques*, vol. 29, no. 5, pp. 437–439, 1986.

[124] S. C. Wong, G. Y. Lee, and D. J. Ma, "Modeling of interconnect capacitance, delay, and crosstalk in vlsi," *IEEE Transaction on Semiconductor Manufacturing*, vol. 13, pp. 108–111, February 2000.

[125] F. A. Ghavanini, P. Enoksson, S. Bengtsson, and P. Lundgren, "Vertically aligned carbon based varactors," *Journal of Applied Physics*, vol. 110, p. 021101, July 2011.

[126] C. F. Kurth and G. S. Moschytz, "Nodal analysis of switched capacitor networks," *IEEE Transaction on Circuits and Systems*, vol. 26, pp. 93–105, February 1979.

[127] R. Gregorian, K. W. Martin, and G. C. Temes, "Switched-capacitor circuit design," *Proceedings of IEEE*, vol. 71, pp. 941–966, August 1983.

[128] S. Roy, N. Mahmoud, and M. H. Chowdhury, "Delay and clock skew variation due to coupling capacitance and inductance," in *IEEE International Symposium on Circuits and Systems*, pp. 621–624, May 2007.

[129] S. Salahuddin and S. Datta, "Use of negative capacitance to provide voltage amplification for low power nanoscale devices," *Nano Letters*, vol. 2, pp. 405–410, October 2008.

[130] J. Bisquert, "A variable series resistance mechanism to explain the negative capacitance observed in impedance spectroscopy measurements of nanostructured solar cells," *Physical Chemistry Chemical Physics*, vol. 10, pp. 4679–4685, January 2011.

[131] V. V. Zhirnov and R. K. Cavin, "Negative capacitance to the rescue?," *Nature Nanotechnology*, vol. 3, pp. 77–78, February 2008.

[132] J. Wang, B. Wang, and H. Guo, "Quantum inductance and negative electrochemical capacitance at finite frequency in a two-plate quantum capacitor," *Physical Review B*, vol. 75, p. 155336, April 2007.

[133] A. G. U. Perera, W. Z. Shen, M. Ershov, H. C. Liu, M. Buchanan, and W. J. Schaff, "Negative capacitance of gaas homojunction far-infrared detectors," *Applied Physics Letters*, vol. 74, pp. 3167–3169, May 1999.

[134] L. E. Byrum, G. Ariyawansa, R. C. Jayasinghe, N. Dietz, A. G. U. Perera, S. G. Matsik, I. T. Ferguson, A. Bezinger, and H. C. Liu, "Negative capacitance in gan/algan heterojunction dual-band detectors," *Journal of Applied Physics*, vol. 106, p. 053701, September 2009.

[135] A. I. Khan, D. Bhowmik, P. Yu, S. J. Kim, X. Pan, R. Ramesh, and S. Salahuddin, "Experimental evidence of ferroelectric negative capacitance in nanoscale heterostructures," *Applied Physics Letters*, vol. 99, p. 113501, September 2011.

[136] J. Shulman, Y. Y. Xue, S. Tsui, F. Chen, and C. W. Chu, "General mechanism for negative capacitance phenomena," *Physical Review B*, vol. 80, p. 134202, October 2009.

[137] S. Yang, K. Choi, and K. Weller, "Dc boosting effect of active bias circuits and its optimization for class-ab ingap-gaas hbt power amplifiers," *IEEE Trans Microw. Theory Tech*, vol. 52, pp. 1455–1463, May 2004.

[138] L. E. Larson, "Microwave device and circuit challenges for next generation wireless applications," in *IEEE Topical Conference on Wireless Communication Technology*, pp. 74–77, October 2003.

[139] J. Valdmanis, G. A. Mourou, and C. W. Gabel, "Subpicosecond electrical sampling," *IEEE Journal of Quantum Electronics*, vol. 19, pp. 664–667, April 1983.

[140] A. L. Fetter and J. D. Walecka, *Quantum theory of many-particle systems*. New York, NY: McGraw-Hill Book Company, 1971.

[141] G. Giuliani and G. Vignale, *Quantum Theory of the Electron Liquid*. Cambridge, UK: Cambridge University Press, 2005.

[142] B. Tanatar and D. M. Ceperley, "Ground state of the two-dimensional electron gas," *Physical Review B*, vol. 39, pp. 5005–5016, March 1989.

[143] N. Iwamoto, "Ground-state-energy theorem and the virial theorem of a many-particle system in d dimensions," *Physical Review A*, vol. 30, pp. 2597–2601, November 1984.

[144] E. Wigner, "On the interaction of electrons in metals," *Physical Review*, vol. 46, pp. 1002–1011, December 1934.

[145] J. W. J. Carr and A. A. Maradudin, "Ground-state energy of a high-density electron gas," *Physical Review*, vol. 133, January 1964.

[146] A. L. Fetter, "Electrodynamics and thermodynamics of a classical electron surface layer," *Physical Review B*, vol. 10, pp. 3739–3745, November 1974.

[147] G. Y. Hu and R. F. OConnell, "Generalization of the lindhard dielectric function to include fluctuation effects," *Physical Review B*, vol. 40, pp. 3600–3604, August 1989.

[148] P. Vashishta and K. S. Singwi, "Electron correlations at metallic densities. v," *Physical Review B*, vol. 6, no. 875, p. 4883, 1972.

[149] J. P. Eisenstein, L. N. Pfeiffer, and K. W. West, "Compressibility of the two-dimensional electron gas: Measurements of the zero-field exchange energy and fractional quantum hall gap," *Physical Review B*, vol. 50, pp. 1760–1778, July 1994.

[150] J. P. Eisenstein, L. N. Pfeiffer, and K. W. West, "Negative compressibility of two-dimensional electron and quasiparticle gases," *Physical Review Letters*, vol. 68, pp. 674–677, February 1992.

[151] H. Yukawa, "On the interaction of elementary particles," *Progress of Theoretical Physics Supplements*, vol. 17, no. 48, 1935.

[152] F. Rapisarda and G. Senatore, "Diffusion monte carlo study of electrons in two-dimensional layers," *Australian Journal of Physics*, vol. 49, no. 1, pp. 161–182, 1996.

[153] C. Attaccalite, S. Moroni, P. Gori-Giorgi, and G. B. Bachelet, "Correlation energy and spin polarization in the 2d electron gas," *Physical Review Letters*, vol. 88, p. 256601, June 2002.

[154] P. J. Burke, I. B. Spielman, J. P. Eisenstein, L. N. Pfeiffer, and K. W. West, "High frequency conductivity of the high-mobility two-dimensional electron gas," *Applied Physics Letters*, vol. 76, pp. 745–747, February 2000.

[155] C. Bulutay and M. Tomak, "Dielectric properties of the quasi-two-dimensional electron liquid in heterojunctions," *Physical Review B*, vol. 54, pp. 14643–14651, November 1996.

[156] F. Stern and W. E. Howard, "Properties of semiconductor surface inversion layers in the electric quantum limit," *Physical Review*, vol. 163, pp. 816–835, November 1967.

[157] F. Stern, "Polarizability of a two-dimensional electron gas," *Physical Review Letters*, vol. 18, pp. 546–548, April 1967.

[158] F. Stern, "Electron exchange energy in si inversion layers," *Physical Review Letters*, vol. 30, pp. 278–280, February 1973.

[159] S. Thiel, G. Hammerl, A. Schmehl, C. W. Schneider, and J. Mannhart, "Tunable quasi-two-dimensional electron gases in oxide heterostructures," *Science*, vol. 313, p. 1942, September 2006.

[160] M. Macucci and K. Hess, "Corrections to the capacitance between two electrodes due to the presence of quantum confined system," *VLSI Design*, vol. 6, no. 1-4, pp. 345–349, 1998.

[161] Y. Tang, H. Zheng, F. Yang, P. Tan, and Y. Li, "Capacitance-voltage characteristic as a trace of the exciton evolvement from spatially direct to indirect in quantum wells," *Semiconductor Science and Technology*, vol. 16, pp. 822–825, August 2001.

[162] Y. Tang, H. Zheng, F. Yang, P. Tan, C. Li, and Y. Li, "Electrical manifestation of the quantum-confined stark effect by quantum capacitance response in an optically excited quantum well," *Physical Review B*, vol. 63, p. 113305, February 2001.

[163] R. C. Ashoori, H. L. Stormer, J. S. Weiner, L. N. Pfeiffer, S. Pearton, K. W. Baldwin, and K. W. West, "Single-electron capacitance spectroscopy of discrete quantum levels," *Physical Review Letters*, vol. 68, pp. 3088–3091, May 1992.

[164] M. Buttiker, H. Thomas, and A. Pretre, "Mesoscopic capacitors," *Physics Letters A*, vol. 180, pp. 364–369, September 1993.

[165] J. Gabelli, G. Feve, J. M. Berroir, B. Placais, A. Cavanna, B. Etienne, Y. Jin, and D. C. Glattli, "Violation of kirchhoff's laws for a coherent rc circuit," *Science*, vol. 313, pp. 499–502, July 2006.

[166] P. Dianat, R. W. Prusak, A. Persano, F. Quaranta, A. Cola, and B. Nabet, "An unconventional hybrid variable capacitor with a 2-d electron gas," *IEEE Transactions on Electron Devices*, vol. 61, pp. 445–451, February 2014.

[167] A. L. Efros, "Negative density of states: Screening, einstein relation, and negative diffusion," *Physical Review B*, vol. 78, p. 155130, October 2008.

[168] G. Allison, E. A. Galaktionov, A. K. Savchenco, S. S. Safonov, M. M. Fogler, M. Y. Simmons, and D. A. Ritchie, "Thermodynamic density of states of two-dimensional gaas systems near the apparent metal-insulator transition," *Physical Review Letters*, vol. 96, p. 216407, 2006.

[169] J. M. Luttinger, "An exactly soluble model of a many-fermion system," *Journal of Mathematical Physics*, vol. 4, pp. 1154–1162, 1963.

[170] L. Latessa, A. Pecchia, and A. D. Carlo, "Negative quantum capacitance of gated carbon nanotubes," *Physical Review B*, vol. 72, July 2005.

[171] M. Bockrath, D. H. Cobden, J. Lu, A. G. Rinzler, R. E. Smalley, L. Balents, and P. L. McEuen, "Luttinger-liquid behaviour in carbon nanotubes," *Nature*, vol. 397, pp. 598–691, 1999.

[172] V. V. Deshpande, M. Bockrath, L. I. Glazman, and A. Yacoby, "Electron liquids and solids in one dimension," *Nature*, vol. 464, pp. 209–216, 2010.

[173] M. F. L. D. Volder, S. H. Tawfick, R. H. Baughman, and A. J. Hart, "Carbon nanotubes: Present and future commercial applications," *Science*, vol. 339, pp. 535–539, February 2013.

[174] S. Luryi and F. Capasso, "Resonant tunneling of twodimensional electrons through a quantum wire: A negative transconductance device," *Applied Physics Letters*, vol. 47, pp. 1347–1349, October 1985.

[175] H. L. Stormer, K. W. Baldwin, L. N. Pfeiffer, and K. W. West, "Gaas fieldeffect transistor with an atomically precise ultrashort gate," *Applied Physics Letters*, vol. 59, pp. 1111–1113, June 1991.

[176] L. J. Lauhon, M. S. Gudiksen, D. Wang, and C. M. Lieber, "Epitaxial core-shell and core-multishell nanowire heterostructures," *Nature*, vol. 420, pp. 57–61, November 2002.

[177] M. Fickenscher, T. Shi, H. H. Jackson, L. M. Smith, J. M. Yarrison-Rice, C. Zheng, P. Miller, J. Etheridge, B. M. Wong, Q. Gao, S. Deshpande, H. H. Tan, and C. Jagadish, "Optical, structural, and numerical investigations of gaas/algaas coremultishell nanowire quantum well tubes," *Nano Letters*, vol. 13, p. 10161022, 2013.

[178] S. Ihn, J. Song, and Y. Kim, "Growth of gaas nanowires on si substrates using a molecular beam epitaxy," *IEEE Transaction on Nanotechnology*, vol. 6, no. 3, pp. 384–389, 2007.

[179] M. Currie, Z. Wang, P. Dianat, P. Prete, I. Miccoli, N. Lovergine, and B. Nabet, "Large light emission enhancement in gaas/algaas coreshell nanowires," in *International Conference on One-Dimensional Nano Materials*, (Annecy, France), 2013.

[180] Z. Wang, M. Currie, P. Dianat, G. Konica, P. Prete, N. Lovergine, and B. Nabet, "On dimensional dependence of interaction of light and nano structures," in *Frontiers in Optics*, no. FTh3C.1, (Orlando, FL), October 2013.

[181] M. Y. Simmons, A. R. Hamilton, M. Pepper, E. H. Linfield, P. D. Rose, D. A. Ritchie, A. K. Savchenko, and T. G. Griffiths, "Metal-insulator transition at b = 0 in a dilute two dimensional gaas-algaas hole gas," *Physical Review Letters*, vol. 80, pp. 1292–1295, February 1998.

[182] C. D. Wang, C. Y. Zhu, G. Y. Zhang, J. Shen, , and L. Li, "Accurate electrical characterization of forward ac behavior of real semiconductor diode: Giant negative capacitance and nonlinear interfacial layer," *IEEE Transactions on Electron Devices*, vol. 20, pp. 1145–1148, April 2003.

[183] S. Zimmermann, A. Wixforth, J. P. Kotthaus, W. Wegscheider, and M. Bichler, "A semiconductor-based photonic memory cell," *Science*, vol. 283, pp. 1292–1295, February 1999.

[184] C. J. Forst, C. R. Ashman, K. Schwarz, and P. E. Blochl, "The interface between silicon and a high-k oxide," *Nature*, vol. 427, pp. 53–56, January 2004.

[185] B. I. Lundqvist, "Single-particle spectrum of the degenerate electron gas: I. the structure of the spectral weight function," *Physik der kondensierten Materie*, vol. 7, pp. 117–123, March 1968.

[186] M. Naghed and I. Wolff, "Equivalent capacitances of coplanar waveguide discontinuities and interdigitated capacitors using a three-dimensional finite difference method," *IEEE Transaction of Microwave Theory and Techniques*, vol. 38, pp. 1808–1815, December 1990.

[187] S. S. Safonov, S. H. Roshko, A. K. Savchenko, A. G. Pogosov, and Z. D. Kvon, "Metallic and insulating behavior of the two-dimensional electron gas on a vicinal surface of si mosfet's," *Physical Review Letters*, vol. 86, pp. 272–275, January 2001.

[188] V. Y. Butko and P. W. Adams, "Quantummetallicity in a two-dimensional insulator," *Nature*, vol. 409, pp. 161–164, January 2001.

[189] M. P. Sarachik and S. V. Kravchenko, "Novel phenomena in dilute electron systems in two dimensions," *Proceeding of the National Academy of Sciences of the United States of America*, vol. 96, pp. 5900–5902, May 1999.

[190] D. A. Knyazev, O. E. Omelyanovskii, V. M. Pudalov, and I. S. Burmistrov, "Metal-insulator transition in two dimensions: Experimental test of the two-parameter scaling," *Physical Review Letters*, vol. 100, p. 046405, February 2008.

[191] A. Punnoose and A. M. Finkelstein, "Metal-insulator transition in disordered two-dimensional electron systems," *Science*, vol. 310, pp. 289–291, October 2005.

[192] N. Manyala, J. F. DiTusa, G. Aeppli, and A. P. Ramirez, "Doping a semiconductor to create an unconventional metal," *Nature*, vol. 454, pp. 976–980, August 2008.

[193] B. Korenblum and E. I. Rashba, "Classical properties of low-dimensional conductors: Giant capacitance and non-ohmic potential drop," *Physical Review Letters*, vol. 89, p. 096803, August 2002.

# Appendices

# Appendix A. Current-Voltage characteristics for "Unconventional" MSMs

Here the Current-Voltage (I-V) characteristics for the MSM-2DES capacitor are presented. The device layer structure is as indicated in Fig. 2.1 and described in Chap. 2. Specifically, the I-V characteristics are compared when geometrical aspects of the metal contact pads, such as size, shape, and separation distance, are varied.
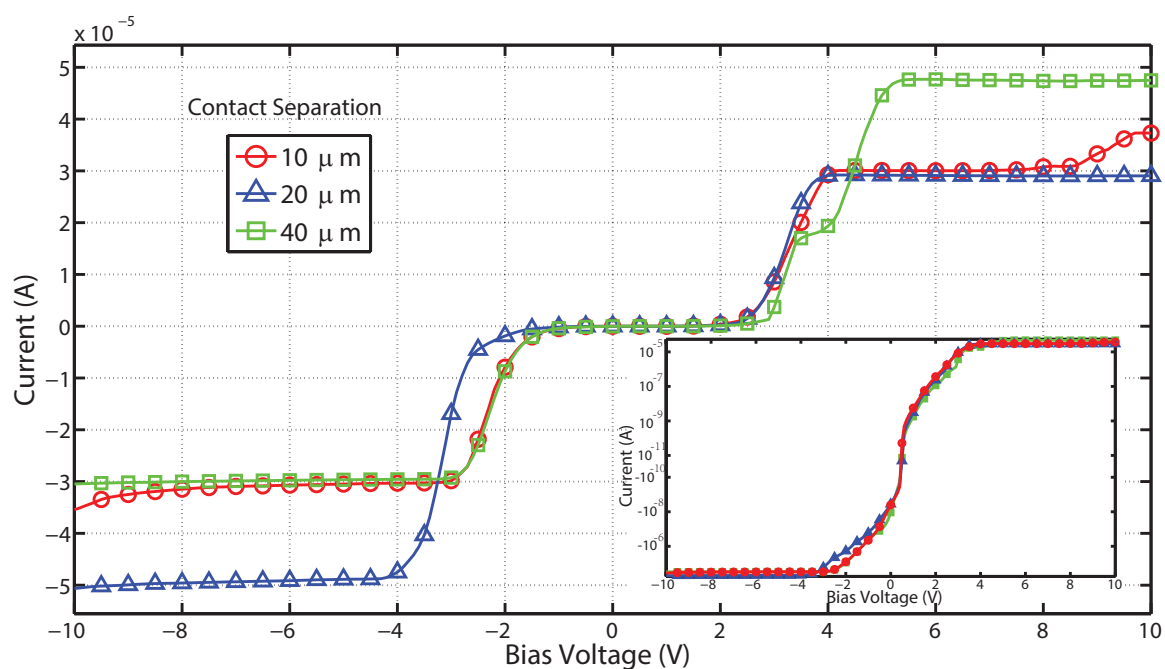
## A.1   Effect of variations in contact separation



Figure A.1: Current-Voltage characteristics for various contact separations on MSM-2DES device.

## A.2 Effect of variations in contact size
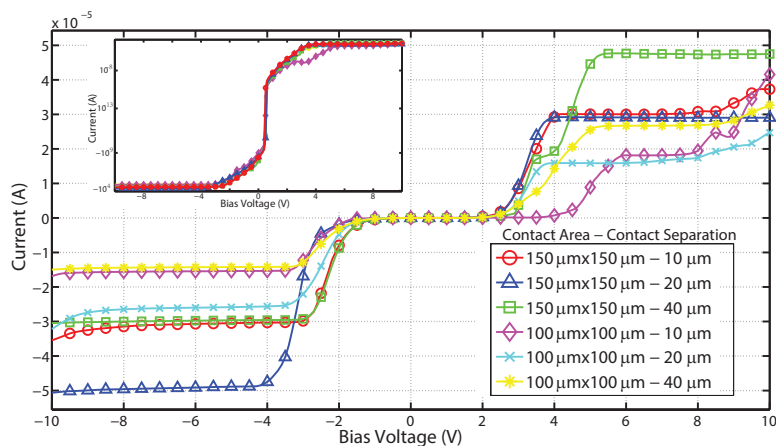


Figure A.2: Current-Voltage characteristics comparing different contact pad areas on MSM-2DES device.

## A.3 Effect of variations in contact shape
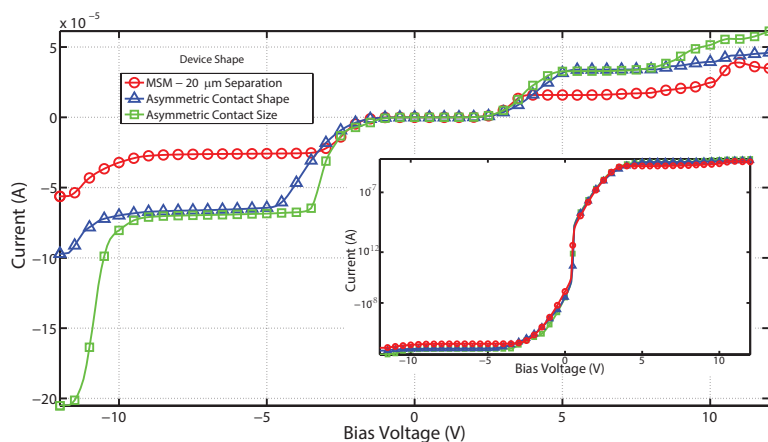


Figure A.3: Current-Voltage characteristics comparing influence of different geometries of contact pads on MSM-2DES device.

## Appendix B. Effect of contact pad geometrical properties on C-V characteristics

Here the results of C-V measurements for the MSM-2DES device with various contact pad geometries are presented. The device layer structure is as indicated in Fig. 2.1(a) and described in Chap. 2.

### B.1 Effect of asymmetry in contact pads on the C-V of MSM-2DES capacitor

Fig. B.1 indicates the C-V characteristics for MSM-2DES capacitors with asymmetric contact geometries, (shape 1 and 2 in Fig. 2.1(c)). The C-V of the TLM (symmetric) MSM-2DES capacitors are also included for comparison.
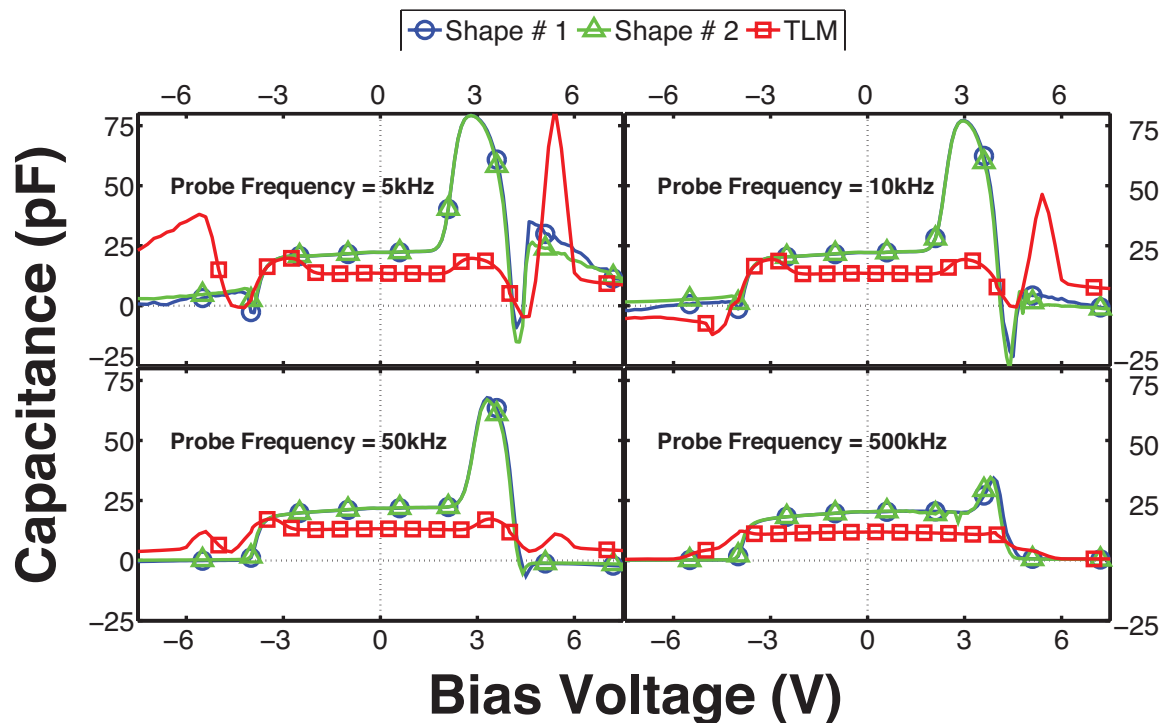


Figure B.1: C-V characteristics for asymmetric area (Shape 1) and asymmetric shape (shape 2) in comparison with TLM (symmetric) MSMs, measured at various probe frequencies.

## B.2 An MSM-2DES capacitor with interdigitated geometry for contact pads

Fig. B.2 indicates the layout for various interdigitated structures that were fabricated on top of the layer structure for the MSM-2DES capacitor.
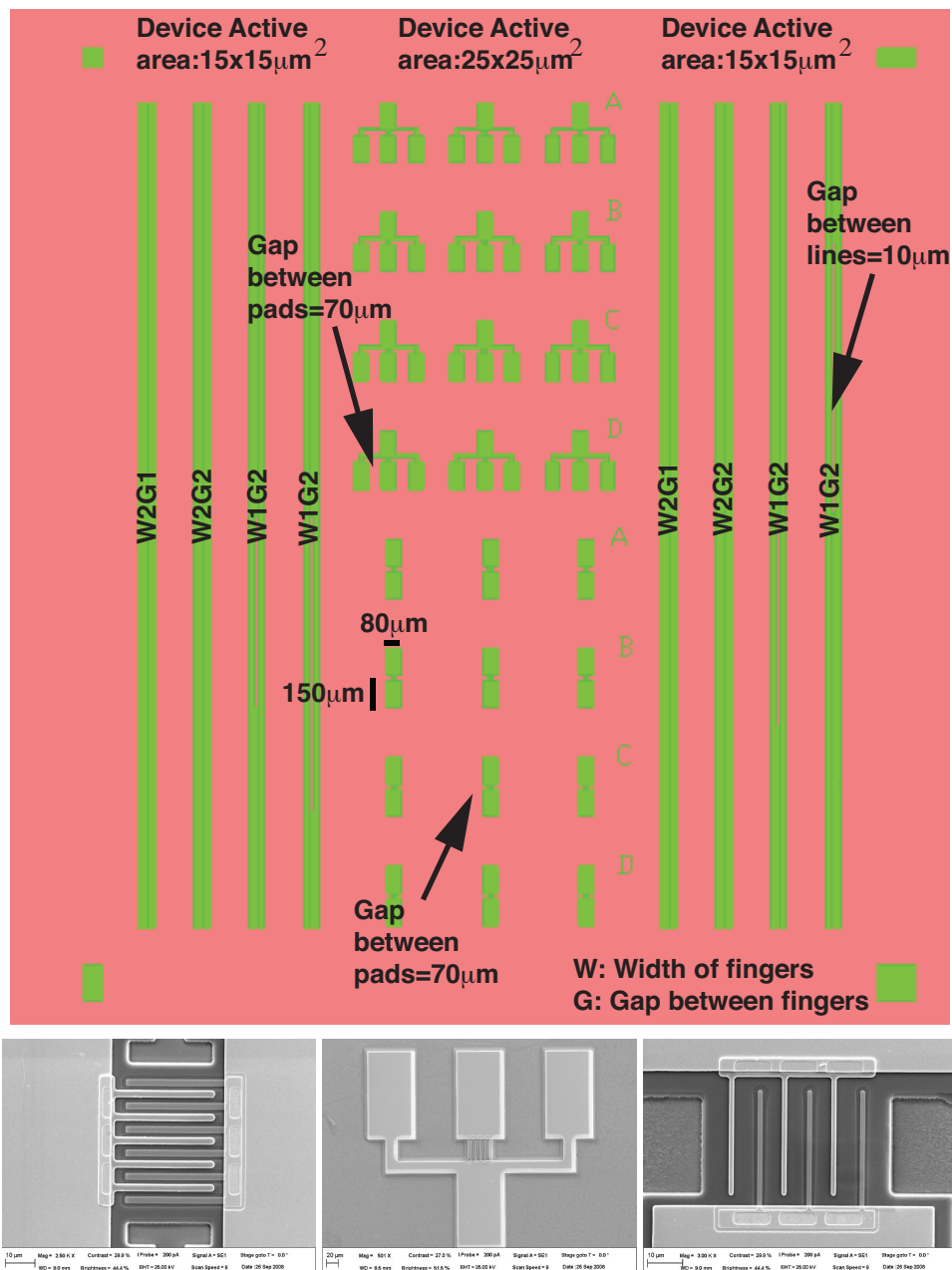


Figure B.2: Interdigitated layout for the fabricated devices.

Figs. B.3 and B.4 show the C-V and Q-V characteristics for the MSM-2DES capacitors with interdigitated structures as described in the layout of Fig. B.2
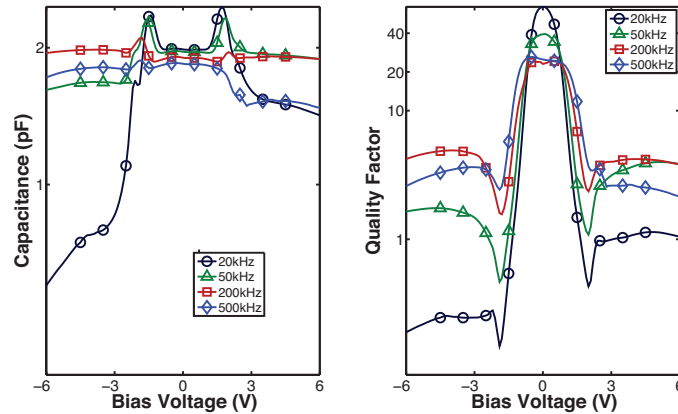


Figure B.3: Capacitance (left) and quality factor (right) characteristics for interdigitated structure at various probe frequencies.
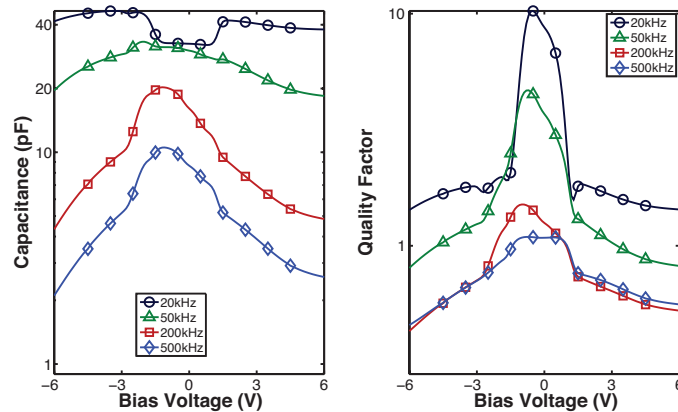


Figure B.4: Capacitance (left) and quality factor (right) characteristics for interdigitated structures attached to transmission lines in Fig. B.2, measured at various probe frequencies.

**Appendix C. "Unconventional" MSMs under extreme conditions**

Here the C-V and I-V characteristics of unconventional MSM devices are presented for measurements at $T = 4.27K$ and/or with magnetic field $B = 1T$.

## C.1    Cryogenic temperatures

### C.1.1    I-V characteristics

Fig. C.1 shows the current-voltage characteristics for MSM-2DES capacitors at various temperatures and magnetic field conditions.
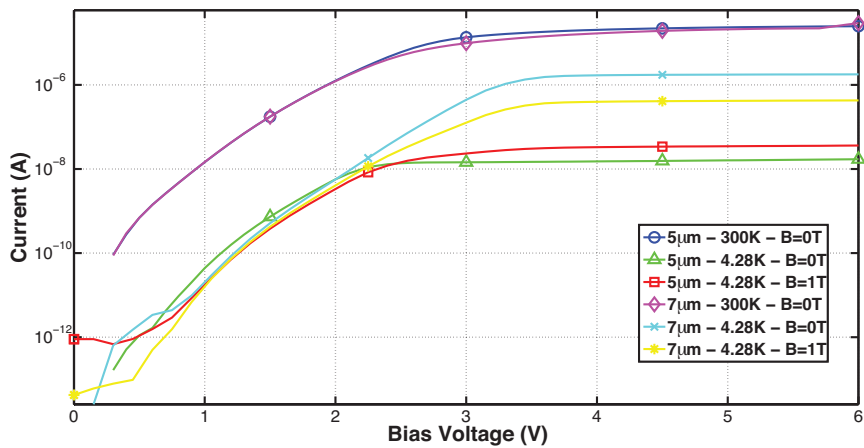


Figure C.1: I-V characteristics for MSM-2DES capacitor under various measurement conditions in temperature and magnetic field.

## C.1.2    C-V characteristics

Figs. C.2, C.3, and C.4 show the capacitance-voltage characteristics for MSM-2DES, symmetric, and asymmetric MSM-2DEHS capacitors, respectively, that are measured at $T = 4.27K$.
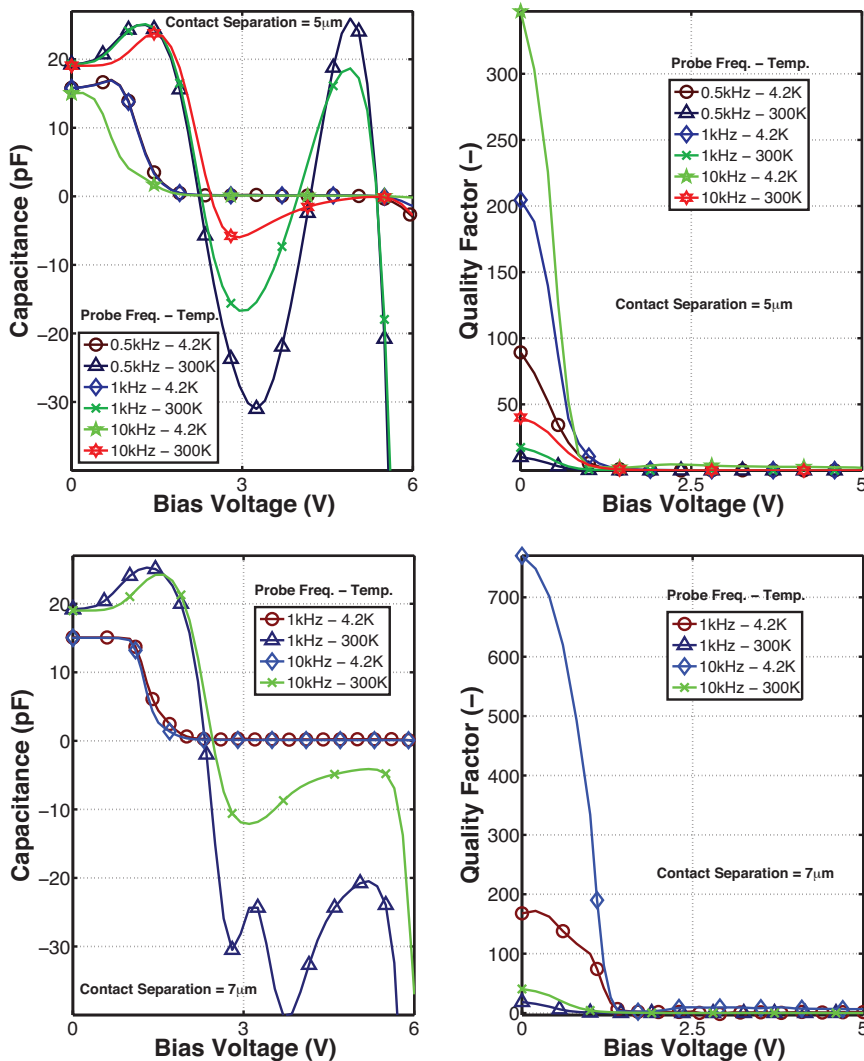


Figure C.2: MSM-2DES capacitor performance characteristics at T=4.27K. a) C-V for $5\mu m$ contact separation, b) Q-V for $5\mu m$ contact separation, c) C-V for $7\mu m$ contact separation, d) Q-V for $7\mu m$ contact separation.
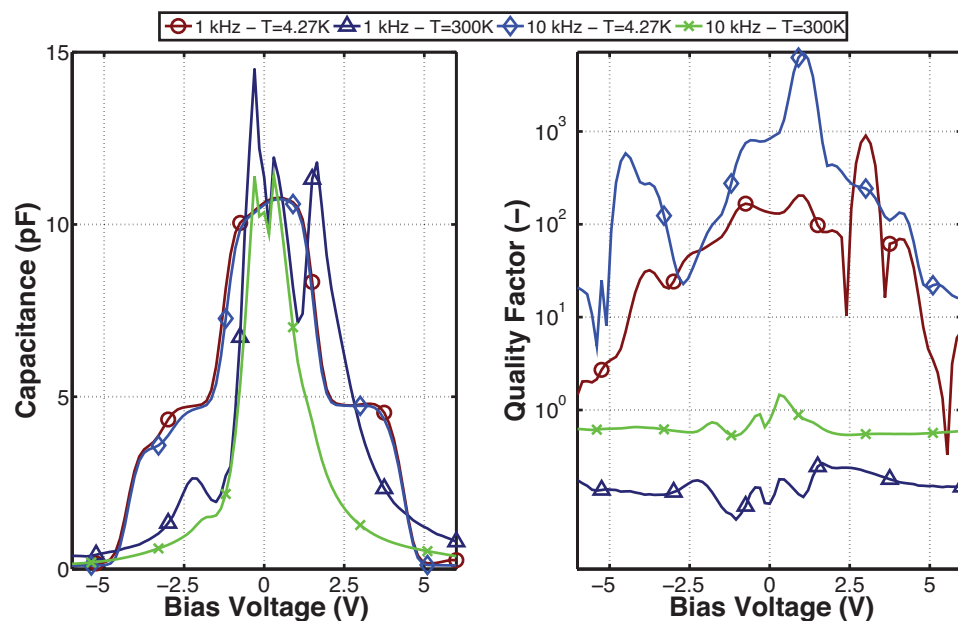
Figure C.3: a) Capacitance, and b) Quality factor vs. voltage characteristics for the symmetric Bragged MSM-2DEHS capacitor with $7\mu m$ contact separation at T=4.2K
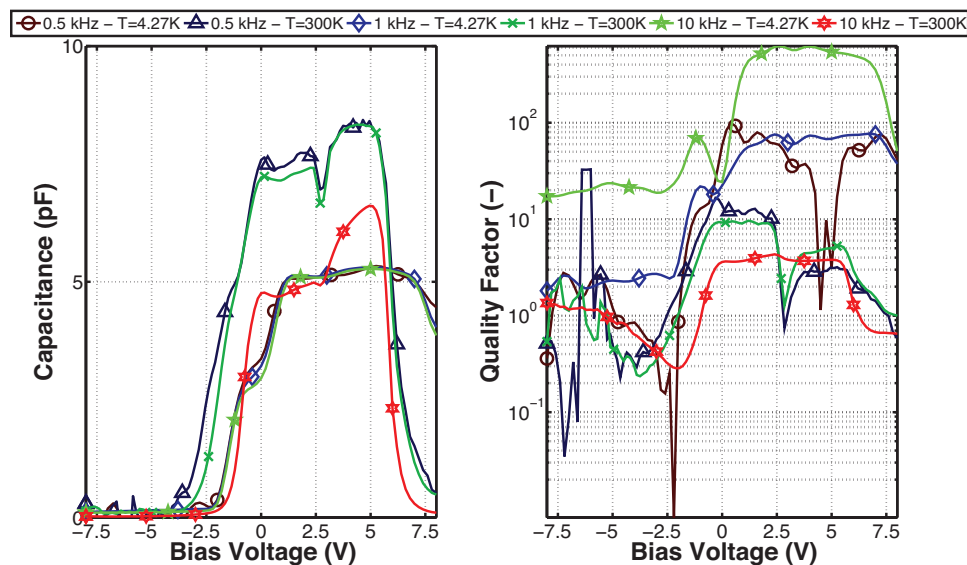


Figure C.4: a) Capacitance, and b) Quality factor for asymmetric MSM-2DEHS photodetector.

## C.2 Magnetic field

### C.2.1 C-V characteristics

Fig. C.5 shows the C-V characteristics for MSM-2DES capacitors in the presence of a magnetic field.
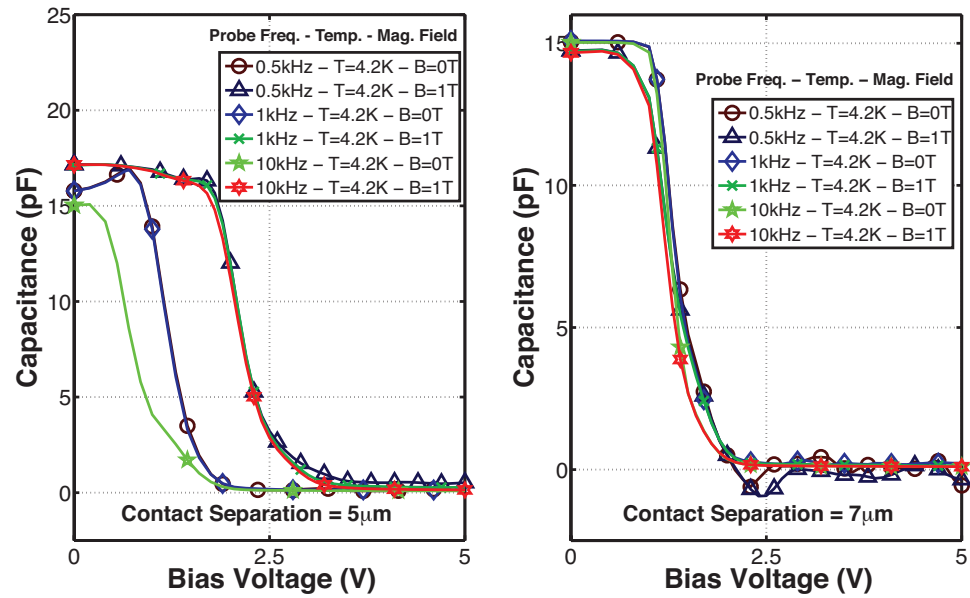


Figure C.5: C-V characteristics under magnetic field of B=1T for MSM-2DES capacitor with a) $5\mu m$, and b) $7\mu m$ contact separations.

<div align="center">

**Vita**

</div>

## Pouya Dianat

## Education

*PhD* in Electrical & Computer Engineering, Drexel University, Philadelphia PA          Feb 2015

*M.Sc* in Electrical & Computer Engineering, Drexel University, Philadelphia PA          Jun 2010

*B.Sc* in Electrical Engineering, Sharif University of Technology, Tehran, Iran          Jun 2007

## Awards and Honors

*Best Poster Award,* IEEE Research Symposium, Drexel University          Apr 2015

*Outstanding Teaching Award,* Office of Graduate Studies, Drexel University          2013 - 2014

*American Physical Society Travel Award,* American Physical Society          Mar 2014

*Allen Rothwarf Award,* for outstanding performance of a graduate student
Electrical & Computer Engineering Department, Drexel University          Jun 2013

*Joseph & Shirley Carleone Fellowship,* College of Engineering, Drexel University          Apr 2013

*Dissertation Fellowship,* Office of Graduate Studies, Drexel University          Jan 2013

## Select Patents & Publications

P. Dianat, book chapter in Photodetectors: materials, devices, applications (2015) Cambridge, UK: Woodhead Publishing

B. Nabet, P. Dianat, X. Zhao, A. A. Seddik, F. Castro, and M. Currie, book chapter in Photodetectors: materials, devices, applications (2015) Cambridge, UK: Woodhead Publishing

P. Dianat, A. Persano, F. Quaranta, A. Cola and B. Nabet, IEEE J Sel. Topics Quantum Electronics, Vol. 21, Issue 4, (2015)

B. Nabet, M. Currie, P. Dianat, F. Quaranta and A. Cola, ACS Photonics, 1 (7), 560-569, 2014

P. Dianat, R.W. Prusak, A. Persano, F. Quaranta, A. Cola and B. Nabet, IEEE Trans. on Electron Device, Vol. 61, Issue 2, (2014)

M. Currie, P. Dianat, A. Persano, M.C. Martucci, F. Quaranta, A. Cola and B. Nabet, Sensors, 13, (2013)

P. Dianat, R.W. Prusak, E. Gallo, F. Quaranta, A. Cola and B. Nabet, Appl. Phys. Lett. 100, 153505 (2012)

P. Dianat, A. Pesano, F. Quaranta, A. Cola and B. Nabet, Frontiers in Optics Conference, Orlando FL Oct. 2013, pp. FTh4C.5

P. Dianat, R.W. Prusak, A. Persano, F. Quaranta, A. Cola, B. Nabet, IEEE Photonics Conference, San Francisco CA, 2012, pp 792-793

P. Dianat, R.W. Prusak, F. Quaranta, A. Cola, B. Nabet, IEEE Compound Semiconductor IC Symposium, San Diego CA, Oct. 2012, pp 1-4

B. Nabet, P. Dianat, R.W. Prusak and E. Gallo, *"Switchable Capacitors with Embedded Charge Reservoirs."* US Patent Pending 12576262, April 18, 2012.